

Exploratory Experiments on Oil Vortices Produced Inside a Cylindrical Container

Pooya Soltanian Sedeh

A Thesis

In the Department

of

Mechanical, Industrial and Aerospace Engineering

Presented in Partial Fulfillment of the Requirements

For the Degree of Master of Applied Science (Mechanical Engineering)

At Concordia University

Montreal, Quebec, Canada

December 2017

© Pooya Soltanian sedeh, 2017

Concordia University
School of graduate studies

This is to certify that the thesis prepared

By: POOYA SOLTANIAN SEDEH

Entitled: Exploratory Experiments on Oil Vortices Produced Inside a Cylindrical Container

And submitted in partial fulfillment of the requirements for the degree of

Master of Applied Science in Mechanical Engineering

Complied with regulation of the University and meets the accepted standards with respect to originality and quality.

Signed by the final examining committee:

Dr. Charles Basenga Kiyanda Chair

Dr. Ashutosh Bagchi External Examiner

Dr. Brian Vermeire Examiner

Dr. Georgios H. Vatistas Supervisor

Dr. Hamid Ait-Abderrahmane Co-Supervisor

Approved by: Department of Mechanical, Industrial and Aerospace Engineering

Dean of Faculty

December 14th, 2017

Abstract

Exploratory Experiments on Oil Vortices Produced inside a Cylindrical Container

Pooya Soltanian Sedeh

This thesis reports the findings of exploratory tests performed with oil vortices produced inside a partially filled cylindrical tank with a rotating base. Three different liquids i.e. Spindle (22.69 cSt), H-22 (46.8 cSt) and H-32 (64.75 cSt) oils are used as the working fluid. The tests are conducted under relatively shallow liquid conditions with heights of 8, 10, and 12mm. The present observations show that the topology of the emerging equilibrium states in oils exhibits a considerably richer morphology than that of water. During a quasi-static spin-up and spin-down of the flow, states ranging from $N = 2$ to 19 are discovered. Also pulsating ($N = 0$) and wobbling ($N = 1$) modes are also detected. In the case of H-22 a retrograde pentagonal ($N = 5$) equilibrium state is found to materialize. Both the spin-up and spin-down tests are marked with strong hysteresis where in some sectors of the state manifold flow bifurcations exist. These are more prominent in the Spindle Oil than in both H-22 and H-32. In addition, for this oil, the equilibria first appear at lower disk speeds than in H-22 and H-32.

A procession of one or a group with more than one (up to 6) solitary waves arranged symmetrically in a circle around the vortex pattern, moving at higher speeds than the fluid, are identified.

Finally, pattern lock-in is found to occur at a frequency of about one-tenth the frequency of the rotating disk. Having a coefficient of variation less than one, the one-tenth value is deemed to be acceptable.

ACKNOWLEDGEMENTS

A long journey always looks short for people from outside of it however every single up and down moments touched me all the way to my bones. Shocking moments of my illness when I never expect such a problem which followed by a period of heavy rain fall of issues in my life never stopped me thinking of what I want from this lifespan.

This thesis and research work accomplishment was not possible without the continuous supports, discussions, encouragement and ideas I received from Professor Georgios H. Vatisstas, who was my M.A.Sc supervisor during my studies. He treated me like his own son and I would like to thank him for all the cooperation and helps he did for my favor. Also, I especially would like to thank Dr. Hamid Ait Abderrahmane, for his co-supervision and confidence in my expertise and helping me through the experimental and analytical parts of my thesis. I would like to thank Dr. Hoi Dick Ng for his collaborations regarding the high-speed camera and for his guidance through the experimental part of this thesis.

I would also like to thank the members of my examination committee, Professor Georgios H. Vatsitas, Dr. Brian Vermeire and Dr. Ashutosh Bagchi for taking their precious time to read and examine my thesis. Administrative and technical staffs at the department of Mechanical Industrial and Aerospace Engineering of Concordia University were always kind and supportive and I would like to thank them all.

There are many friends with whom I shared lots of moments and discussions at Concordia University, ENCS faculty and my personal life, that without their help I could not

pave this way. Thank you, Ehsan, Hamid, Nirmal, Vinay, Philip, Antoune, Garo and Margesh for the joyful memories that I will remember throughout my life.

My sincerest and heartiest gratitude goes to my brother Al, my mother Giti, my sister Laleh, my brother in law Shabir, my uncle David, my aunt Jane and my niece Nafas who have been always supporting me with their invaluable love. My sister Laleh as well as my brother in law Shabir, did a great devotion by supporting me and covering my responsibilities during my absence at home. And last but not the least, Ehsan and Hamid who showed me support in friendship is borderless. I have never imagined myself overcoming such a goal without boundless dedication of all of you.

Finally, I would like to thank Concordia University and faculty of engineering and computer science for the funds they provided to me through my supervisors' grants.

Contents

| | |
|--|------|
| Figures | x |
| Tables | xv |
| Nomenclature | xvii |
| 1 Introduction | 1 |
| 1.1 Problem Statement | 1 |
| 1.2 Previous Work with a Low Viscosity Liquid (Water) | 3 |
| 1.3 Previous Work with Intermediate Viscosity Liquid (Oil) | 8 |
| 1.4 Contribution of the Thesis | 10 |
| 2 Dimensional Analysis | 11 |
| 3 Experimental Apparatus Instrumentation and Procedure | 17 |
| 3.1 The Experimental Apparatus | 17 |
| 3.2 The High-Speed Camera | 18 |
| 3.3 The Lighting System | 19 |
| 3.4 Description of the Oils | 20 |
| 3.5 Procedure | 20 |
| 3.5.1 General Description | 20 |
| 3.5.2 Estimation of Experimental Uncertainties Associated with the | |

| | |
|---|----|
| Measurements | 21 |
| 4 Results and Discussion..... | 24 |
| 4.1 Evolution of Equilibrium States | 24 |
| 4.1.1 Spindle Oil | 24 |
| 4.1.2 Clusters of Synchronized Rotating Single Depression Solitons in Polygonal Formations | 46 |
| 4.1.3 H-22 Hydraulic Oil | 51 |
| 4.1.4 H-32 Hydraulic Oil | 55 |
| 4.2 Image Processing Through MATLAB | 59 |
| 4.3 Analysis | 61 |
| 4.4 Results..... | 66 |
| 5 Conclusions | 69 |
| 6 Future Work | 70 |
| 7 References | 71 |
| Appendix A | 77 |
| Appendix B..... | 83 |
| Appendix C..... | 89 |
| Appendix D | 92 |

| | |
|------------------|----|
| Appendix E | 97 |
| Appendix F | 99 |

Figures

| | |
|--|----|
| Figure 1. A schematic of Kelvin's Vortex Atoms. | 1 |
| Figure 2. A schematic of the apparatus utilized by Vatistas (1990) | 4 |
| Figure 3. Actual equilibria (Courtesy of Professors Vatistas and Ait-Abderrahmane).6 | |
| Figure 4. Schematic of typical equilibrium and transitional (mixed states) gaps spectrum. The $N = 7$ is in real settings unstable (Courtesy of Professor Vatistas). | 7 |
| Figure 5. The heptagon must live theoretically in an exceedingly very thin range of disk speeds or in real settings unstable (Courtesy Prof. Vatistas). | 8 |
| Figure 6. Oil Kelvin's equilibria with $N = 8, 10$, and 16 ($N = 8$ and 10 from Vatistas et al. (1992)), $N = 16$ recent observation. | 9 |
| Figure 7. Diagram of the experimental apparatus, $Rt = 143$ mm and $Rd = 142$ mm. The clearance between the disk and the bottom plate (ε) was 28 mm while the disk's thickness was 9.525 mm. | 18 |
| Figure 8. One Complete Revolution of the Pattern..... | 22 |
| Figure 9. One image of a set of three rotating solitary waves | 26 |
| Figure 10. Spindle Oil (8mm) Ascending Sequence Actual Equilibria..... | 28 |
| Figure 11. Spindle Oil (8mm) Descending Sequence Actual Equilibria..... | 31 |
| Figure 12. Spindle Oil (8mm) Schematic of Typical Equilibrium Spectrum | 32 |
| Figure 13. Typical shapes of the pattern shapes (a) of the pulsating mode ($A = 0.2$, $k = 0$, $n = 2$ and $\omega = 2$, for $z = 0$) and (b) wobbling (all are the same as previous but in | |

| | |
|--|----|
| this case $k = 1$). | 34 |
| Figure 14. Spindle Oil (10mm) Ascending Sequence Actual Equilibria..... | 36 |
| Figure 15. Spindle Oil (10mm) Descending Sequence Actual Equilibria | 39 |
| Figure 16. Spindle Oil (10mm) Schematic of Typical Equilibrium Spectrum | 40 |
| Figure 17. Spindle Oil (12mm) Ascending Sequence Actual Equilibria..... | 42 |
| Figure 18. Spindle Oil (12mm) Descending Sequence Actual Equilibria | 45 |
| Figure 19. Spindle Oil (12mm) Schematic of Typical Equilibrium Spectrum | 45 |
| Figure 20. Spindle Oil 3D Graph Representing <i>Taylor's No.</i> versus N and $hORd$ ratio | 46 |
| Figure 21. Clusters of $m = 2$, and 3 solitons frozen in time. | 47 |
| Figure 22. Solitary Waves with $m = 2, 3$ and 6 ($hO = 10\text{ mm}$) | 48 |
| Figure 23. Gaussian free surface profile of the soliton..... | 49 |
| Figure 24. Signals of the Solitary waves ($hO = 10\text{ mm}$)..... | 50 |
| Figure 25. H-22 Oil (8mm) Schematic of Typical Equilibrium Spectrum | 53 |
| Figure 26. H-22 Oil (10mm) Schematic of Typical Equilibrium Spectrum | 53 |
| Figure 27. H-22 Oil (12mm) Schematic of Typical Equilibrium Spectrum | 54 |
| Figure 28. H-22 Oil 3D Graph Representing <i>Taylor's No.</i> versus N and $hORd$ ratio | 54 |
| Figure 29. Harmonic Modulation of the $N = 3$ state by an $N = 9$ wave in oil having a | |

| | |
|---|----|
| viscosity of 5.7 cSt (courtesy of G. H. Vatistas and J. Wang 1992)..... | 56 |
| Figure 30. H-32 Oil (8mm) Schematic of Typical Equilibrium Spectrum | 57 |
| Figure 31. H-32 Oil (10mm) Schematic of Typical Equilibrium Spectrum | 57 |
| Figure 32. H-32 Oil (12mm) Schematic of Typical Equilibrium Spectrum | 58 |
| Figure 33. H-32 Oil 3D Graph Representing <i>Taylor's No.</i> versus <i>N</i> and <i>hORd ratio</i> | 58 |
| Figure 34. Typical Image of Experiments | 59 |
| Figure 35. Image Processing Procedure..... | 61 |
| Figure 36. Signal Analysis | 62 |
| Figure 37. (a) Fast Fourier Transform. (b) State Number..... | 62 |
| Figure 38. Mixed States Representation | 64 |
| Figure 39. Pattern interrupted with solitary waves | 65 |
| Figure 40. Superimposed Figure Representing <i>C</i> ratio versus <i>Taylor's Number</i> | 67 |
| Figure 41. (a) Power Spectrum Density (PSD) of patterns from 3 to 6 modes, showing a pattern frequency lock-in at about 1/3 of the disk. (b) Frequency ratio vs. the Froude number. The average value of the set is 0.33 having a standard deviation of 0.01 | 68 |
| Figure 42. H-22 Oil (8mm) Ascending Sequence Actual Equilibria..... | 77 |
| Figure 43. H-22 Oil (8mm) Descending Sequence Actual Equilibria | 78 |
| Figure 44. H-22 Oil (10mm) Ascending Sequence Actual Equilibria..... | 79 |

| | |
|--|----|
| Figure 45. H-22 Oil (10mm) Descending Sequence Actual Equilibria | 80 |
| Figure 46. H-22 Oil (12mm) Ascending Sequence Actual Equilibria..... | 81 |
| Figure 47. H-22 Oil (12mm) Descending Sequence Actual Equilibria | 82 |
| Figure 48. H-32 Oil (8mm) Ascending Sequence Actual Equilibria..... | 83 |
| Figure 49. H-32 Oil (8mm) Descending Sequence Actual Equilibria | 84 |
| Figure 50. H-32 Oil (10mm) Ascending Sequence Actual Equilibria..... | 85 |
| Figure 51. H-32 Oil (10mm) Descending Sequence Actual Equilibria | 86 |
| Figure 52. H-32 Oil (12mm) Ascending Sequence Actual Equilibria..... | 87 |
| Figure 53. H-32 Oil (12mm) Descending Sequence Actual Equilibria | 88 |
| Figure 54. $N=3$ Analysis – Spindle Oil..... | 89 |
| Figure 55. $N=19$ Analysis – Spindle Oil | 89 |
| Figure 56. $N=5$ Analysis – Spindle Oil..... | 89 |
| Figure 57. $N=15$ Analysis – H-22 Oil..... | 90 |
| Figure 58. $N=7$ Analysis – H-22 Oil..... | 90 |
| Figure 59. $N=9$ Analysis – H-32 Oil..... | 90 |
| Figure 60. $N=12$ Analysis – H-32 Oil..... | 91 |
| Figure 61. C Ratio versus <i>Taylor Number</i> - Spindle Oil (8mm) | 92 |
| Figure 62. C Ratio versus <i>Taylor Number</i> - Spindle Oil (10mm) | 92 |

| | |
|---|----|
| Figure 63. <i>C</i> Ratio versus <i>Taylor Number</i> - Spindle Oil (12mm) | 93 |
| Figure 64. <i>C</i> Ratio versus <i>Taylor Number</i> – H-22 Oil (8mm)..... | 93 |
| Figure 65. <i>C</i> Ratio versus <i>Taylor Number</i> – H-22 Oil (10mm)..... | 94 |
| Figure 66. <i>C</i> Ratio versus <i>Taylor Number</i> – H-22 Oil (12mm)..... | 94 |
| Figure 67. <i>C</i> Ratio versus <i>Taylor Number</i> – H-32 Oil (8mm)..... | 95 |
| Figure 68. <i>C</i> Ratio versus <i>Taylor Number</i> – H-32 Oil (10mm)..... | 95 |
| Figure 69. <i>C</i> Ratio versus <i>Taylor Number</i> – H-32 Oil (12mm)..... | 96 |
| Figure 70. Superposition of Reynolds Number vs Froude Number | 97 |
| Figure 71. Superposition of Taylor Number vs Froude Number | 97 |
| Figure 72. Superposition of Taylor Number vs Reynolds Number | 98 |

Tables

| | |
|---|----|
| Table 1. Spindle Oil – 8mm Ascending Sequence Equilibria | 27 |
| Table 2. Spindle Oil – 8mm Descending Sequence Equilibria..... | 30 |
| Table 3. Spindle Oil – 10mm Ascending Sequence Equilibria | 35 |
| Table 4. Spindle Oil – 10mm Descending Sequence Equilibria..... | 38 |
| Table 5. Spindle Oil – 12mm Ascending Sequence Equilibria | 42 |
| Table 6. Spindle Oil – 12mm Descending Sequence Equilibria..... | 44 |
| Table 7. H-22 Oil – 8mm Ascending Sequence Equilibria | 77 |
| Table 8. H-22 Oil – 8mm Descending Sequence Equilibria..... | 78 |
| Table 9. H-22 Oil – 10mm Ascending Sequence Equilibria | 79 |
| Table 10. H-22 Oil – 10mm Descending Sequence Equilibria..... | 80 |
| Table 11. H-22 Oil – 12mm Ascending Sequence Equilibria | 81 |
| Table 12. H-22 Oil – 12mm Descending Sequence Equilibria..... | 82 |
| Table 13. H-32 Oil – 8mm Ascending Sequence Equilibria | 83 |
| Table 14. H-32 Oil – 8mm Descending Sequence Equilibria..... | 84 |
| Table 15. H-32 Oil – 10mm Ascending Sequence Equilibria | 85 |
| Table 16. H-32 Oil – 10mm Descending Sequence Equilibria..... | 86 |

| | |
|---|----|
| Table 17. H-32 Oil – 12mm Ascending Sequence Equilibria | 87 |
|---|----|

| | |
|---|----|
| Table 18. H-32 Oil – 12mm Descending Sequence Equilibria..... | 88 |
|---|----|

Nomenclature

| | | |
|-------|---|-----------------|
| He | Helium | |
| h_0 | Initial height of the fluid | mm |
| g | Gravitational acceleration | $\frac{m}{s^2}$ |
| R_d | Radius of disk | mm |
| R_t | Radius of tank | mm |
| f | Function | |
| fr | Camera's frequency | Hz |
| PIV | Particle Image Velocimetry | |
| T | Camera's period | s |
| R | The radius of the undisturbed pattern on the disk's surface | |
| A | The amplitude of the harmonic perturbation | |
| r_s | The radial position of the interface | |
| v | Disk velocity | $\frac{m}{s}$ |
| R | Radius of disk | m |

Greek Letters

| | | |
|---------------|---|-----------------|
| ω_d | Disk speed | rpm |
| ω_p | Pattern speed | rpm |
| ν | Kinematic viscosity | $\frac{m^2}{s}$ |
| ε | The clearance between the disk and the bottom plate | mm |

Dimensionless numbers and variables

| | | |
|--------|---|---------------------------------|
| η | Amplitude of the soliton | |
| Fr | Froude number | $\frac{v}{\sqrt{gh}}$ |
| Re | Reynolds number | $\frac{vl}{\nu}$ |
| Ta | Taylor number | $\frac{4\omega_d^2.R^4}{\nu^2}$ |
| C | Ratio of pattern's velocity to disk's velocity | $\frac{\omega_p}{\omega_d}$ |
| k | Wave number in the radial direction | |
| N | State number | |
| m | Number of solitons | |
| n | Wave number in the axial direction | |
| x | Dimensionless distance from the center of the soliton | |

1 Introduction

1.1 Problem Statement

The subject matter of this thesis is based on a classical topic, which was first studied theoretically in 1880 by William Thomson (Lord Kelvin). Kelvin in search of an *ethereal* atomic theory of matter investigated the vibration of columnar vortices postulating that the core is able to harbor three-dimensional perturbations with various wave numbers [Thomson (1869)]. Their motion, being frictionless and stable, once produced by a “creative power”, will last forever, see Fig. 1.

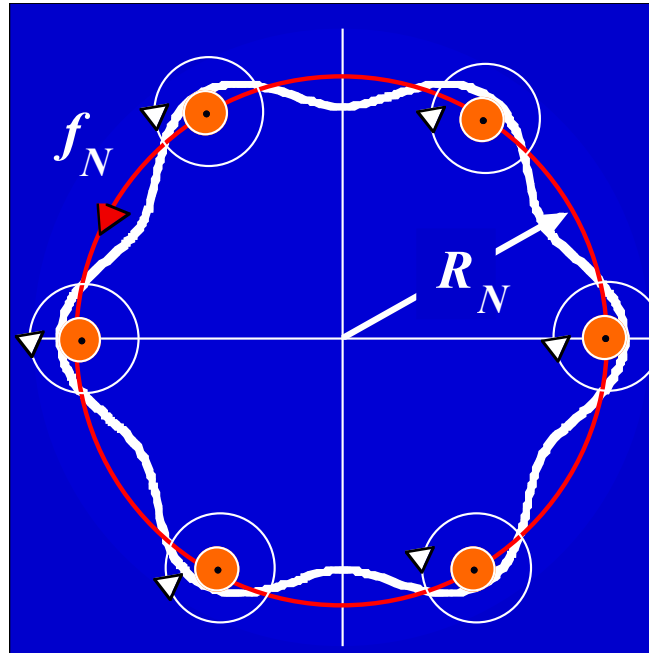


Figure 1. A schematic of Kelvin's Vortex Atoms.

As a result of the Michelson-Morley (1887) experiment and Einstein's special relativity (1905) against the existence of *ether* (a hypothetical ideal fluid) the initial notion was abandoned for a prolonged period time. However, a rekindled interest in the subject was prompted by its significance in many scientific areas such as super-fluidity [Williams (1974)], plasma physics [Durkin and Fajans (2000)] atmospheric and oceanographic sciences [Stewart (1943), Carnevale and Kloosterziel (1995)]. The possibility that unusual phenomena such as Saturn's hexagonal North pole vortex structure [Godfrey (1988), Polvani (1993), Barbosa-Aguiar (2010), Morales-Juberías et al. (2011)], the double vortex in Venus' South pole [Taylor (2006)], suction vortices in tornados [Fujita (1972), Bedard (2005)], meso-vortices in hurricanes and typhoons [Braun et al. (2006), Lewis (1982), Schubert, (1999)], volcanic revolving columns [Chakraborty (1999)], or in galactic hydrodynamics [Fridmann (1985)] could have a similar root made this subject more appealing.

Flow conditions can change from laminar to turbulent conditions into two manners. The first involves a precipitous switch. Classical paradigm of this sort of flow transformation is the Hagen-Poiseuille flow in a circular pipe. At low Reynolds numbers the flow field is classified as laminar having the highest degree of symmetry. Beyond a critical value of the Reynolds number (of about 2,000), the flow transfers into the turbulent state traversing first a narrow sector (Reynolds numbers between 2,000 - 3,000) where the flow is in transition.

The second route of changeover involves a slow alteration whereby as the Reynolds number increases the system is passing through different laminar flow states. Ultimately, a further increase of the Reynolds number the dynamical noise intensifies gradually and finally overwhelms the flow destroying its symmetry, giving rise to turbulence. Two clear examples of

the slow transition are flows within two concentric cylinders (Taylor-Goertler flow) and spheres [Sawatzki (1970)]. Another example of slow transition can be observed utilizing a rotating disk submerged in water [Vatistas (1990)].

1.2 Previous Work with a Low Viscosity Liquid (Water)

The origins of the hydrodynamic theoretical side of the problem, with an inviscid fluid, could be found in Helmholtz's work on vorticity, which dealt with the stability of one and two vortices in an infinite fluid. Kelvin dealt with the stability of three vortices. J.J. Thomson (1883) examined the situations of three to seven, predicting instability to set in for any ensemble $N > 6$. Cabral and Schmidt (1999) and Kurakin and Yudovich (2008) showed that the $N = 7$ system is stable.

The first experimental tests related to the same theme were performed by Gregory et al. (1955) revealing the existence of $N = 6$ vortices. Yarmchuk et al. (1979) found similar vortex arrays in superfluid helium (He with a small amount (0.8% of ^4He)). Utilizing the Malmberg-Penning electron trap, Durkin and Fajans validated Havelock's (1931) analytical predictions. The complete sets of these polygonal structures were also observed earlier by Vatistas (1990) using the experimental apparatus shown in Fig. 3.

Subsequent to the original discovery by Vatistas (1990), the studies of Vatistas *et al.* (2008) disclosed that waves developed on the free liquid surface, possessed all the basic attributes of Kelvin's equilibria (Thomson (1875-6)).

The revolving fluid motion generates a centrifugal force that pushes the liquid towards wall

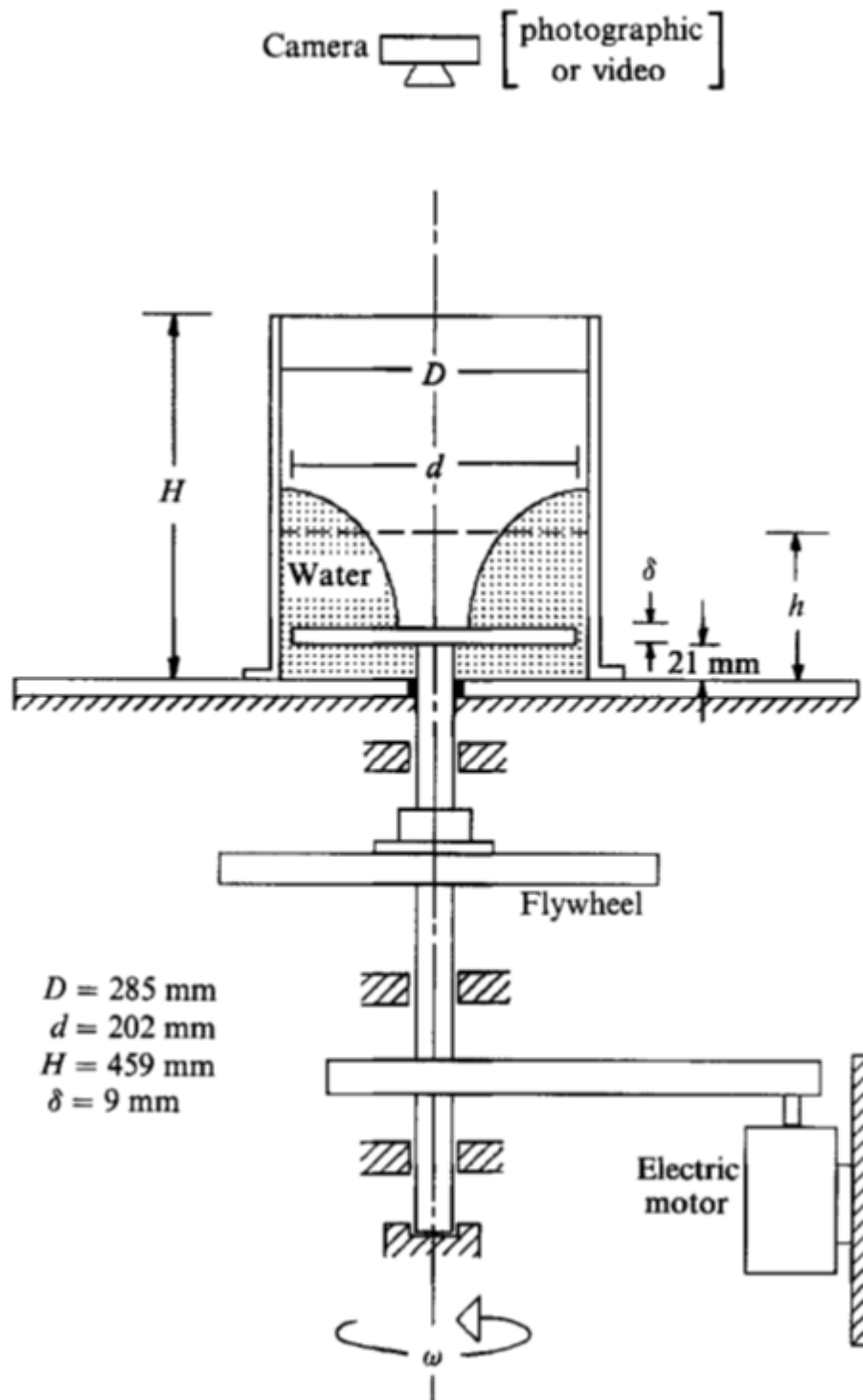
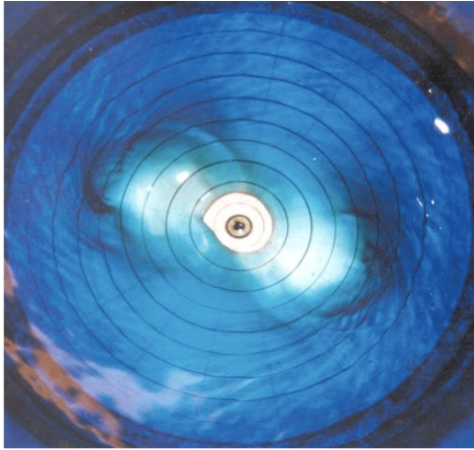


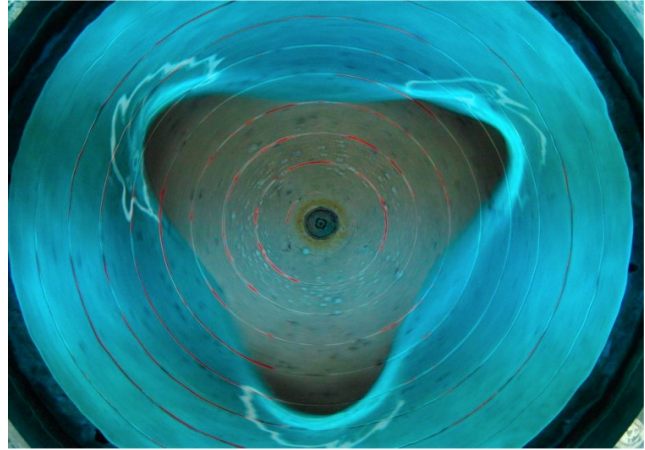
Figure 2. A schematic of the apparatus utilized by Vatistas (1990)

of the cylindrical reservoir. The retreating liquid makes the vortices to touch the disk thus

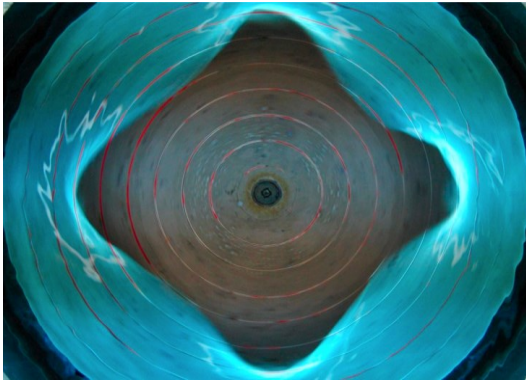
revealing part of its surface to atmospheric air. The common line of the solid, liquid, and air designates the form of the core. For contrast, the fluid was colored with a blue dye. Under shallow water conditions and low disk speeds the vortex core is circular ($N = 0$). Increasing the disk rotation, the vortex flow moves into another state characterized by a precessing core. A gradual augmentation of the disk speed, yields incrementally vortex cores with $N = 2$, $N = 3$, $N = 4$, $N = 5$, and $N = 6$, see Fig. 2.



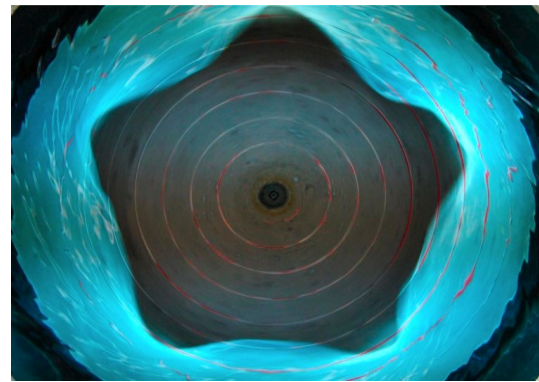
$N = 2$



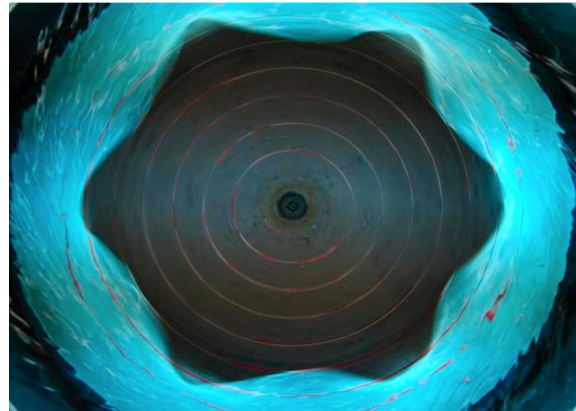
$N = 3$



$N = 4$



$N = 5$



$N = 6$

Figure 3. Actual equilibria (Courtesy of Professors Vatistas and Ait-Abderrahmane).

The power spectrum shown in Fig. 3, shows that between equilibrium shapes, patterns of mixed states exist. The interval of resilience of the different equilibrium patterns and mixed states reduce with increasing N . It is important to note incidentally that Kelvin (Thomson 1875-6) had accurately predicted the expected cores of $N = 2$ to 5. No lasting $N = 7$ was able to appear. The missing $N = 7$ in the tests was attributed to the narrowness of the range of speeds where the $N = 7$ could survive [Vatistas et al. (2008)], see Fig. 3. Using a high-speed camera Vatistas and Ait-Abderrahmane (2012) were ultimately able to obtain several consecutive images of the heptagon see Fig. 4; but it was short lived ($\sim 1/10$ sec). The pattern appeared to temporally vary from $N = 7$ to 8 and vice versa, forming in between patterns of unidentifiable shape.

Spectra-water

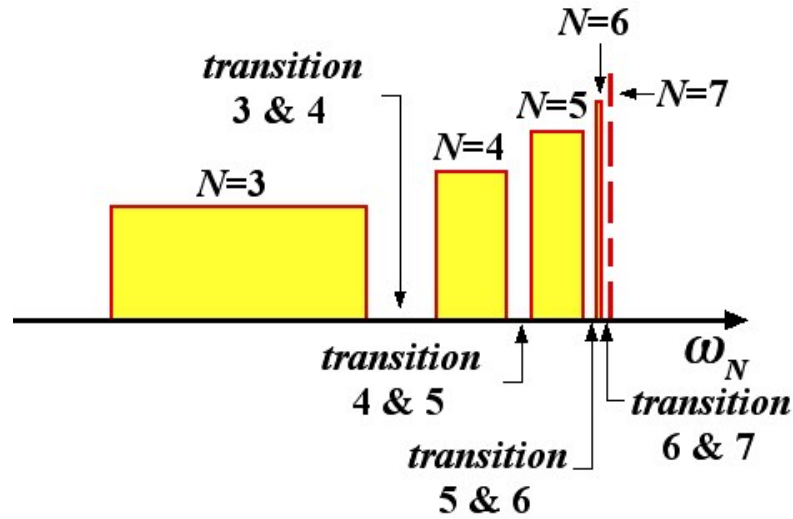


Figure 4. Schematic of typical equilibrium and transitional (mixed states) gaps spectrum. The $N = 7$ is in real settings unstable (Courtesy of Professor Vatistas).

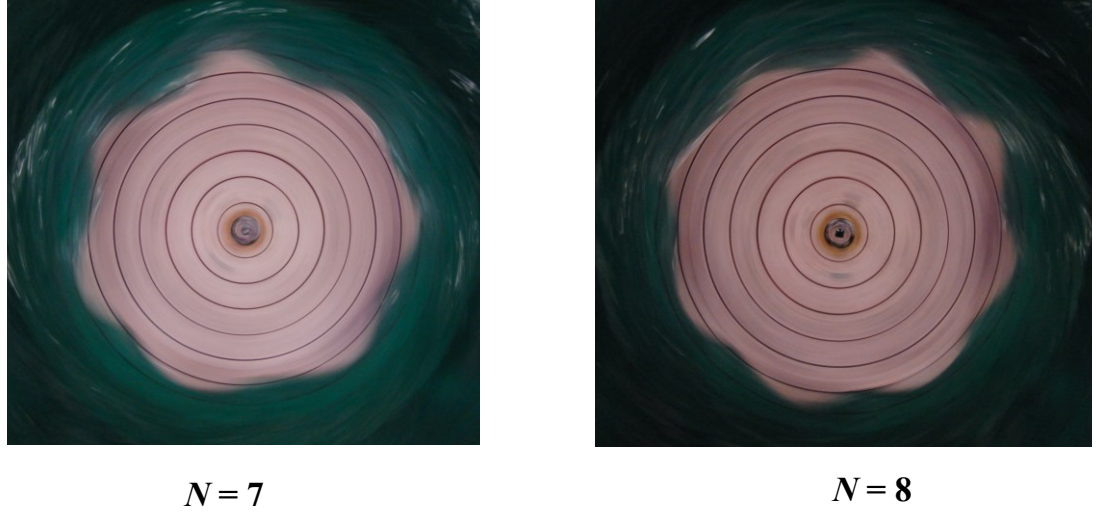


Figure 5. The heptagon must live theoretically in an exceedingly very thin range of disk speeds or in real settings unstable (Courtesy Prof. Vatistas).

In 2006 Jansson et al. (2006) confirmed Vatistas's (1990) findings using a similar experimental arrangement, but with a rotating bottom (The ratio of the disk diameter to the container was much lower than Vatistas work). Continuing their investigations, the Concordia group, confirmed using the Particle Image Velocimetry (PIV) technique that the autorotation property of three-vortex ensemble could be approximated by the old idealized point vortex theory [Ait-Abderrahmane et al. (213)].

1.3 Previous Work with Intermediate Viscosity Liquid (Oil)

Higher viscosity vortices produce considerably richer manifestations and consequently are more complex in nature than water. There is only one journal paper by Vatistas et al. (1992) and a doctoral thesis by Wang (1995) that dealt with the previous problem using oils with kinematic viscosities $\nu = 5.7 \times 10^{-5} \frac{m^2}{s}$ and $\nu = 6.4 \times 10^{-4} \frac{m^2}{s}$ as the working fluids. The

experiments however were conducted relying on primitive instruments; a low resolution, low-speed video camera, a photographic camera for still pictures, a stroboscope, as well on visual inspections. In the case of water, the order in which the equilibria evolve is sequentially, traversing almost the same route during the spin-up and spin-down schedule. In the case of oil vortices, not only the flow patterns during the ascending and descending schedules are not in sequence but also one encounters multiple states under the same boundary conditions. The transition from one stationary equilibrium state to another happens abruptly. Steady vortex patterns with polygons from one to eleven were observed, see Fig. 5 for the case of $N = 8$ and 10, while in a recent image (current work) an $N = 16$ showed up. States whereby one wave modulate harmonically another, and states where one or two wave packets (solitary waves) periodically encircled the base wave core were also visualized. Also peculiar is that there exist retrograde equilibria that were never observed in very low viscosity liquids such as water. In the case of higher viscosity oil with $\nu = 6.4 \times 10^{-4} \frac{m^2}{s}$ the vortex core was circular and stable. For very large initial oil heights ($h_0 > 100mm$) and disk speeds ($\omega_d > 800 rpm$), significantly dispersed waves emerged. All these results were obtained visually using an ordinary video camera, an optical speedometer and a stroboscope.

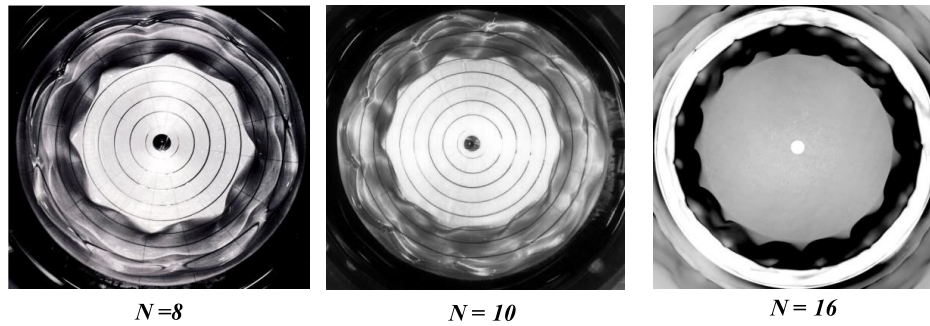


Figure 6. Oil Kelvin's equilibria with $N = 8, 10$, and 16 ($N = 8$ and 10 from Vatistas et al. (1992)), $N = 16$ recent observation.

1.4 Contribution of the Thesis

The present study is a continuation of the Vatistas et al. (1992) principal finding along with the studies reported by Wang in (1995). The current tests were conducted using three different oils with viscosities ranging from 22 to 65 centistokes. Observations illustrate the dynamics of the flow evolution during the spin-up and spin-down tests. More precisely, the goal here is to examine how the flow unfolds during a sequential quasi-static increase and decrease *vis-à-vis* the governing dimensionless groups. All experimental runs start from rest (zero disk velocity) and the ascending sequence continues up to a point where the flow is no more under laminar conditions. Then the spin-down process takes place where the disk rotation is decreased gradually to zero. The evolutionary history of the different equilibrium state spectra is presented. Applying image processing, the contour of each pattern extracted and an estimation of the patterns' speed as a function of Taylor's number is obtained. The newly discovered rotating clusters of solitary waves are also investigated.

2 Dimensional Analysis

Past observations with water and oil along with present exploratory experiments using different viscosity oils suggest that the problem depends functionally on the following parameters:

$$N = f\{\nu, \omega_d, R_d, h_o\} \quad (1)$$

There are 4 independent dimensional variables in the above functional relationship Eq. 1 (ν, ω_d, R_d and h_o , note N is dimensionless), involving 2 basic dimensions: length (L) and time (T). Therefore, according to dimensional analysis 2+1 dimensionless numbers are required to describe the problem:

$$\pi_1 = \omega_d^\varepsilon R_d^\zeta \nu = \left(\frac{\text{rads}}{T}\right)^\varepsilon L^\zeta \frac{L^2}{T} = L^0 T^0$$

$$T: -\varepsilon - 1 = 0 \rightarrow \varepsilon = -1$$

$$L: \zeta + 2 = 0 \rightarrow \zeta = -2$$

$$\pi_1 = \frac{\nu}{\omega_d R_d^2}$$

$$\pi_1' = \frac{\omega_d R_d^2}{\nu} = \text{Re}$$

$$\pi_2 = \omega_d^\theta R_d^\eta h_o = \left(\frac{rads}{T} \right)^\theta L^\eta L = L^0 T^0$$

$$T: -\theta=0 \rightarrow \theta=0$$

$$L: \eta+1=0 \rightarrow \eta=-1$$

$$\pi_2 = \frac{h_o}{R_d}$$

and

$$\pi_3 = N$$

Hence the phenomenon can be stated equivalently with the following functional relationship,

$$N = f_n \left\{ \mathbf{Re}, \frac{h_o}{R_d} \right\}$$

Since Taylor's number (Ta) denotes the ratio of centrifugal to viscous forces,

$$Ta = \frac{4 \omega_d^2 R_d^4}{\nu^2} = \frac{4 (\omega_d R_d^2)^2}{\nu^2} = 4 \left(\frac{\omega_d R_d^2}{\nu} \right)^2$$

Then

$$Ta = 4 \text{Re}^2 \rightarrow \text{Re} = 2\sqrt{Ta}$$

Therefore,

$$N = fn \left\{ Ta, \frac{h_o}{R_d} \right\}$$

If the aspect ratio is kept constant ($h_o / R_d = \text{const.}$) then,

$$N = fn \{ Ta \}$$

or

$$N = fn \{ \text{Re} \}$$

We now assume that the speed of the pattern depends on:

$\nu, g, \omega_d, R_d, h_o$, and N , or

$$\omega_p = f \{ \nu, g, \omega_d, R_d, h_o, N \} = 0 \quad (2)$$

There are 6 independent dimensional variables in the above functional relationship Eq. 2 ($\nu, g, \omega_d, \omega_p, R_d$, and h_o , note N is dimensionless), involving 2 basic dimensions: length (L) and time (T).

Therefore, according to dimensional analysis 4+1 dimensionless numbers are required to describe the problem equivalently:

$$\pi_1 = \omega_d^\alpha R_d^\beta \omega_p = \left(\frac{rads}{T} \right)^\alpha L^\beta \frac{1}{T} = L^0 T^0$$

$$T: -\alpha - 1 = 0 \rightarrow \alpha = -1$$

$$L: \beta = 0 \rightarrow \beta = 0$$

$$\pi_1 = \frac{\omega_p}{\omega_d}$$

which is the celerity ratio.

$$\pi_2 = \omega_d^\gamma R_d^\delta g = \left(\frac{rads}{T} \right)^\gamma L^\delta \frac{L}{T^2} = L^0 T^0$$

$$T: -\gamma - 2 = 0 \rightarrow \gamma = -2$$

$$L: \delta + 1 = 0 \rightarrow \delta = -1$$

$$\pi_2 = \frac{g}{\omega_d^2 R_d} = \frac{g h_o}{\omega_d^2 R_d^2 \frac{h_o}{R_d}} = \frac{1}{Fr^2 \frac{h_o}{R_d}}$$

$$\pi_2' = \frac{\omega_d^2 R_d^2 \frac{h_o}{R_d}}{g h_o} \square Fr \sqrt{\frac{h_o}{R_d}} = Fr'$$

Where, Fr' is the reduced Froude number.

$$\pi_3 = \omega_d^\varepsilon R_d^\zeta \nu = \left(\frac{rads}{T} \right)^\varepsilon L^\zeta \frac{L^2}{T} = L^0 T^0$$

$$T: -\varepsilon - 1 = 0 \rightarrow \varepsilon = -1$$

$$L: \zeta + 2 = 0 \rightarrow \zeta = -2$$

$$\pi_3 = \frac{\nu}{\omega_d R_d^2}$$

$$\pi_3' = \frac{\omega_d R_d^2}{\nu} = \text{Re}$$

The Reynolds number,

$$\pi_4 = \omega_d^\theta R_d^\eta h_o = \left(\frac{rads}{T} \right)^\theta L^\eta L = L^0 T^0$$

$$T: -\theta = 0 \rightarrow \theta = 0$$

$$L: \eta + 1 = 0 \rightarrow \eta = -1$$

aspect ratio,

$$\pi_4 = \frac{h_o}{R_d}$$

and

$$\pi_5 = N$$

is the state number.

Hence the phenomenon can be stated equivalently with the following functional

relationship,

$$\frac{\omega_p}{\omega_d} = fn \left\{ Fr^2 \frac{h_o}{R_d}, Re, \frac{h_o}{R_d}, N \right\}$$

or

$$\frac{\omega_p}{\omega_d} = fn \left\{ Fr', Re, \frac{h_o}{R_d}, N \right\}$$

or

$$\frac{\omega_p}{\omega_d} = fn \left\{ Fr', Ta, \frac{h_o}{R_d}, N \right\}$$

Previous experiments using water have shown that the dispersion velocity ratio ω_p / ω_d was constant and equal to 1/3. This will be examined in the section (4.2, results) for the oils under consideration.

3 Experimental Apparatus Instrumentation and Procedure

3.1 The Experimental Apparatus

The present exploratory experiments were conducted at the Concordia's Fluid Dynamics Research Laboratory using the apparatus, which is schematically shown in Fig. 6.

The liquid vortex agitator apparatus consists of a DC electric motor, is linked to the shaft using a belt. A flywheel attached to the shaft dampens any possible fluctuations of the angular velocity of the axle. An aluminum disk with the specifications given in Fig. 6, is firmly attached to axle, which imparts angular velocity to the fluid placed inside a plexiglass container. The gap between the disk and the wall of the containing vessel (284 mm) is relatively small in comparison to the disk diameter 286 mm. Since the last clearance is indeed small i.e. $(D_t - D_d)/D_t = 0.007$ the evolving phenomenon unfolds in a stationary vessel with practically a rotating bottom plate. The flow evolution for the case where the disk does not cover the entire bottom can be found in Vatistas et al. (1992) and Wang (1995). As mentioned above, the shaft is driven through a belt pulley assembly by a DC motor, where its speed was regulated by a variac. The nominal specifications of the DC motor are:

- 3/4 Horse Power
- Speed range from 0 to 1750 RPM

Liquid can be poured into the container from the top and drained through a small hole at the bottom of the container.

A paper strip was placed at the center of the disk in order to calculate its rotational speed

accurately through image processing which will be described later.

A ruler, placed on the side of the container, as well as a vernier caliper, determined the liquid initial height, above the disk's surface.

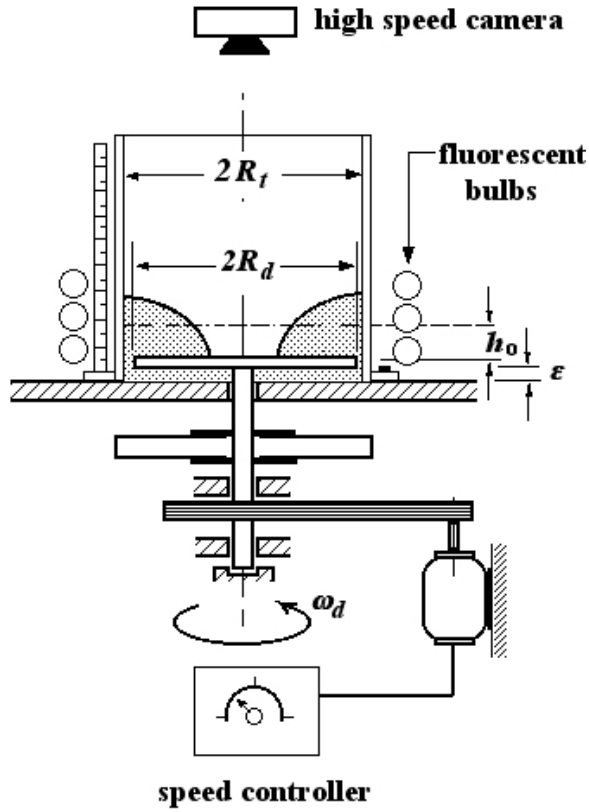


Figure 7. Diagram of the experimental apparatus, $R_t = 143$ mm and $R_d = 142$ mm. The clearance between the disk and the bottom plate (ϵ) was 28 mm while the disk's thickness was 9.525 mm.

3.2 The High-Speed Camera

As shown in Fig. 6, a PCO 1200hs high-speed camera was mounted and centered on top of the container with the specifications given below, is used to capture images of different patterns during the experiments:

- 636 fps at 1.3 MPixels full resolution
- 50 ns - 5 s exposure time range
- 75 ns inter-framing time
- 1280 x 1024 pixel
- USB 3.0, Camera Link, GigE / USB 2.0, IEEE1394

The Camware64 software was used to operate the camera. Using the previous software, based on the rotational speed of the fluid and disk, the exposure time was set appropriately to have the best possible resolution for the images and videos.

It needs to be mentioned that due to lack of internal memory of the camera, which was 4 GB, each time only a set of 4000 images that covered a period of 7.1 to 8 seconds were captured for each equilibrium state. The frequency of the camera was synchronized to the frequency of the disk.

3.3 The Lighting System

In order to take images with the best quality and maximum resolution it was necessary to have an appropriate lighting system. This is especially true when recording at high frequency, when the exposure time is low (close to 0.0125 seconds). With the assistance of two students from the Studio Arts Department of Concordia University, a lighting system consisting of three circular fluorescent bulbs each with 2600 lumens output were used in the experiments.

3.4 Description of the Oils

Three different oils made by the Exxon Mobile Company with the following specifications were used for the experiments:

- Spindle Oil with 22.69 cSt Kinematic Viscosity,
- H-22 Hydraulic Oil with 46.8 cSt Kinematic Viscosity,
- H-32 Hydraulic Oil with 64.75 cSt Kinematic Viscosity.

For each oil, three set of experiments with the initial heights of 8, 10 and 12 mm were conducted.

The viscosities of the oils were measured in the Fluid Mechanics Laboratory of Concordia University using Ostwald (or capillary) viscometers.

3.5 Procedure

3.5.1 General Description

As mentioned earlier, three different oils with viscosities ranging from 22 cSt to 65 cSt were involved in the experiments.

During each set of experiments two sequences were conducted:

- Ascending or spin-up sequence,
- Descending or spin-down sequence.

Prior to starting the ascending run and then setting the disk into rotation, the container was filled partially with one of the oils up to a certain initial height relative to the upper surface of disk. Then, rotation was imparted to the fluid by the disk. This caused the central part of disk surface to be exposed to air and consequently the interfacial line of oil, the disk surface, and air outlined the equilibrium states. The disk speed was increased by small amounts (~5 rpm each time) with a pause in between.

In the beginning, as the disk started to rotate, in the counter-clockwise direction, the central portion of the oil free surface touched the disk and a circular shape appeared. As the speed was increased slowly, the circle got wider, and its radius enlarged proportionally to the disk's velocity. Later on, two warped curves emerged one on top of the other. One is the interface between the fluid and the container's wall and the other was a curve that acted as the boundary between the two elevations. Hence, a further speed increment results in appearance of a circular region in which behaved as a rope. Later on, the rope started to have torsion while rotating in same direction as the disk. This behavior could be understood to be the result of liquid movement in three-dimensions. The first was the liquid's rotary motion in the radial-azimuth plane, while the other that taking place in the axial direction. It is the first that causes the forming of the different equilibrium patterns that will be described later.

3.5.2 Estimation of Experimental Uncertainties Associated with the Measurements

During the tests different parameters were recorded. Since each variable had its own percentage of uncertainty they must be estimated separately.

In order to measure the liquid initial height above the disk's upper surface, a ruler, placed

on the side of the container, and a vernier caliper were used. Therefore, there must be a percentage uncertainty associated with the measurement. Based on the provided specifications by the manufacturer, the Vernier had an accuracy of 0.02 mm. Since three different heights were considered in the experiment, there will be three different uncertainties associated with the measurement as following calculations:

$$\frac{|8 \text{ mm} - 8.02 \text{ mm}|}{8 \text{ mm}} = 0.0025 \Rightarrow 0.0025 \times 100 = 0.25 \%$$

$$\frac{|10 \text{ mm} - 10.02 \text{ mm}|}{10 \text{ mm}} = 0.002 \Rightarrow 0.002 \times 100 = 0.2 \%$$

$$\frac{|12 \text{ mm} - 12.02 \text{ mm}|}{12 \text{ mm}} = 0.0017 \Rightarrow 0.0017 \times 100 = 0.17 \%$$

The other parameter has to do with the disk speed. In order to determine accurately the rotational speed of the disk, a band was placed across the center of the disk see Fig. 7. Having the camera's frequency from the camera's software, a MATLAB code was employed to calculate the disk speed. By comparing the strip location in the first image to the image in which the strip underwent a full revolution (the band returning to the same location) the speed of disk was computed. The figure below (Fig. 7) illustrates the procedure for one of the cases.

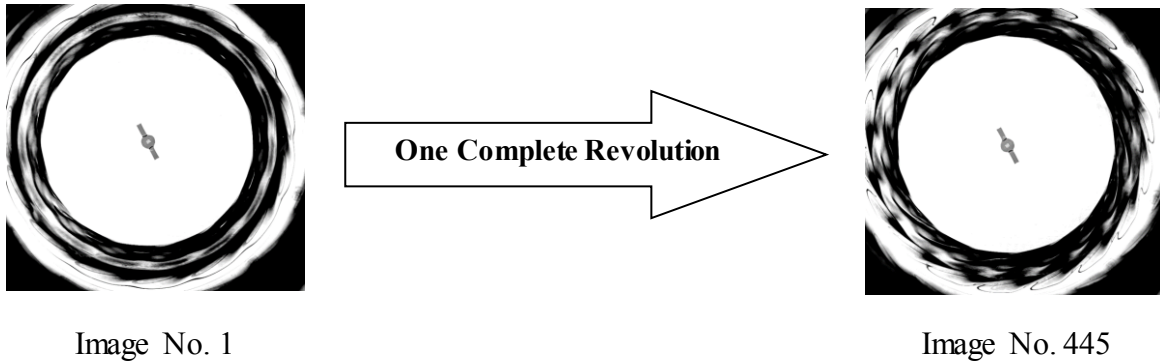


Figure 8. One Complete Revolution of the Pattern

In this case, having the camera's frequency, the following calculations can be conducted to determine the speed of the disk:

$$\begin{aligned}
 fr = 548.95 \text{ Hz} &\Rightarrow T = \frac{1}{fr} = 0.00182 \text{ s} \Rightarrow \text{No. of the last image} = 445 \\
 &\Rightarrow \text{Time for one complete revolution} = 445 \times 0.00182 \text{ s} = 0.8099 \text{ s} \\
 &\Rightarrow \text{To convert into rpm} \Rightarrow \frac{60}{0.8099} = 74.08 \text{ rpm}
 \end{aligned}$$

Based on the above computations, there could be an error of ± 1 image in detecting the correct image number in which a complete revolution occurred. For instance, in the above example, the full revolution could have happened in the image number 444 instead of 445. Therefore, the uncertainty is calculated as follows:

$$\frac{|445 - 444|}{444} = 0.00225 \times 100 = 0.225 \%$$

Of course, the uncertainties will depend on the disk speed. Overall however, it was found to lie between 0.142 - 0.714%. To sum up, the maximum amount of uncertainty for this type of measurement (in all the cases) was found not to exceed 1%.

4 Results and Discussion

Past experiments with smaller disks, using water as the working fluid have shown that the equilibrium patterns show up in sequence with the disk speed, that they were also marked by intervals of mixed-states see Fig. 3. A small degree of hysteresis (~5%) also existed during the spin-up and spin-down schedules Vatistas et al. (2001). This will be shown here that it is not the case in oil vortices

4.1 Evolution of Equilibrium States

4.1.1 Spindle Oil

4.1.1.1 Spindle Oil 8 mm initial height – Ascending Sequence

First, the events during the spin-up process using spindle oil and an initial height (h_o) of 8 mm are to be described. Prior to the experiment, starting from rest, the free surface of the oil surface was horizontal (no centrifugal force was present). The disk was then set into rotation by gradual adjustments of the variac in steps of 5 rpm. Due to the combination of gravitational and centrifugal accelerations the central part of the liquid level was lowered, it touched the disk, and at 41.7 rpm a diffused circular contact line was formed as shown in Fig. 9(a). As the disk speed was elevated to 52 rpm, the oil-disk-air interface migrated towards container's wall and the mean radius of the circular pattern enlarged, and then became more noticeable as it is illustrated in Fig. 9(b). One more image of the circular shape at a higher disk speed (62 rpm) with even larger radius was obtained see Fig. 9(c).

Continuing to increase the speed to 76.5 rpm, the circular shape lost its stability and transformed into the smooth “fat” steady triangle pattern or $N = 3+$ shown in Fig. 9(d). The

number refers to the state and the plus sign indicates that the wave rotates in the same direction as the fluid (or it is co-grade¹). The shape had a lower angular velocity than the disk, which increased with the disk speed. As a result of larger centrifugal force, the pattern got larger when the disk speed was increased to 85.3 rpms see Fig. 9(e).

At approximately 91.2 rpm, the core became once more a circle see Fig. 9(f). The circular shape lasted up to 109.3 rpm at which point the pattern underwent a fast transition to $N = 15+$. The new equilibrium state was stable with sharp edges as illustrated in Fig. 9(g). In order to investigate the bifurcations at a specific equilibrium, the fluid was disturbed by the introduction of a cylindrical rod into the rotating fluid. In case that the existing pattern underwent notable change in its structure, it was concluded that at this specific speed, multiple patterns (or bifurcations) exist under the same boundary conditions. If by disturbing the flow field four times, did not produce any significant change to the pattern's shape, it was concluded that there were no more possible equilibria at the same speed.

Continuing the ascending process, the pattern lost its stability giving rise to an $N = 15+$ possessing a higher angular velocity. There were no more changes in the last pattern up to just before 120.7 rpm. At the end of the interval the pattern switched rapidly into a stable $N = 18+$ polygonal shape with sharp edges as shown in Fig. 9(h). Disturbing the pattern at this point forced the $18+$ equilibrium state to transform into the $19+$ stationary polygonal pattern shown in Fig. 9(i). Once more, the bar was introduced into the fluid and the $19+$ equilibrium state changed into an $N = 18+$ pattern, see Fig. 9(j). Reintroducing the external disturbance four times did not make any further changes in the existing equilibrium state, and therefore it was concluded that at

¹ A negative sign after the number will indicate retrograde (i.e. counter rotating) state.

this speed there were no more bifurcated states.

The $N = 18+$ pattern remained stable up to 143.5 rpm. At this speed, it was observed that the $N = 18+$ was replaced by the stationary hexagon ($N = 6+$) shown in Fig. 7(k). The last basic pattern included three solitary waves or in short solitons² (having only a trough and no crest) sliding along the base equilibrium revolving with a constant velocity around it shown in Fig. 8. These were found to move in unison around the pattern with higher (than the pattern) but constant speed. Since this is a remarkable finding it will be discussed separately in section 4.1.2.

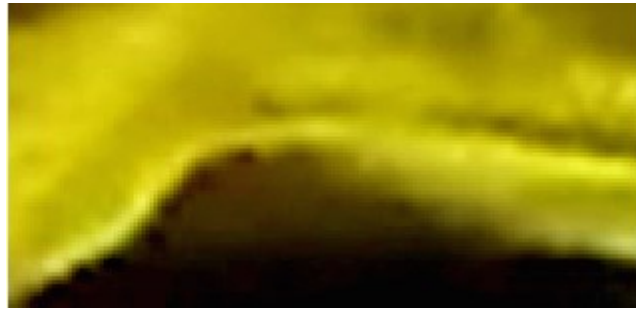


Figure 9. One image of a set of three rotating solitary waves

Increasing the disk speed, forced the $N = 6+$ to be replaced by an $N = 7+$ pattern at ~ 150 rpms as demonstrated in Fig. 9(l). Again, a solitary wave, but this time even weaker than before rotating around the main pattern was observed. One more set of images of the same $7+$ pattern at 152.8 rpm was captured see Fig. 9(m).

Augmenting the disk speed further lead to the appearance of an $N = 8+$ asymmetric polygonal pattern at 166.2 rpm as shown in Fig. 9(n). This equilibrium state persisted up to approximately 175.2 rpm and it appeared to lose stability due to strong secondary waves rotating

² One and two wave packets [Vatistas et al. (1992)], which later were classified as solitary waves [Wang (1995)] encircling the main pattern were encountered. These however were suspected but never substantiated.

around the main pattern as illustrated in Fig. 9(o). Beyond this point, the flow-field became turbulent and the pattern was plagued by a variety of different superimposed patterns. One more set of images was taken at 188.4 rpm as demonstrated in Fig. 9(p) exhibited the same characteristics. At this point, the ascending process was terminated. Table 1 provides the data of what was described before.

Table 1. Spindle Oil – 8mm Ascending Sequence Equilibria

| Disk Velocity (rpm) | Equilibria State (<i>N</i>) | Bifurcation | Figure (9) |
|--------------------------------|--|--------------------|-----------------------|
| 41.7 | Circle | NO | a |
| 52 | Circle | NO | b |
| 62 | Circle | NO | c |
| 76.5 | 3+ | NO | d |
| 85.3 | 3+ | NO | e |
| 91.2 | Circle | NO | f |
| 109.3 | 15+ | NO | g |
| 120.7 | 18+ | YES | h |
| 120.7 | 19+ | YES | i |
| 120.7 | 18+ | YES | j |
| 143.5 | 6 - Stationary | NO | k |
| 150.5 | 7+ | NO | l |
| 152.8 | 7+ | NO | m |
| 166.2 | 8+ | NO | n |
| 175.2 | 8+ | NO | o |
| 188.4 | 8+ | NO | p |

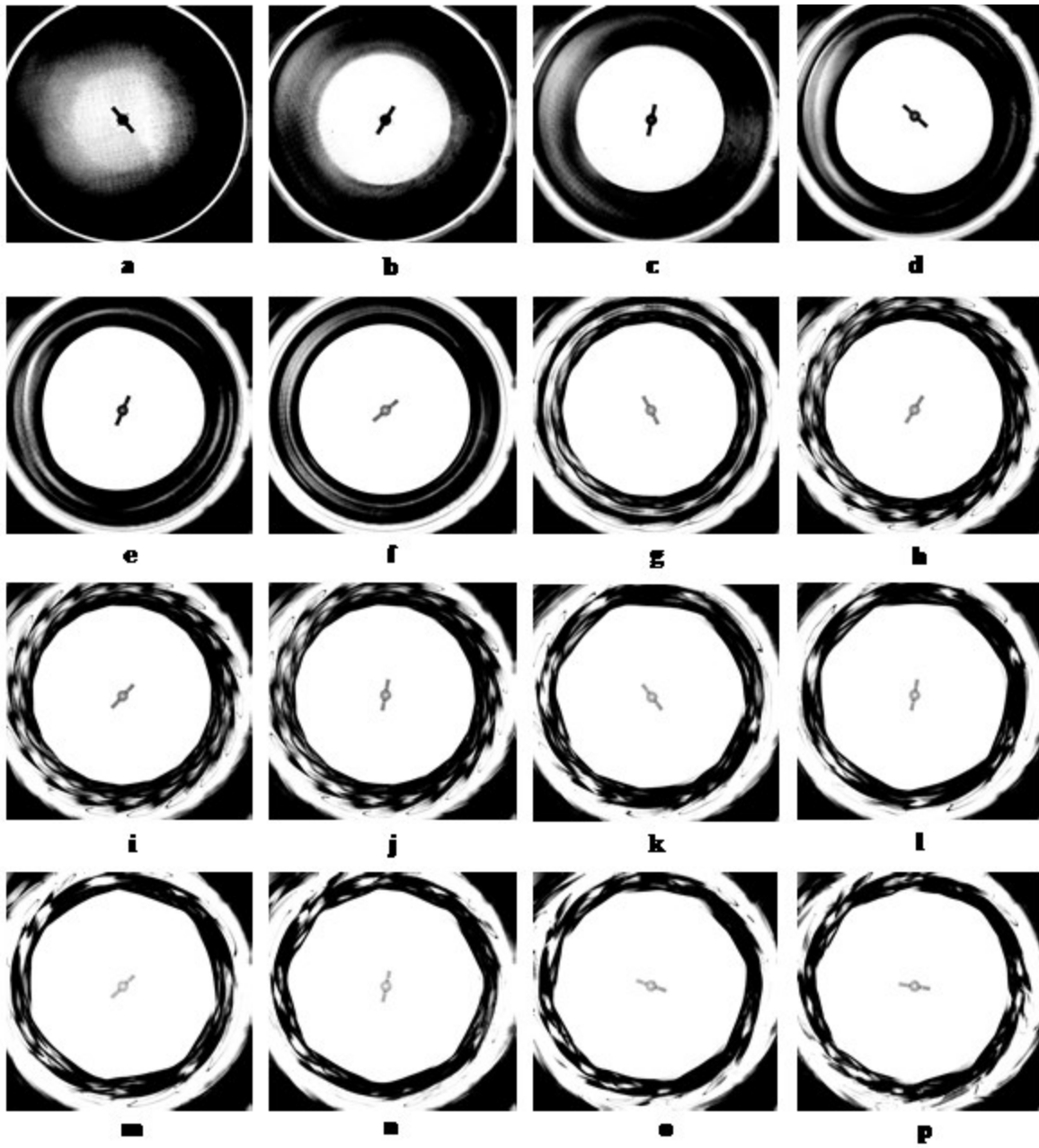


Figure 10. Spindle Oil (8mm) Ascending Sequence Actual Equilibria

4.1.1.2 Spindle Oil 8 mm initial height – Descending Sequence

Flow spin-down begun at the end of the spin-up state (188.4 rpm). The existing $N = 8+$ state remained with minor changes as shown in Fig. 10(a) taken at 167.1 rpm. Disturbing the pattern multiple times did not give any changes in the state and therefore no bifurcation existed at this speed.

Gradually reducing the disk speed, the $N = 8+$ remained unaltered until 156.8 rpm where a stable heptagon ($N = 7+$) developed see Fig. 10 (b). The heptagonal pattern seemed to be asymmetric having a relatively low angular velocity. No bifurcation observed at this point. An additional set of images of the $N = 7+$ equilibrium state was taken at 150.5 rpm see Fig. 10(c). Resuming the decent process down to 140 rpm, the previous pattern switched to the stationary hexagonal equilibrium state ($N = 6+$) shown in Fig. 10(d). External disturbance did not alter the shape.

Decreasing the disk speed slightly to 129.8 rpm, the stationary hexagon was replaced by the $N = 13+$ non-symmetrical polygonal pattern illustrated in Fig. 10(e). Unsteadiness was observable in the outer region of the pattern as well as on its edges. In addition, wobbling was detected in the outer periphery of the pattern. As the disk speed was decreased to 122.5 rpm, the existing pattern got steadier and symmetric as shown in Fig. 10(f). Upon rod introduction into the rotating fluid the stable symmetric 13+ pattern switched into a mixed pattern (Fig. 10(g)) that was modulated by several solitary waves. The same mixed pattern with multiple solitary waves persisted down to 107.2 rpm. Beyond this point the pattern was replaced by a smooth, symmetric and stable $N = 17+$ as shown in Fig. 10(h). One flow disturbance attempt made the $N = 17+$ pattern to turn into a symmetric and stable $N = 15+$ state see Fig. 10(i). Any further flow

disruptions did not yield any change in the existing state.

Driving the disk's angular velocity down to 96.4 rpm gave rise to a circular pattern (Fig. 10(j)) followed by a $N = 3+$ that appeared at 87.8 rpm (Fig. 10(k)). Reducing the disk speed further, the pattern got squeezed towards the axis of rotation at lower speeds (as illustrated in Fig. 10(l) at 76 rpm) and remained up to 61.4 rpm where it transformed into a plain smooth non-shivering circle as shown in Fig. 10(m). The existing circular shape pattern got smaller as the speed decreased to a point where it disappeared when the entire disk was flooded by the liquid. At this point, the experiment was terminated. Table 2, provides the data of what was described before. Fig.11 shows a schematic of typical equilibrium spectrum.

Table 2. Spindle Oil – 8mm Descending Sequence Equilibria

| Disk Velocity (rpm) | Equilibria State (N) | Bifurcation | Figure (10) |
|---------------------|----------------------|-------------|-------------|
| 167.1 | 8+ | NO | a |
| 156.8 | 7+ | NO | b |
| 150.5 | 7+ | NO | c |
| 140 | 6 - Stationary | NO | d |
| 129.8 | 13+ | NO | e |
| 122.5 | 13+ | NO | f |
| 122.5 | Mixed 11 -13 | NO | g |
| 107.2 | 17+ | YES | h |
| 107.2 | 15+ | YES | i |
| 96.4 | Circle | NO | j |
| 87.8 | 3+ | NO | k |
| 76 | 3+ | NO | l |
| 61.4 | Circle | NO | m |

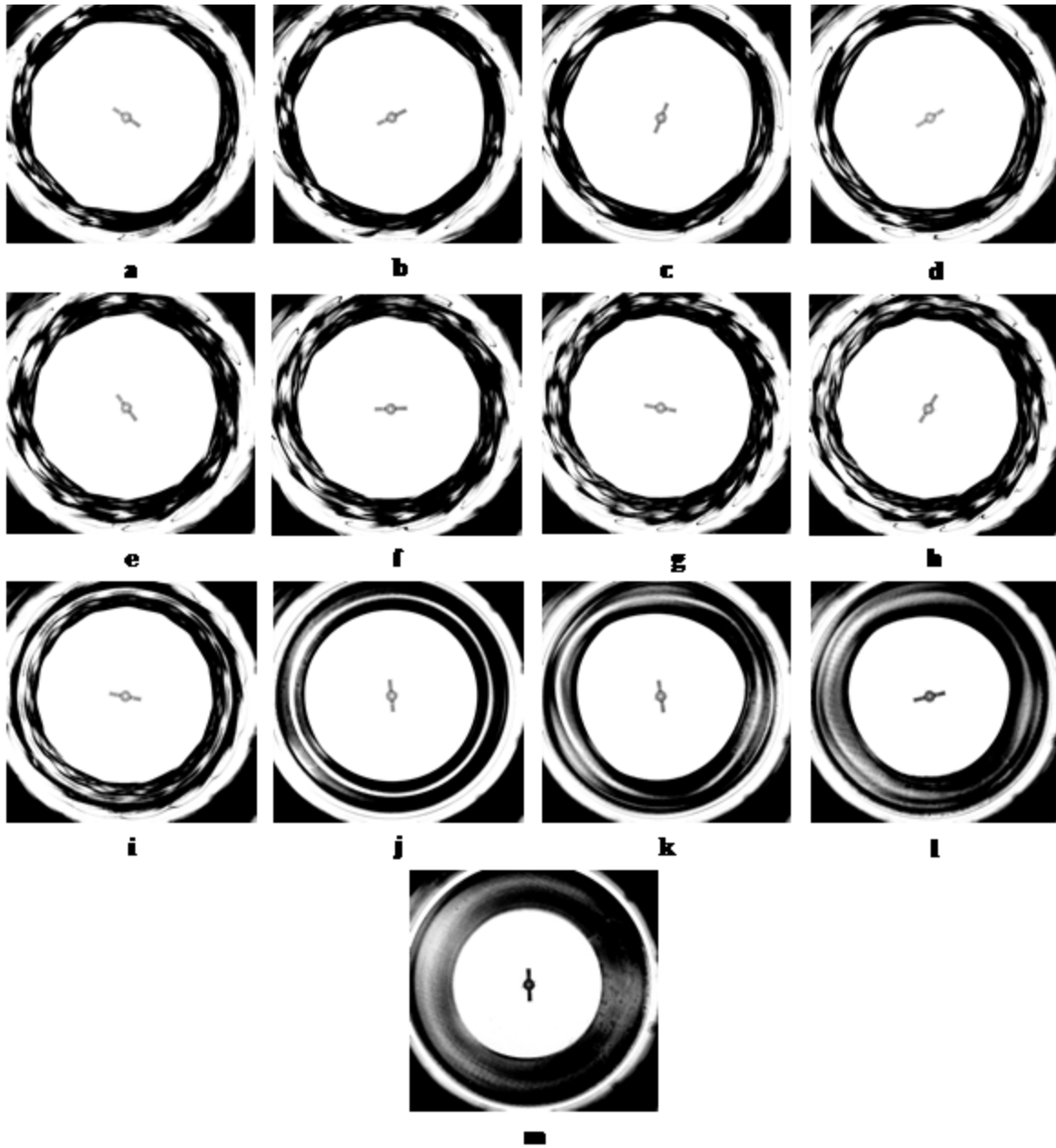


Figure 11. Spindle Oil (8mm) Descending Sequence Actual Equilibria

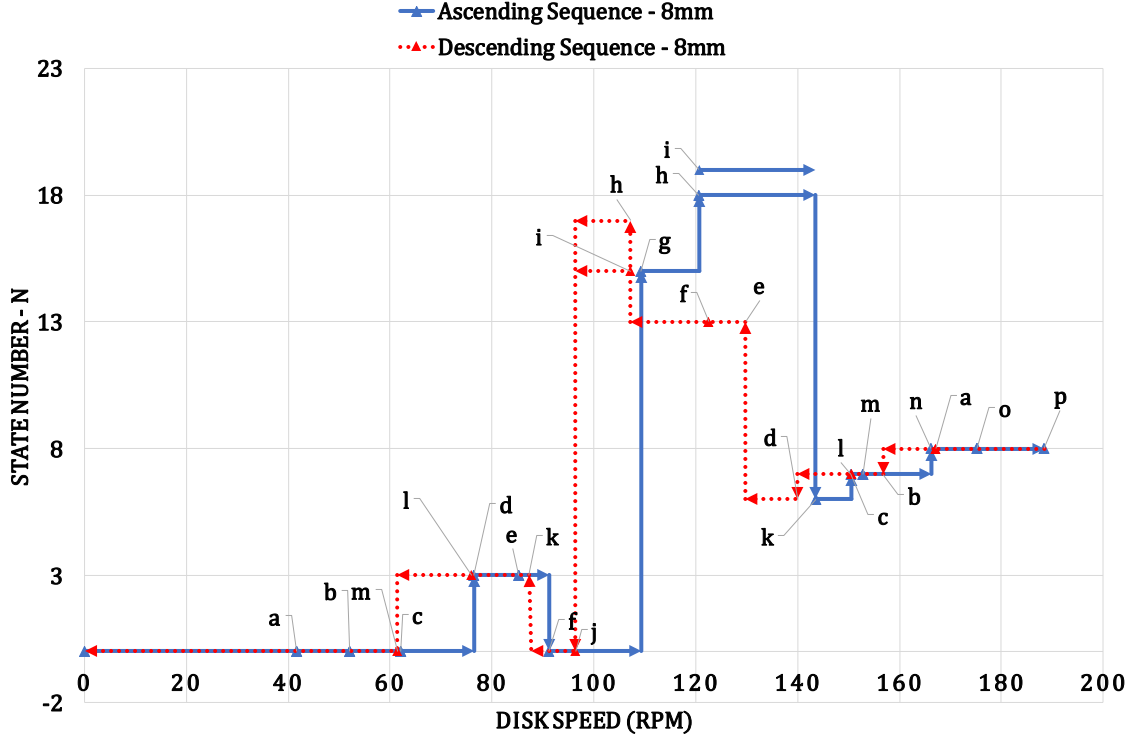


Figure 12. Spindle Oil (8mm) Schematic of Typical Equilibrium Spectrum

It is abundantly evident from the previous ascending and descending equilibrium spectra (Fig. 11) that flow exhibits very strong hysteresis.

4.1.1.3 Spindle Oil 10 mm initial height – Ascending Sequence

Next the ascending sequence for $h_o = 10$ mm keeping all other parameters the same will be discussed. Following a quasi-static increase of the disk speed from rest to 77.7 rpm, the circular interface (which is shown in Fig. 13(a) and (b)) was first replaced by a flattened $N = 2+$ stable pattern at the end shown in Fig. 13(c). It should be mentioned that as the disk speed increased, the $N = 2+$ equilibrium state expanded towards the container's wall and its phase speed increased. This lasted up to 86.4 rpm where it switched into the co-grade triangle ($N = 3+$) shown in Fig. 13(d). The previous state persisted within a range of 13 rpm where it transformed into a

circular shape again that appeared quite solid but unsteady see Fig. 13(e). The unsteadiness of the $N = 0$ pattern is due to the presence of pulsating and wobbling temporal effects. The source of which can be attributed to the four-dimensional nature of the event, i.e. the phenomenon takes place in the radial, azimuth, axial, and time dimensions. Since the occurrences unfolded not under strictly shallow liquid conditions, the radial position of the interface (at $z = 0$ or on the disk) can be approximated by:

$$r_s = R + A \left\{ k \cos\left(\frac{r}{R}\right) + n \sin\left(\frac{z=0}{R}\right) - \omega t \right\}$$

Where: R is the radius of the undisturbed pattern on the disk's surface, A is the amplitude of the harmonic perturbation, k and n are the wave numbers in the radial and axial direction respectively, and ω is the angular velocity of the pattern.

Typical shapes of the patterns during pulsating³ and wobbling⁴ modes for different times are shown in Fig. 12(a) and (b). Therefore, the pulsating mode is triggered by the harmonic perturbation in the axial direction while the wobbling is due to precession of the vortex core.

³ Shape dilates and contracts at regular intervals.

⁴ Hypocycloid motion, a smaller circle that rolls in the periphery of a larger circle.

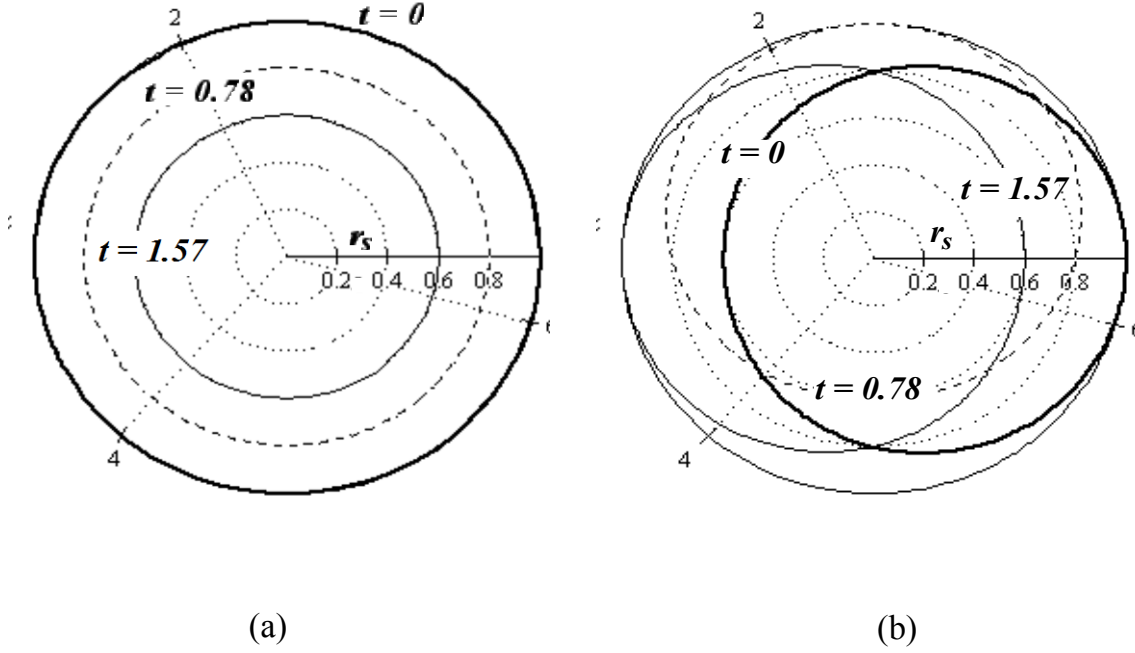


Figure 13. Typical shapes of the pattern shapes (a) of the pulsating mode ($A = 0.2$, $k = 0$, $n = 2$ and $\omega = 2$, for $z = 0$) and (b) wobbling (all are the same as previous but in this case $k = 1$).

Up to this point, although the flow field was disturbed, no bifurcations transpired. A further advancement of the disk speed, caused the circle to wobble and then it was replaced by an $N = 15+$ state (as shown in Fig. 13(f)) having two solitary waves rotating around it with a constant speed. No bifurcations were observed here either.

The previous pattern persisted up to 125.8 rpm and then it transformed into an $N = 13+$ polygonal pattern as illustrated in Fig. 13(g). The new 13+ possessed also a pulsating mode where a radial harmonic motion was also superimposed to the base pattern. At this point, after introducing a stick inside the fluid, the $N = 13+$ pattern switched to an $N = 12+$ equilibrium state as shown in Fig. 13(h), while the pulsating mode was still observable. This condition endured up to 154.7 rpm where through an abrupt transition a core pattern of $N = 7+$ arose. A sample image of the new heptagonal pattern is provided in Fig. 13(i). This co-grade heptagon appeared stable

possessing sharp edges. After disturbing the fluid, it switched to a mixed mode where both 7+ and 6+ patterns were observable (Fig. 13(j)).

Increasing the disk speed furthermore to 161.8 rpm, the mixed mode state became a pure $N = 7+$ equilibrium (Fig. 13(k)), which was asymmetric as previously. However, as the disk speed reached 171.5 rpm, the heptagon shape became unsteady (Fig 13(l)). The previous remained up to 193.9 rpm where a co-grade octagonal ($N = 8+$) came into view see Fig. 13(m). As the disk speed increased the 8+ pattern was still unsteady but with more pronoun shape fluctuations. The ascending procedure was continued up to 227.8 rpm where a state that consisted from a crowd of waves (Fig 13(n)) merged. At this point, spin-up run was halted. Table 3, provides the data of what was described before.

Table 3. Spindle Oil – 10mm Ascending Sequence Equilibria

| Disk Velocity (rpm) | Equilibria State (N) | Bifurcation | Figure (13) |
|------------------------|-----------------------------|-------------|----------------|
| 47.6 | Circle | NO | a |
| 62.8 | Circle | NO | b |
| 77.7 | 2+ | NO | c |
| 86.4 | 3+ | NO | d |
| 99 | Circle | NO | e |
| 117.2 | 15+ | NO | f |
| 125.8 | 13+ | YES | g |
| 125.8 | 12+ | YES | h |
| 154.4 | 7+ | YES | i |
| 154.4 | Mixed 7+ and 6+ | YES | j |
| 161.8 | 7+ | NO | k |
| 171.5 | 7+ | NO | l |
| 181 | 8+ | NO | m |
| 227.8 | Mixed of different states | NO | n |

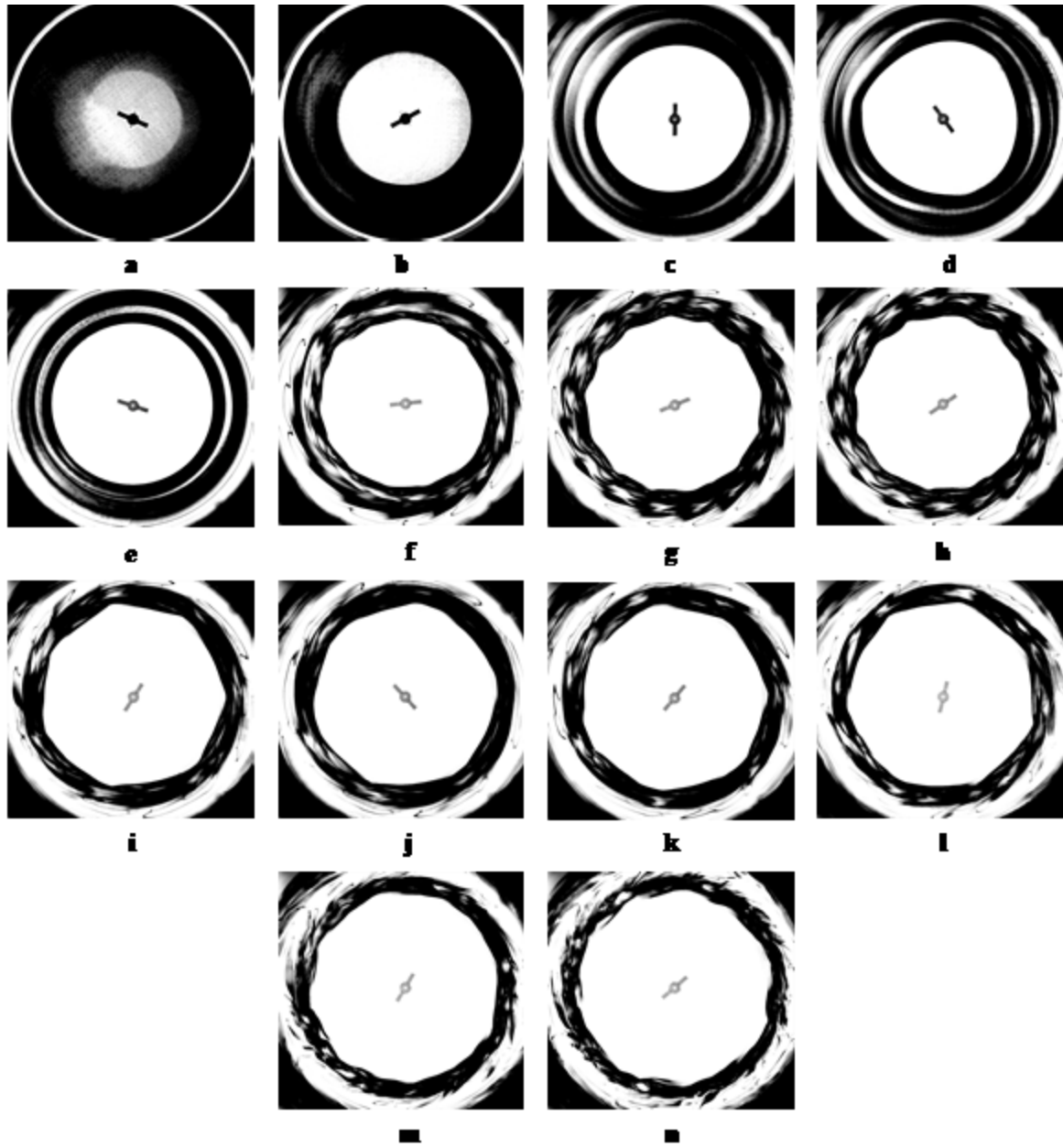


Figure 14. Spindle Oil (10mm) Ascending Sequence Actual Equilibria

4.1.1.4 10 mm initial height – Descending Sequence

Spinning down from 227.3 rpm to 181 rpm, a semi-steady asymmetric 8+ state appeared (Fig. 14(a)). As the disk speed was decreased, the pattern became more steady and symmetric, and at 172.4 rpm it transformed into a semi-stationary 7+ state as shown in Fig. 14(b). The

existing $N = 7+$ state persisted down to 152 rpm where a co-grade steady heptagon showed up (Fig. 14(c)). Later on, after further decrease in speed, the previous state transformed into a co-grade hexagon as illustrated in Fig. 14(d). The $N = 6+$ pattern had a very low angular velocity. So, it was not possible to have a complete revolution through the images due to lack of camera's internal memory. Due to the last impediment it was only possible to obtain recordings for half a revolution.

A further speed decrement down to 134.6 rpm caused the $N = 6+$ state to disappear and instead, a smooth and stable retrograde pentagon pattern emerged (Fig. 14(e)). Note that Wang (1995) had previously observed retrograde triangular, square, and pentagonal vortex cores, in the same apparatus with lower viscosity oil and smaller disk (126 mm). The present $N = 5-$ was harmonically modulated by small amplitudes waves. The retrograde pentagon pattern survived down to 125.8 rpm where it was replaced by a mixed state pattern (Fig. 14(f)), with states $16+$ and $17+$. Bifurcation was observed at this point, where upon flow disturbance the existing pattern switched to another mixed state (of $11+$ and $13+$ as shown in Fig. 14(g)) with at least six solitary waves going around the core, after disturbing the flow with the externally applied rod. Four more attempts to disturb the pattern, no more bifurcations were observed.

Reducing the speed to 114.3 rpm, a fifteen-sided co-grade polygonal pattern appeared see Fig. 14(h). The $N = 15+$ equilibrium state had two distinct characteristics. The first involved one weak solitary wave traveling around the main pattern, and the other one was the presence of an observable (from the video recordings) pulsating mode. As the disk speed decreased to 107.7 rpm, the $N = 15+$ pattern became more steady, the solitary wave disappeared and the pulsating mode terminated as shown in Fig. 14(i). The previous state persisted down to 104.4 rpm where it

transformed into a pulsating circle (Fig. 14(j)). Disturbing the flow four times yielded no changes to the existing state precipitated, therefore no bifurcation states exists at this point. However, as the disk speed decreased to 87.3 rpm, a co-grade triangle became evident (Fig. 14(k)). The triangle had a high frequency of rotation. As the speed reduction continued, the sides of the $N = 3+$ state curved in towards the disk center and then at 65.2 rpm it transformed into a circle (Fig. 14(l)). Two sets of images at 65.2 rpm and 48.2 rpm of the circular shape were taken in order to show the effects of speed on its radius (Fig. 14(l) and (m)). At this point the experiments were terminated because the fluid flooded the entire disk surface. Table 4, provides the data of what was described before. Fig.15 shows a schematic of typical equilibrium spectrum.

Table 4. Spindle Oil – 10mm Descending Sequence Equilibria

| Disk Velocity (rpm) | Equilibria State (N) | Bifurcation | Figure (14) |
|---------------------|--------------------------|-------------|-------------|
| 181 | 8+ | NO | a |
| 172.4 | 7+ | NO | b |
| 152 | 7+ | NO | c |
| 143.3 | 6+ | NO | d |
| 134.6 | 5- | NO | e |
| 125.8 | Mixed 16+ and 17+ | NO | f |
| 125.8 | Mixed 11+ and 13+ | NO | g |
| 114.3 | 15+ | NO | h |
| 107.7 | 15+ | NO | i |
| 104.4 | Circle | NO | j |
| 87.3 | 3+ | NO | k |
| 65.2 | Circle | NO | l |
| 48.2 | Circle | NO | m |

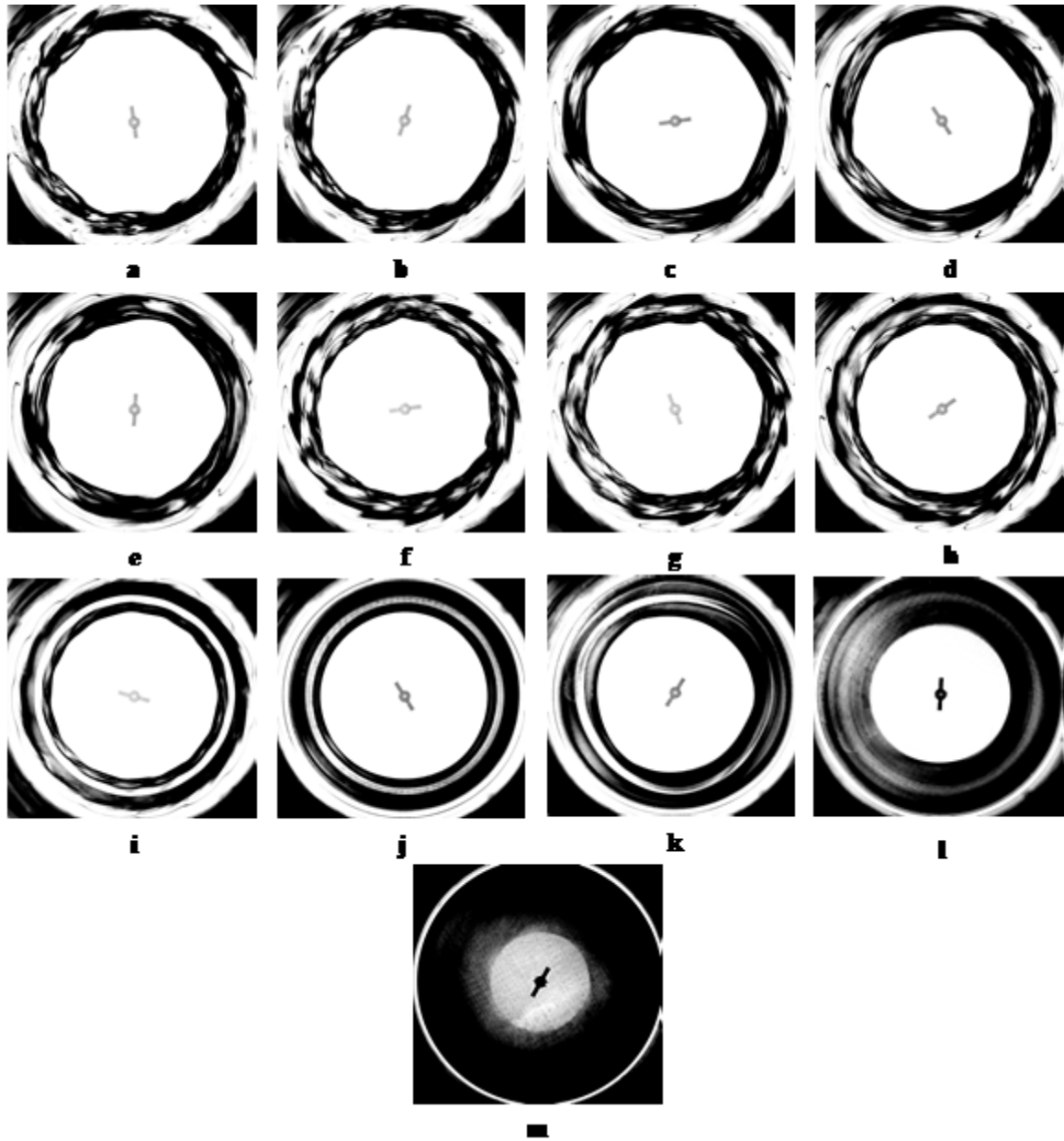


Figure 15. Spindle Oil (10mm) Descending Sequence Actual Equilibria

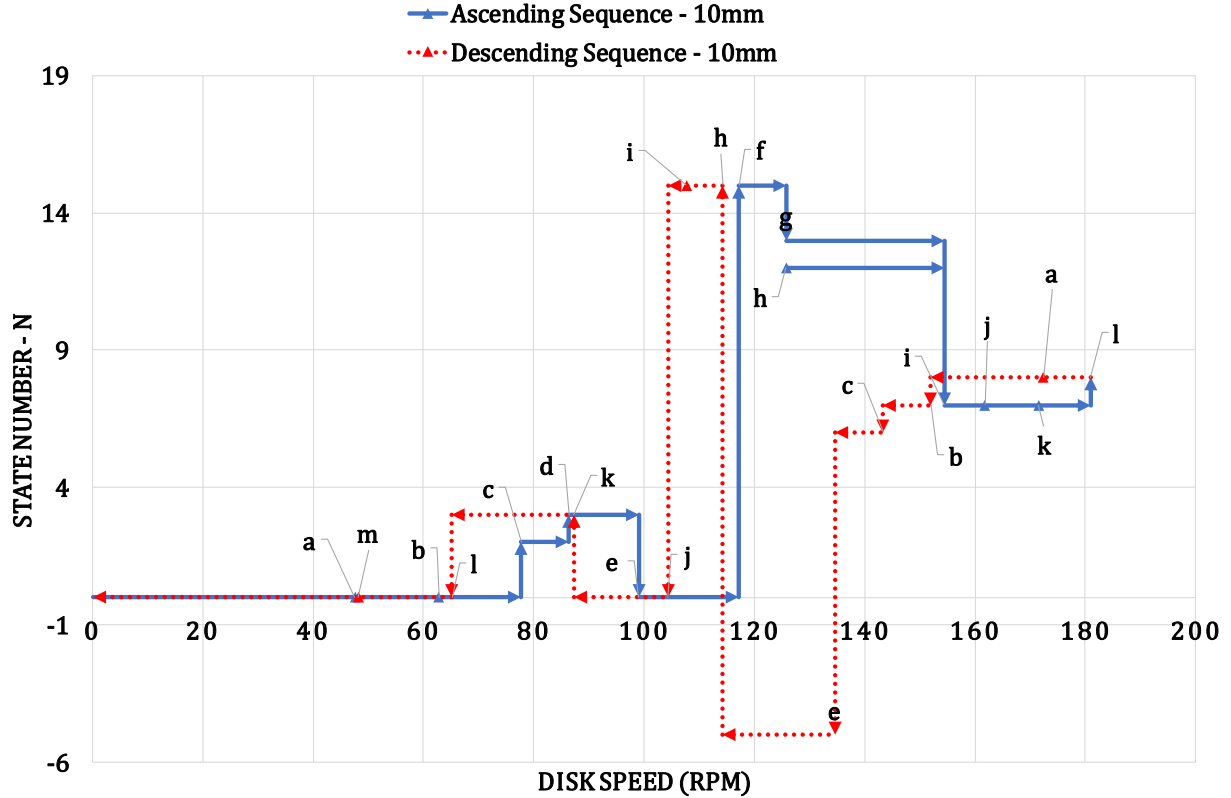


Figure 16. Spindle Oil (10mm) Schematic of Typical Equilibrium Spectrum

4.1.1.5 12 mm initial height – Ascending Sequence

Quasi-static increase of the disk speed from rest to 64.8 rpm, the circular dim $N = 0$ silhouette (Fig. 16(a)) was first noticed. Between 0 to 64.8 rpm the shady circle underwent the flowing particular transformations. In the beginning, it looked the same as previously, however, as the speed was increased, multiple small but detectable edges appeared on its perimeter. Afterwards, a shadowy full pentagon shown in Fig. 16(b) appeared, but due to its undetectable shady edges, it was not possible to process the images. Then the pentagon was replaced by a fat rectangular pattern, which is shown in Fig. 16(c). At 71 rpm, an $N = 8+$ state came into sight (Fig. 16(d)).

Continuing to increase the disk speed furthermore, at 80.4 rpm a noticeable 2+ solid equilibrium state appeared and persisted up to 103.4 rpm. Two sets of images (Fig. 16(e) and (f)) at 80.4 and 95 rpm were taken to demonstrate that by increasing the disk speed the $N = 2+$ pattern became fuller. This flow state however changed into a pulsating circle at 103.4 rpm (Fig. 16(g)).

At 125.3 rpm, the pulsating circular pattern was replaced by an asymmetric co-grade eleven-sided polygonal state (Fig. 16(h)). Disturbing the existing pattern led to a 13+ symmetric pattern as illustrated in Fig. 16(i). Therefore, a bifurcation existed in this situation.

From 125.3 to 141.7 rpm no further changes took place. But, beyond this point, a non-symmetric co-grade $N = 9+$ equilibrium state was observed (Fig. 16(j)). Increasing the disk speed forced the $N = 9+$ pattern to get more erratic under the presence of significant secondary waves. At 170.6 rpm, it seemed that fluid was going towards a mixed and unpredictable phase (Fig. 16(k)), hence, ascending procedure was terminated. Table 5, provides the data of what was described before.

Table 5. Spindle Oil – 12mm Ascending Sequence Equilibria

| Disk Velocity (rpm) | Equilibria State (N) | Bifurcation | Figure (16) |
|---------------------|--------------------------|-------------|-------------|
| 51.3 | Circle | NO | a |
| 59.3 | Circle | NO | b |
| 64.8 | Circle | NO | c |
| 71 | 8+ | NO | d |
| 80.4 | 2+ | NO | e |
| 95 | 2+ | NO | f |
| 103.4 | Circle | NO | g |
| 125.3 | 11+ | YES | h |
| 125.3 | 13+ | YES | i |
| 141.7 | 9+ | NO | j |
| 170.6 | 9+ | NO | k |

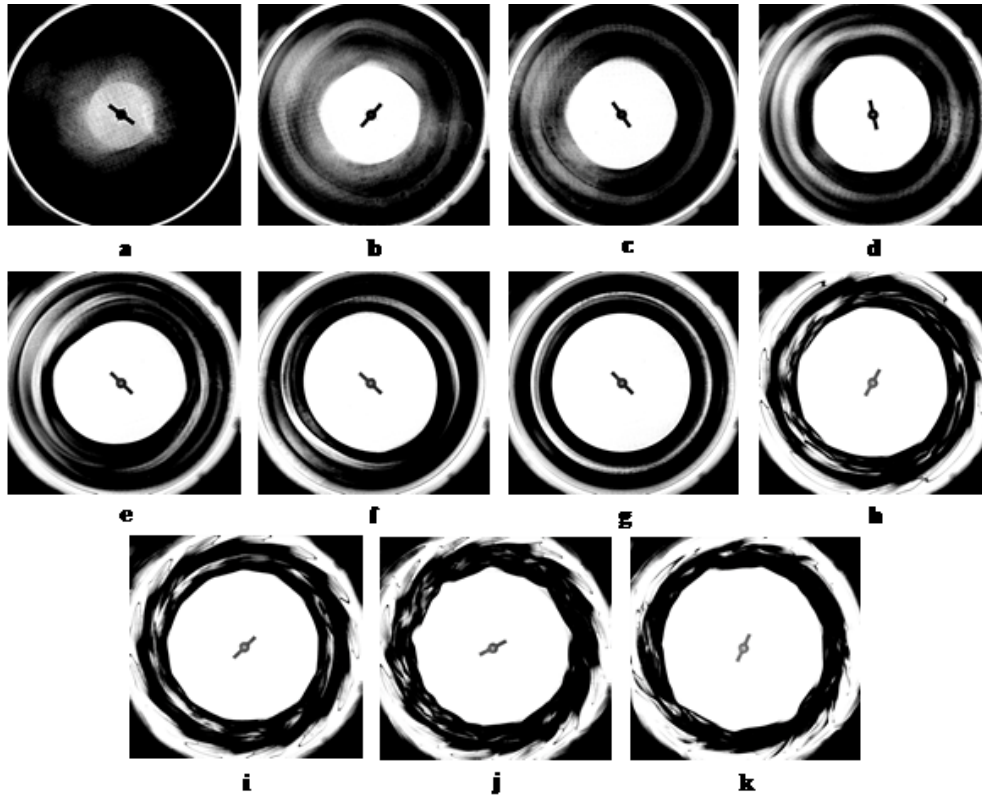


Figure 17. Spindle Oil (12mm) Ascending Sequence Actual Equilibria

4.1.1.6 Spindle Oil 12 mm initial height– Descending Sequence

Starting from 170.6 rpm, where the $N = 9+$ pattern resided, the spin-down process begun.

At 131.9 rpm, the core transformed into a co-grade $N=13+$ state as demonstrated in Fig. 17(c). Decreasing the speed to 131.9 rpm the 9+ pattern became calmer, and at 145.4 rpm a single solitary wave developed (Fig. 17(a)). Bifurcation transpired at 145.4 rpm where a mixed unstable state with $N = 7+, 9+$ and $11+$, see Fig. 17(b)) appeared. The unsteadiness was due to the solitary wave moving around the core.

As mentioned above, at 131.9 rpm a co-grade stable thirteen-sided equilibrium pattern ($N = 13+$) showed up. The first attempt of disturbing the pattern led to a 14+ pattern, which was quite sturdy see Fig. 17(d). A second disturbance, led into a 12+ semi-steady pattern (Fig. 17(e)). The unsteadiness was due to a secondary wave that existed on the surface of the fluid. A third agitation caused the existing 12+ equilibrium state to switch again to the previous 13+ while an additional external disturbance made the 13+ state to jump into a 14+ again.

Further speed reduction to 121.6 rpm, the 14+ gave away into an $N = 13+$ polygonal pattern (Fig. 17(f)). Two more states were observed at this speed. The first was a stationary decagon $N = 10+$ (Fig. 17(g)) which appeared after the first flow disturbance. A second disturbance resulted into a third state, which was a stable symmetric 14+ as illustrated in Fig. 17(h). Continuing the speed reduction, a pulsating circle appeared at 106.8 rpm (Fig. 17(i)). It needs to be included that as the disk speed was decreasing, the 14+ equilibrium state lost its stability as it was traversing a transient phase and it finally was replaced by a pulsating circular core. No bifurcation observed here. Finally, at 81.4 rpm, the circular shape transformed into a steady $N = 2+$ (Fig. 17(j)).

Further speed decrement caused the oval pattern to be replaced by a circular shape at 68.7 rpm (Fig. 17(k)). The new circular pattern however looked shady with noticeable edges. It

is quite similar to the shady 8+, which was found at 71 rpm during the ascending procedure. Although eight edges are visible, due to its low definition, it was difficult to extract the contour of the pattern.

As the disk speed decreased furthermore to 57.4 rpm, shady edges of exiting pattern were disappeared, and it transformed to a circular shape (Fig. 17(l)) that persisted until the liquid covered the whole surface of the disk. At this point the experiment was terminated. Table 6, provides the data of what was described before. Fig.18 shows a schematic of typical equilibrium spectrum.

Table 6. Spindle Oil – 12mm Descending Sequence Equilibria

| Disk Velocity (rpm) | Equilibria State (<i>N</i>) | Bifurcation | Figure (17) |
|--------------------------------|--|--------------------|------------------------|
| 145.4 | 9+ | NO | a |
| 145.4 | Mixed 7+, 9+ and 11+ | NO | b |
| 131.9 | 13+ | YES | c |
| 131.9 | 14+ | YES | d |
| 131.9 | 12+ | YES | e |
| 121.6 | 13+ | YES | f |
| 121.6 | 10+ | YES | g |
| 121.6 | 14+ | YES | h |
| 106.8 | Circle | NO | i |
| 81.4 | 2+ | NO | j |
| 68.7 | 8+ | NO | k |
| 57.4 | Circle | NO | l |

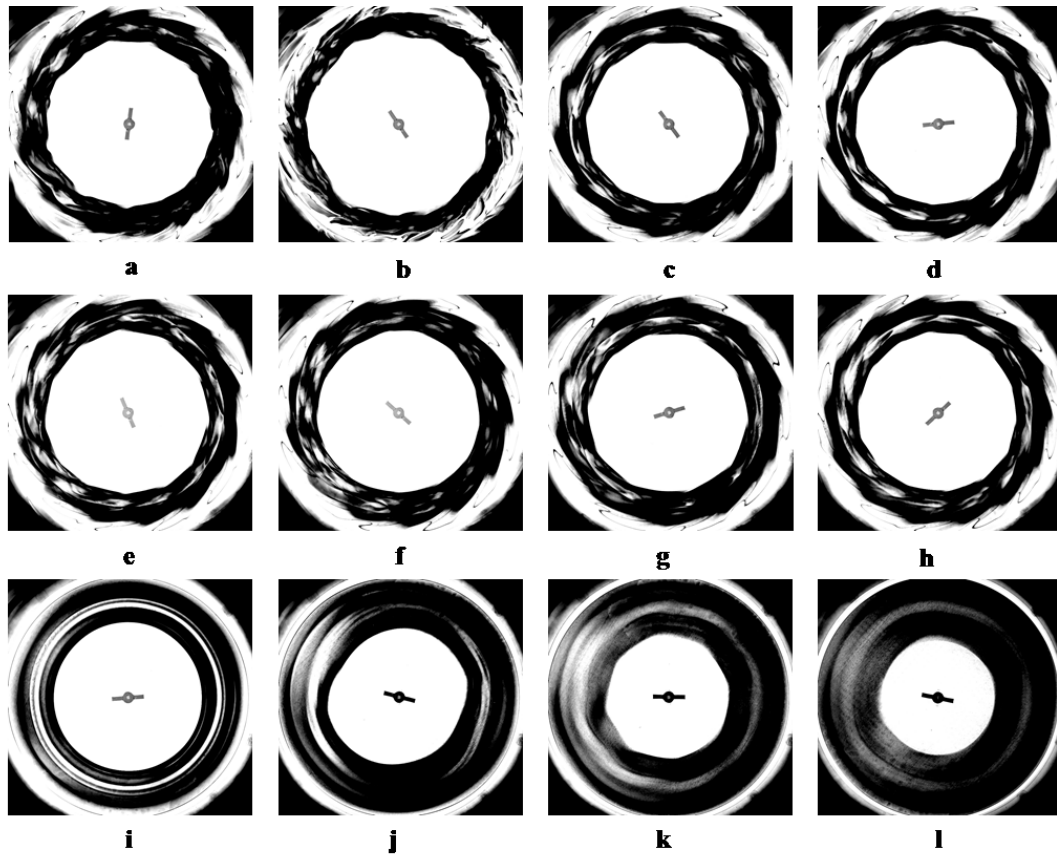


Figure 18. Spindle Oil (12mm) Descending Sequence Actual Equilibria

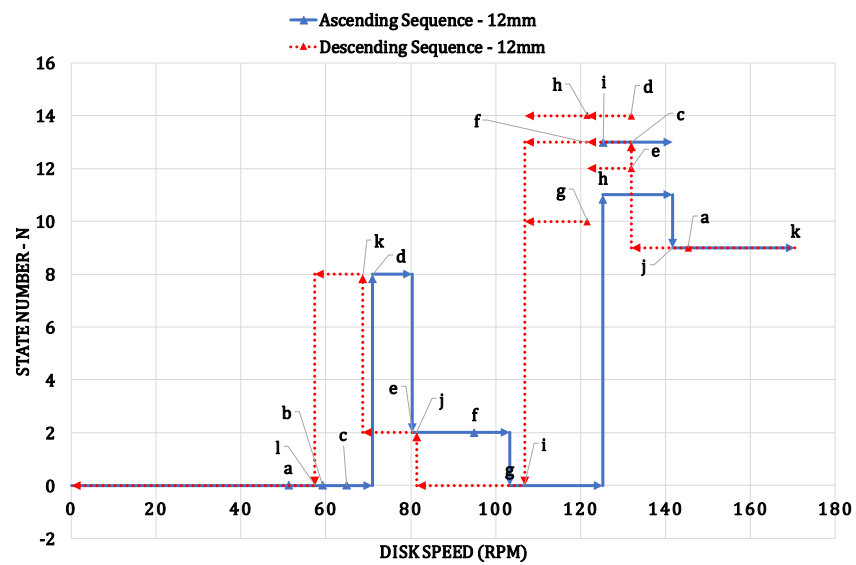


Figure 19. Spindle Oil (12mm) Schematic of Typical Equilibrium Spectrum

A three-dimensional figure representing *Taylor No.* versus N with $\frac{h_0}{R_d}$ ratio is shown in Fig. 19.

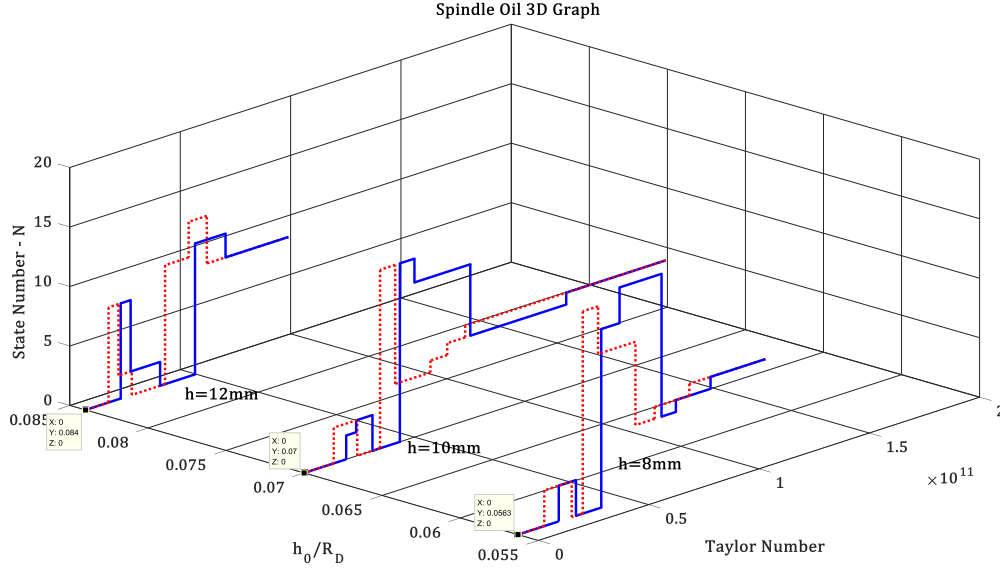


Figure 20. Spindle Oil 3D Graph Representing *Taylor's No.* versus N and $\frac{h_0}{R_d}$ ratio

4.1.2 Clusters of Synchronized Rotating Single Depression Solitons in Polygonal Formations

A solitary wave is a special type of undulation in a dispersive medium that consists from either a single isolated elevation (crest) or depression (trough).

Succeeding the discovery of the grand “Wave of Translation” by Russell in 1844, the event lied dormant for approximately one hundred years and resurfaced again in the nineteen sixties. Since then, single hydraulic waves in translation i.e. solitary waves (or popularly known as

tsunamis⁵) became of interest to a variety of areas of classical hydrodynamics. In addition, the phenomenon is also of relevance (by analogy) to plasma waves, acoustics, flow of granular chains, fiber optics, electrical and mechanical transmission lines, lattice dynamics, and many others.

It is interesting to note a propos that the first solitary wave of the single elevation type, in pure rotation, was first reported by Vatistas (1990), and the subsequently studies by the Concordia's fluid dynamics research team in 2011 and 2013 (A it Abderrahmane et al. (2011) and Amaouche et al. (2013) contributed to its better understanding.

In the present study, solitary waves of the single depression type were observed only in Spindle oil, see Fig. 20. They appeared suddenly and persisted within a range of disk speed in both the spin-up and spin-down schedules.

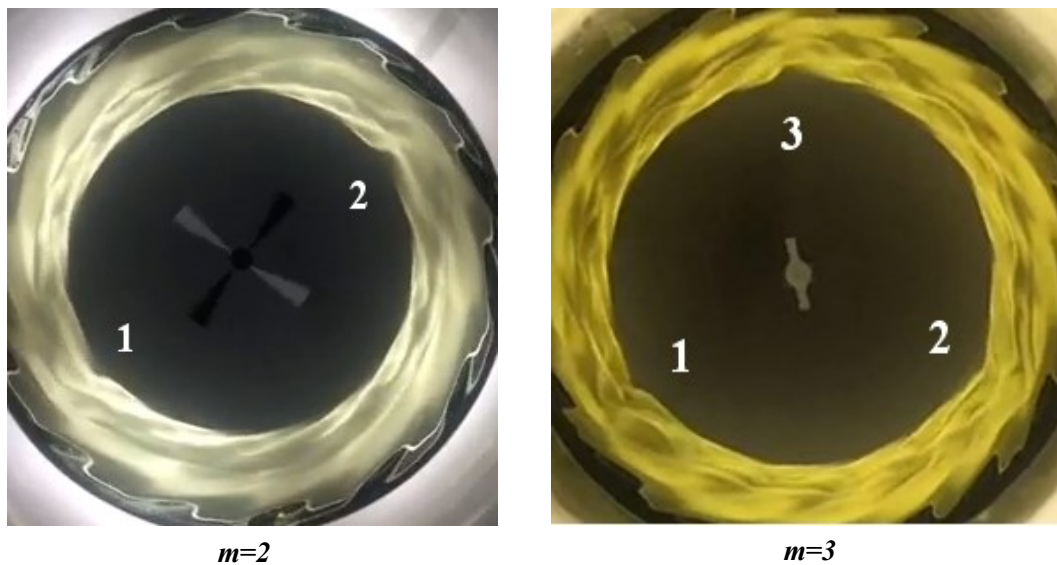


Figure 21. Clusters of $m = 2$, and 3 solitons frozen in time.

⁵ Tsunami is in Japanese is the harbor-wave.

Both their growth and annihilation were spontaneous, but in all the cases emerged and vanished in a similar fashion. At a critical disk speed, they arose by a localized rupture of the interface. Next, these entered into a circular orbit and progressively their movement was synchronized, finally positioning themselves on the same radius, around the host pattern, separated by equal angles (for 2 180° apart, for 3 120° , and for 6 60°) as shown in Fig. 21. If these are left undisturbed will rotate continuously. At the end of their endurance (at a second critical disk speed) they all coalescent into a specific point on the main pattern's contour and disappeared abruptly i.e. the same way as they appeared. Due to camera memory limitations it was not possible to examine in depth their temporal evolution and extinction phases.

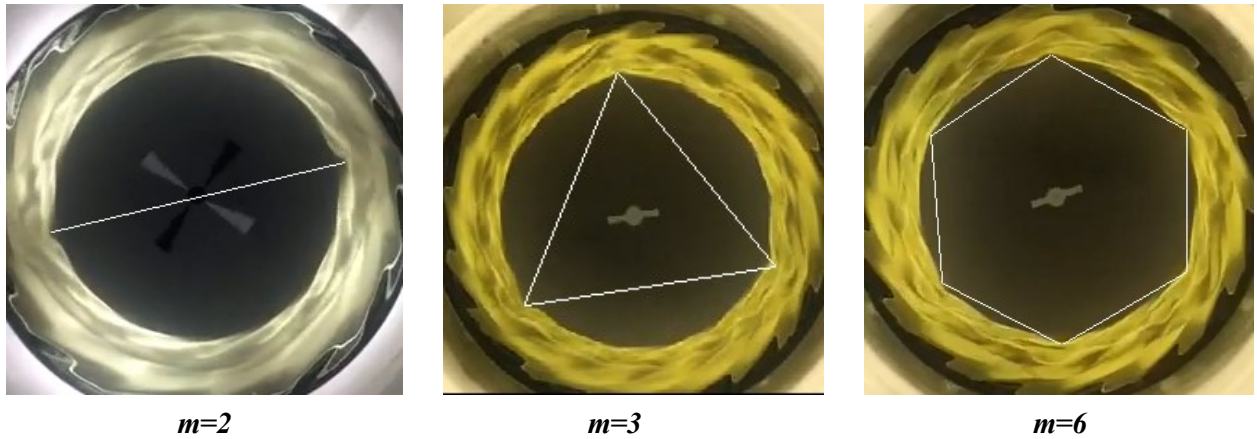


Figure 22. Solitary Waves with $m = 2, 3$ and 6 ($h_o = 10 \text{ mm}$)

The depth profile of one of these waves ($m = 2$) is shown in Fig. 22. The anticipated “Gaussian” free surface profile of the soliton $\eta = -\text{sech}^2(2x)$ correlates reasonably with the observed soliton shape.

The signatures of the solitons can be generated via image processing for all three cases as

shown in Fig. 23. Each peak represents a solitary wave passing through a fixed point. By subtracting the two values of the consecutive peaks, the period of the signal could be calculated.

For $m = 2$ the period of the signal is $0.5653 - 0.1234 = 0.4419$ s, or the frequency is $1/0.4419 = 2.263$ Hz. Because there are two waves present, the last frequency must be divided by 2, or $2.263/2 = 1.1315$ Hz. Similarly, the frequency of rotation for $m = 3$ and 6 are 1.1820 and 1.16 Hz respectively.

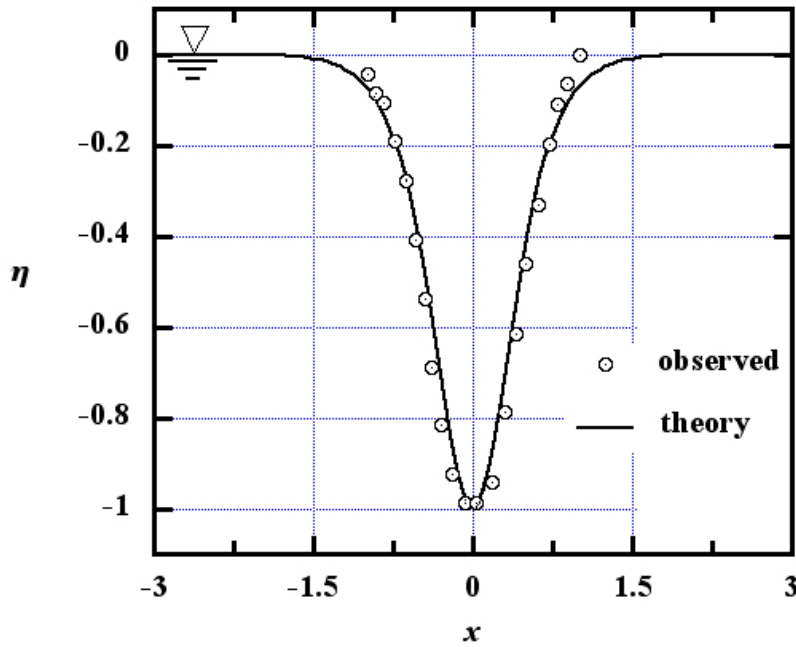


Figure 23. Gaussian free surface profile of the soliton

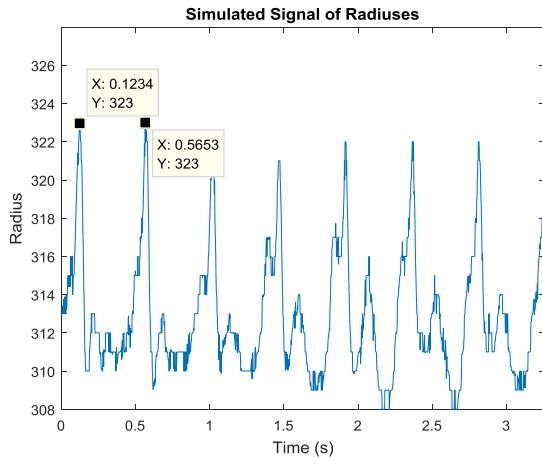
The ratio C' , defined as the solitary wave frequency divided by the frequency of the disk (ω_w / ω_d) could be calculated for each m (Equation 32, 33 and 34):

$$m = 2 \quad C' = 1.135 / 1.953 = 0.58$$

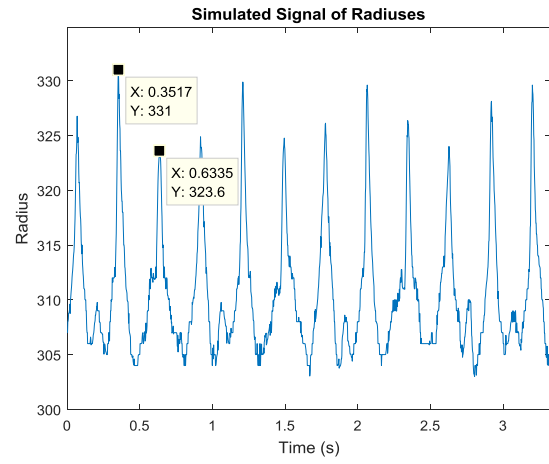
$$m = 3 \quad C' = 1.182 / 2.09 = 0.565$$

$$m = 6 \quad C' = 1.16 / 2.09 = 0.555$$

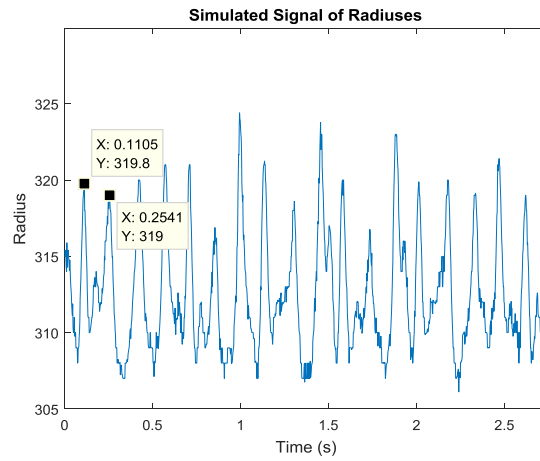
Therefore, the solitary waves rotate faster than the fluid but slower than the disk ($\sim 1/1.8$ times slower).



Signal spectrum – Solitary waves (2)



Signal spectrum – Solitary waves (3)



Signal spectrum – Solitary waves (6)

Figure 24. Signals of the Solitary waves ($h_o = 10 \text{ mm}$)

4.1.3 H-22 Hydraulic Oil

4.1.3.1 H-22 Hydraulic Oil 8 mm initial height

As mentioned at start, three different oils with various viscosities have been utilized during the investigative experiments. In the preceding section (4.1.1) the evolution of states With Spindle oil was presented. The second type of liquid that we will examine now hydraulic H-22 with kinematic viscosity of 46.8 cSt. The experiments were conducted for the same initial liquid levels 8, 10 and 12 mm. In general, the results were found to be comparable to those that were described in the previous section. Hence only the significant dissimilar outcomes will be presented here. The detailed spin-up and spin-down tables and the accompanied photographs of the equilibria can be found in Appendix A.

The first noticeable difference is the disk speed in which the first pattern appears. In the case of spindle oil with relatively lower viscosity, the equilibrium states appeared at lower speeds. For instance, the first equilibrium state for the spindle oil with the initial height of 8mm, appeared at 76.5 rpm, while for the H-22 oil with the same initial height, the first equilibrium state appeared at 172.4 rpm.

The second finding had to do with the maximum speed at which the coherent structures endured. In case of the Spindle Oil, the flow transferred to full blown turbulent states at approximately 188.4 rpm. However, for H-22 oil took place at 332.69 rpm. This suggests that the higher viscosity fluid causes the equilibria to remain stable and laminar over a wider range of disk speeds.

The third noteworthy difference pertains to the diversity of equilibrium states that were observed. On one hand a variety of patterns were detected utilizing the spindle oil as the working

fluid patterns with $N = 2, 3, 5, 6, 7, 8, 9, 10, 11, 12, 13, 14, 15, 17, 18$ and 19 were identified. On the other hand, with H-22 only equilibrium states of $N = 5, 6, 7, 8, 11, 12, 13$ and 15 were found. Also, it should be noted that, unwavering patterns were observed only in Spindle oil but not in H-22 and H-32. This will be discussed later. In addition, using H-22, a retrograde pentagonal equilibrium was unearthed. The last was absent in the Spindle oil experiments.

The fourth was related to two most significant phenomena, which have been exposed previously using Spindle Oil; the presence of solitary wave(s) and the wobbling effects. Neither solitary waves, nor equilibrium wobbling effects emerged through utilizing H-22 and H-32 oils.

And fifth disparity concerns the bifurcation phenomena, which took place more often for Spindle Oil than in H-22 and H-32 cases.

These were the most noticeable incongruities found in the experiments with different viscosity fluids.

Following, the schematic of typical N equilibria versus the disk speed for different heights are given in Figs. 24, 25 and 26. The three different figures are summarized in Fig. 26 as a three-dimensional state manifold as a function of N , Ta , and h_o / R_d . The sequences of the equilibria are given in Tables 7, 8, 9, 10, 11 and 12 of Appendix A.

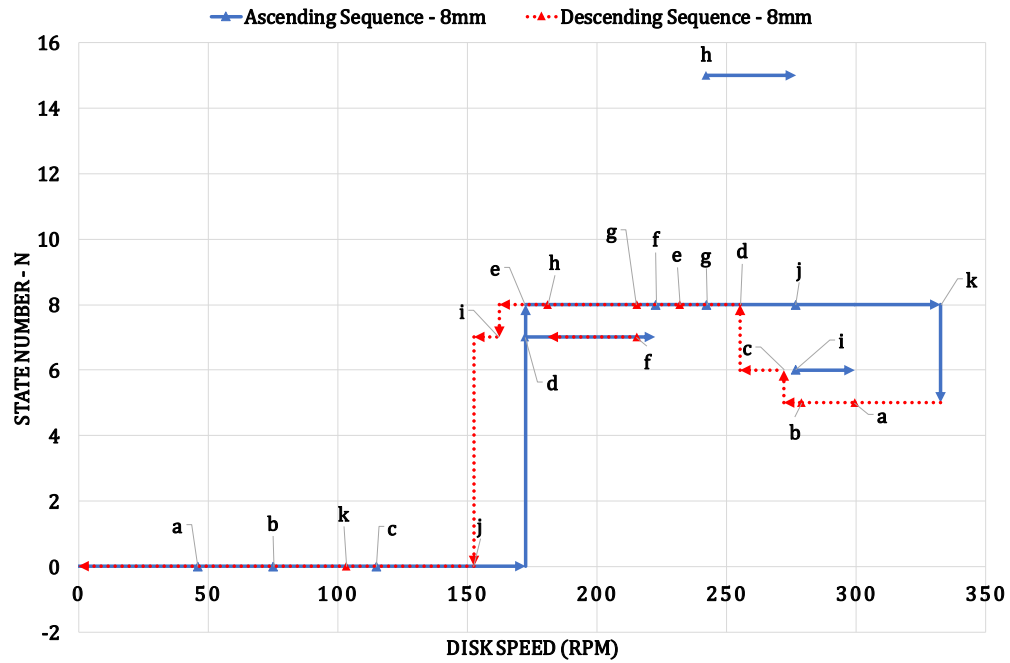


Figure 25. H-22 Oil (8mm) Schematic of Typical Equilibrium Spectrum

4.1.3.2 H-22 Hydraulic Oil 10 mm initial height

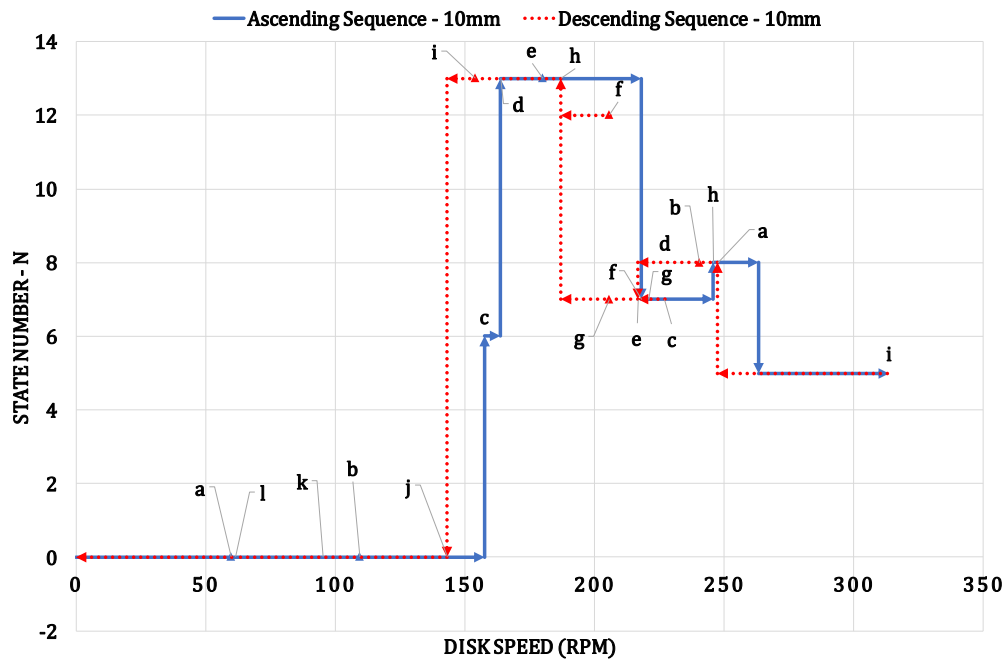


Figure 26. H-22 Oil (10mm) Schematic of Typical Equilibrium Spectrum

4.1.3.3 H-22 Hydraulic Oil 12 mm initial height

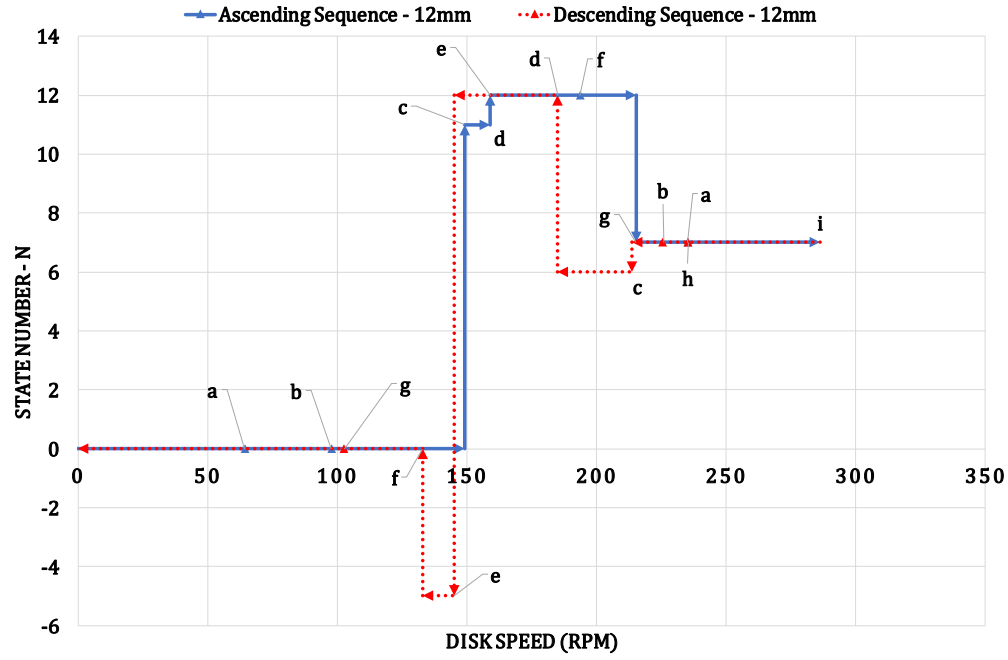


Figure 27. H-22 Oil (12mm) Schematic of Typical Equilibrium Spectrum

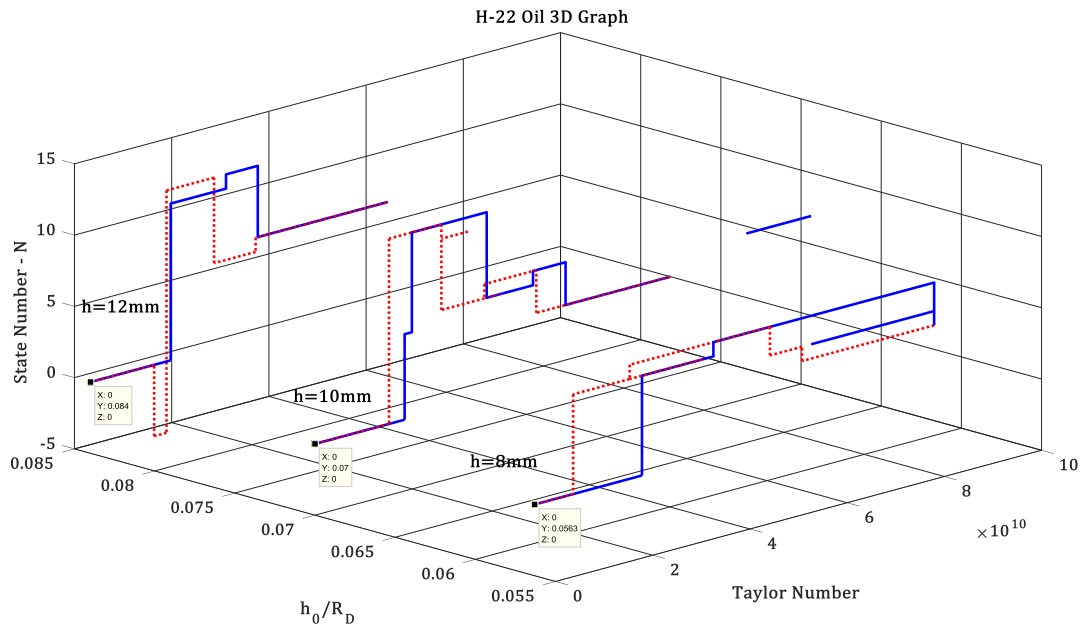


Figure 28. H-22 Oil 3D Graph Representing *Taylor's No.* versus N and $\frac{h_0}{R_d}$ ratio

4.1.4 H-32 Hydraulic Oil

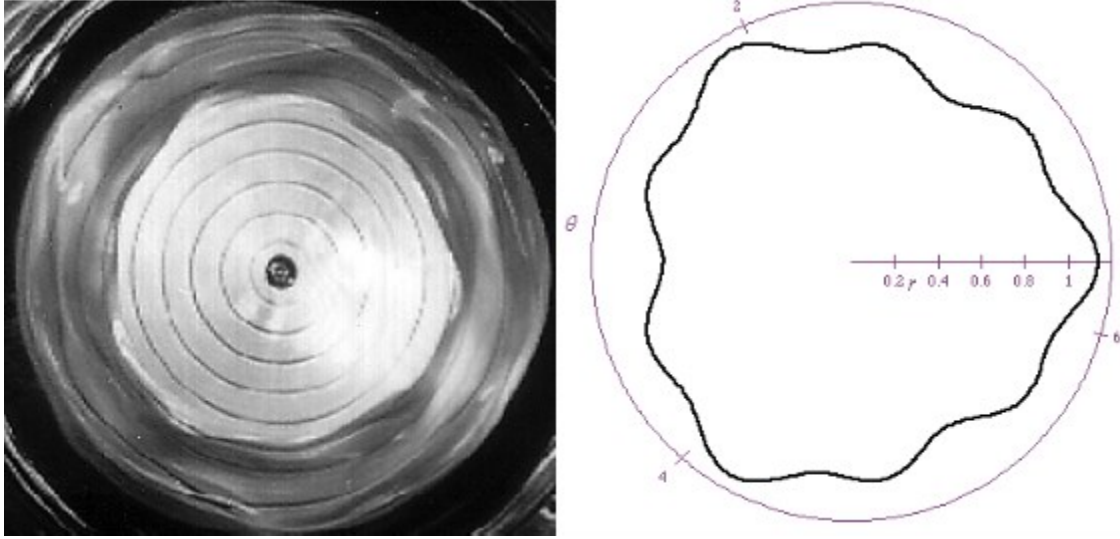
4.1.4.1 H-32 Hydraulic Oil 8 mm initial height

The last working fluid was H-32 hydraulic oil with kinematic viscosity of 64.75 cSt, which was the most viscous fluid in comparison to the other two i.e. Spindle oil and H-22 hydraulic oil. The entire ascending and descending sequences along with the initial fluid heights were the same as the other two fluids. However, there were several differences in flow manifestation that will be discussed below.

The first expected dissimilarity was the speed at which the patterns began to appear. For instance, starting from rest with initial height 8mm, the first equilibrium state for Spindle Oil (lowest viscosity) appeared at 76.5 rpm, for H-22 at 172.4 rpm, and finally for H-32 Oil with the (highest viscosity) emerged at 202.09 rpm.

The second noticeable difference was the fact that at higher speeds H-32 as flow was approaching the turbulent state, due to generation of air bubbles the oil was getting milky. This interference forced us to terminate the tests at lower speeds than in H-22. However, the final reachable speed was once more higher than that of Spindle oil.

As mentioned before, neither solitary waves, nor wobbling effect were observed here. Therefore, almost the entire set of phenomena associated with the problem was observed in Spindle oil. Instead, mixed states, which were the combination of two or more states at the same speed, were detected during the laboratory experiments, in both the H-22 and H-32 oils. In mixed states the amplitude of one pattern is harmonically modulated by one or more wave(s) with different frequency. A very clear case of mixed states was observed previously where an $N = 3$ state is harmonically modulated by another $N = 9$, see Fig. 28.



$$r_s = \{1 + 0.03 \cos(9\theta)\} \{1 + 0.05 \cos(3\theta)\}$$

Figure 29. Harmonic Modulation of the $N = 3$ state by an $N = 9$ wave in oil having a viscosity of 5.7 cSt (courtesy of G. H. Vatistas and J. Wang 1992).

The last significant variation involved the diversity of the patterns that have been observed. As mentioned earlier, there were more equilibrium states detected in Spindle oil than in both H-32 and H-22. Specifically, for the H-32, the assortment was even narrower than in the other two fluids.

Following, the schematics of typical equilibrium spectra given in Figs. 29, 30 and 31 along with the 3D state manifold graph shown in Fig. 31 providing a summarized picture of the occurrence. The sequences of the equilibria are given in Tables 13, 14, 15, 16, 17 and 18 of Appendix B.

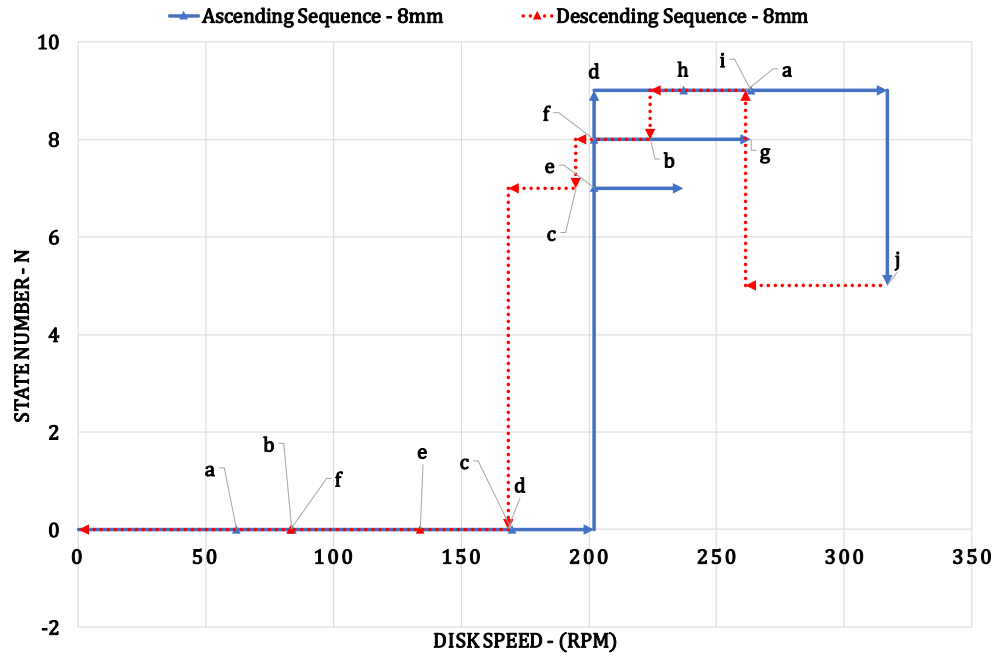


Figure 30. H-32 Oil (8mm) Schematic of Typical Equilibrium Spectrum

4.1.4.2 H-32 Hydraulic Oil 10 mm initial height

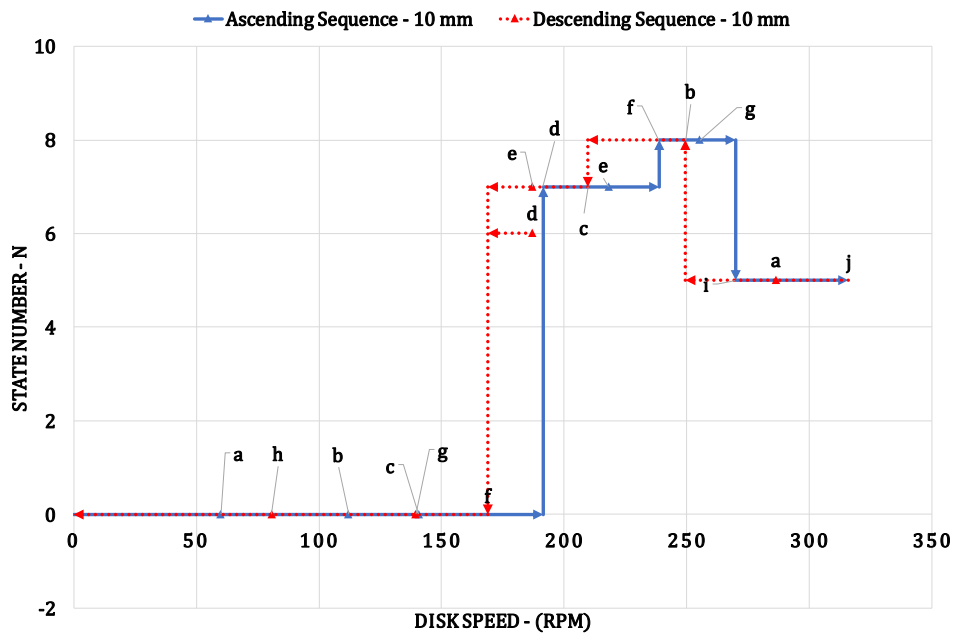


Figure 31. H-32 Oil (10mm) Schematic of Typical Equilibrium Spectrum

4.1.4.3 H-32 Hydraulic Oil 12 mm initial height

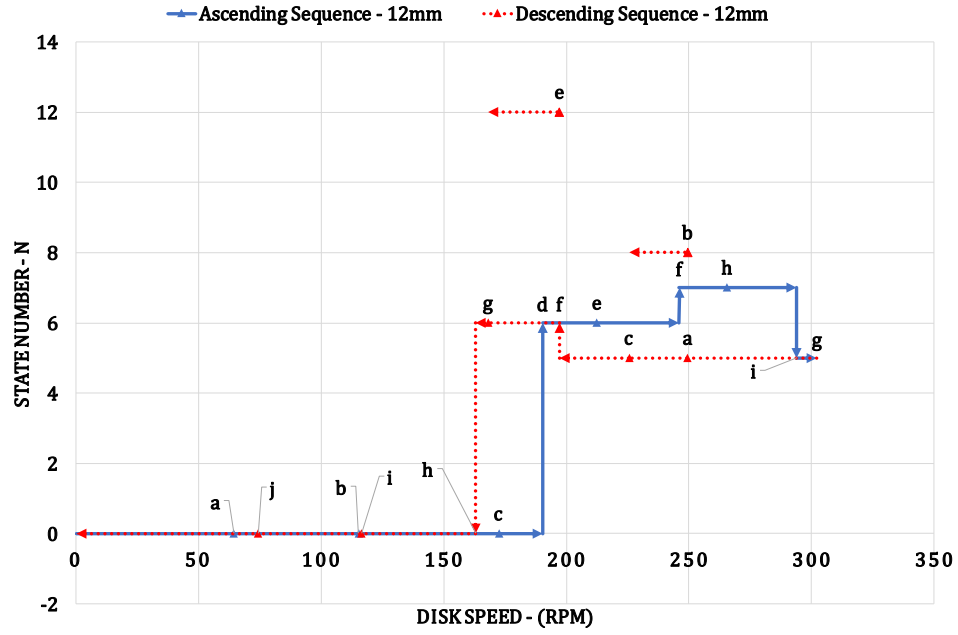


Figure 32. H-32 Oil (12mm) Schematic of Typical Equilibrium Spectrum

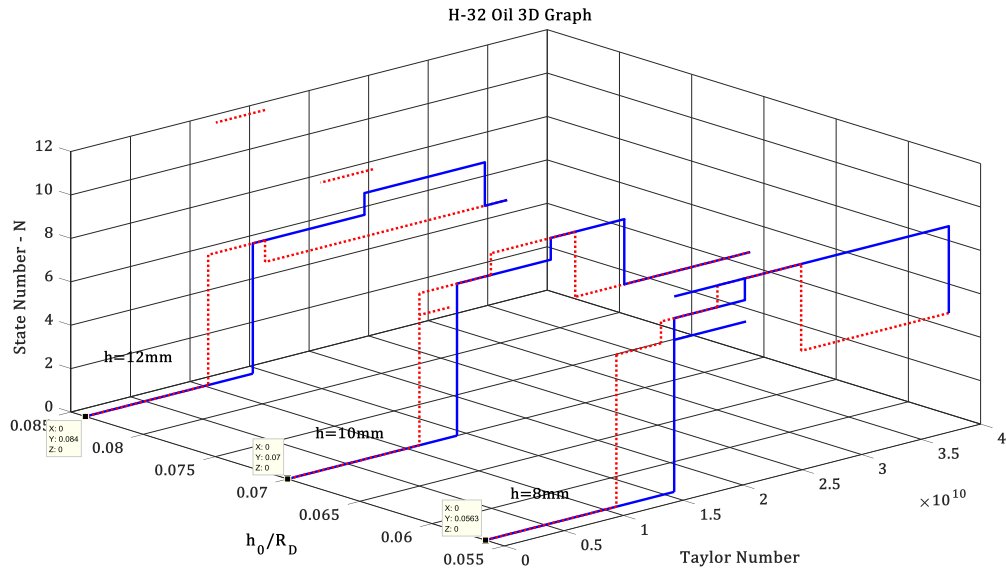


Figure 33. H-32 Oil 3D Graph Representing *Taylor's No.* versus N and $\frac{h_0}{R_d}$ ratio

4.2 Image Processing Through MATLAB

A high-speed camera was used to capture the sets of images of different patterns. A typical image captured during the experiments is demonstrated below (Fig. 33).

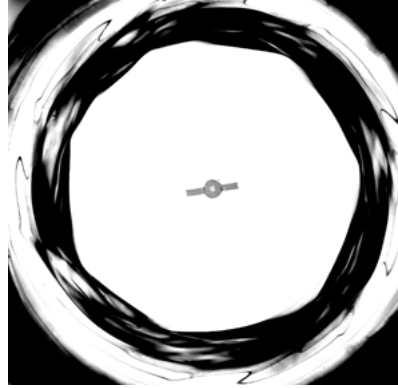


Figure 34. Typical Image of Experiments

An image-processing algorithm implemented in the MATLAB platform (Appendix E) was developed to identify the corners of the polygonal patterns. Utilizing the algorithm, each set of images acquired by the high-speed camera was processed automatically and the contours of patterns were produced. Below, the details of the algorithm are illustrated step by step.

The first step was to use an appropriate filter in order to reduce noise (called effects and sharpness of the image) and to increase its capacity for further processing, which in this case is to convert the gray scale image (Fig. 34 (a)) into a binary image. A low-pass Gaussian filter was applied during this algorithm as shown in Fig. 34 (b).

The second step concerns the image segmentation, which defines as the conversion of the primary 8-bit gray-scale image into a binary image, using an adequate limen to extract the different polygonal shape pattern's contour. Consequently, choosing the appropriate threshold is

critical for this step. The quantity of the limen for image segmentation was chosen based on sharpness of the edges of polygonal shapes for each series of images and was applied to all images in the specific set. In this step, all the pixels with gray-scale quantities more than or equal to the limen were assigned 1's and the pixels with gray-scale values lower than the limen such as dark portions, were assigned 0's. Therefore, by applying this, the binary image illustrated in Fig. 34 (c), was created for each image.

Next, the intended regions, i.e. the boundaries of the pattern, were extracted from the binary image. Accordingly, the standard edge detection procedure was executed. The contours gained from the edge recognition sequence were then filtered using a zero-phase filter to affirm that they had no phase distortion (Fig. 34 (d)). Superposition of the contours demonstrated that each image had its own contour, which due to disk rotation and consequently pattern's rotation, would vary from the previous contour, and the edges had been moved during time (Fig. 34 (e)).

It should be included that prior to the experiments, two small white color strips were marked on the disk, which are clearly observable in each image. The mentioned strips were used to determine the disk's rotational velocity through image analysis.

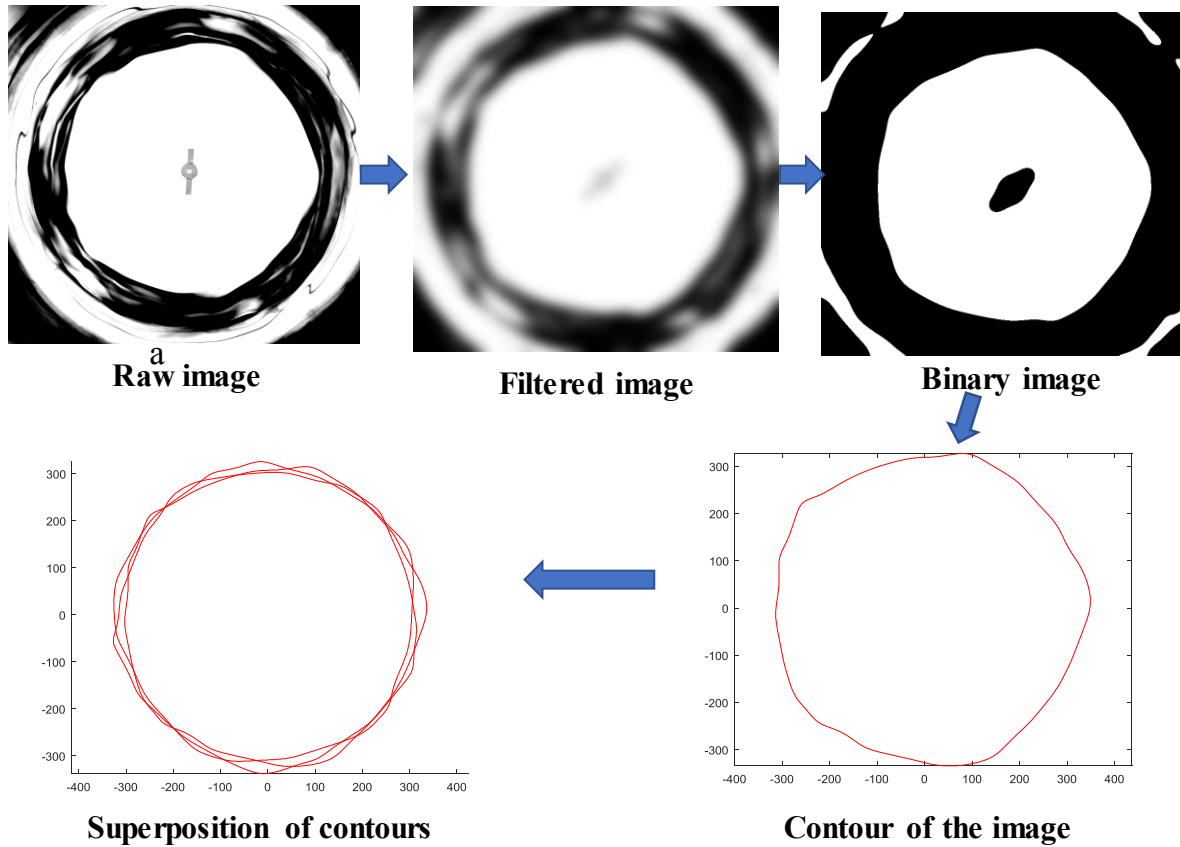


Figure 35. Image Processing Procedure

4.3 Analysis

The second part of the MATLAB code was used to analyze the data generated by the image-processing algorithm. Based on each image, a contour was created, and using the superposition and signature function, a series of variable radial distances from the center of the image was embodied. In order to make it clearer, a sample of image of say a heptagon along with its corresponding contour and a series of distances (in terms of signals) were determined, see Fig. 35.

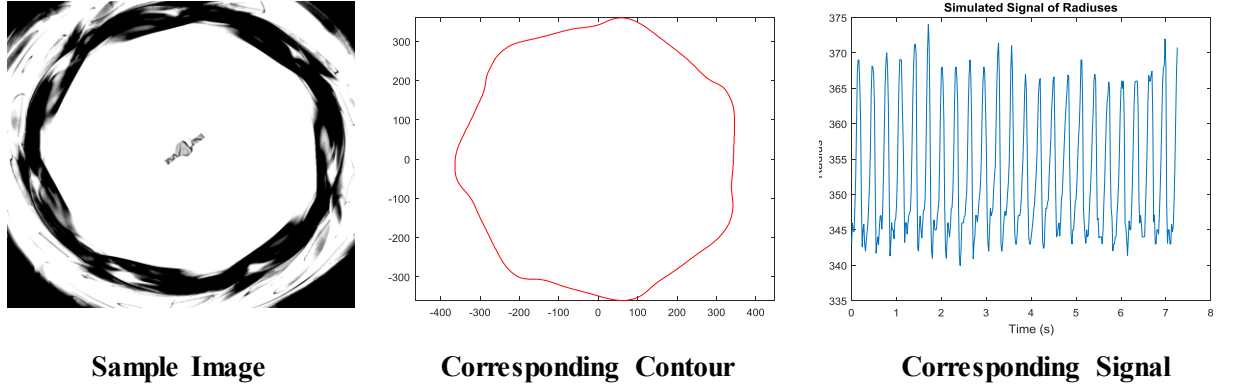


Figure 36. Signal Analysis

The interest here was to obtain the frequency of the pattern using the obtained signals. Utilizing the Fast Fourier Transformation (FFT) function, the dominant frequency was calculated based on the power spectrum outcome shown in Fig. 36. (a) The leading frequency⁶ must be divided by the number of edges in the equilibrium state.

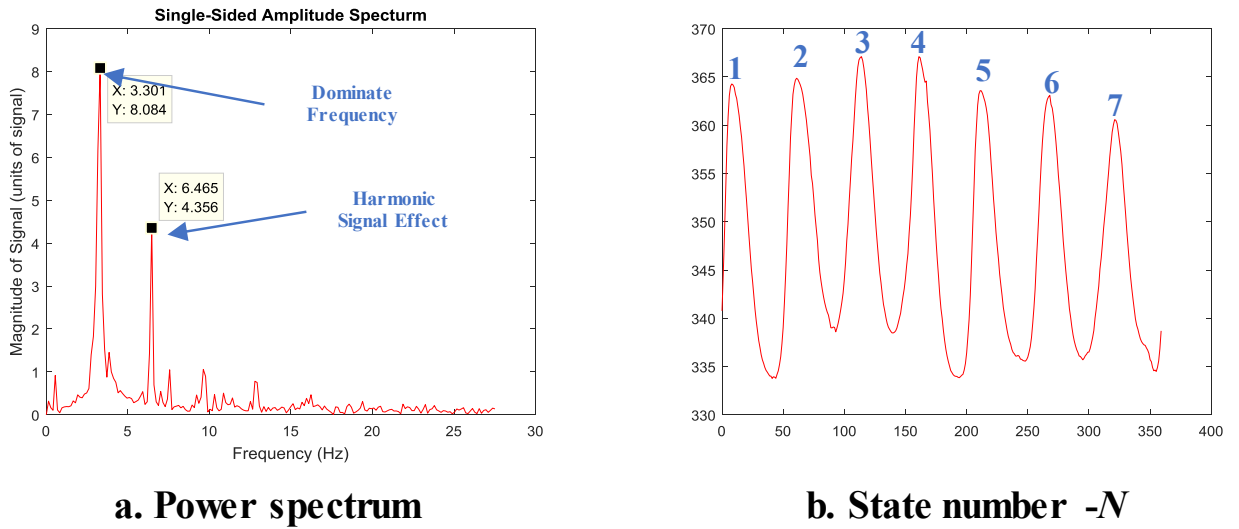


Figure 37. (a) Fast Fourier Transform. (b) State Number

⁶ The main frequency should be divided by the state number since every corner of the polygon passes through the fixed-point N times.

In this case, the principle frequency was 3.301 Hz that needs to be divided by the state number $N = 7$. To obtain the exact state number, the sample contour, shown in Fig. 36 (b), could clarify the method. Each peak represents one edge, since there are seven peaks, then the equilibrium must be a heptagon. Therefore, its frequency is:

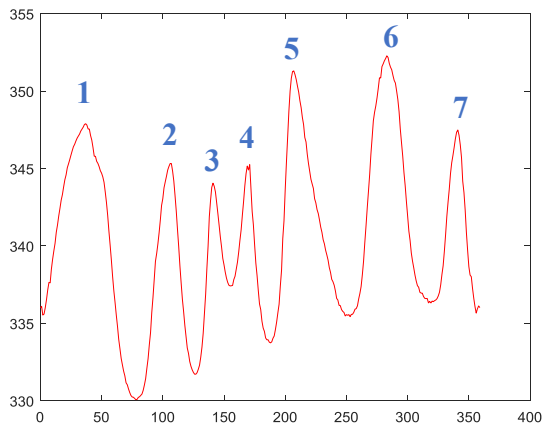
$$\frac{3.301}{7} = 0.47 \text{ Hz}$$

But as mentioned earlier, there are some exceptional cases, which were discussed, and their corresponding power spectrum will be stated. Though, most of the images were clear and behave like the others in terms of power spectrum and signals, some specific cases were different.

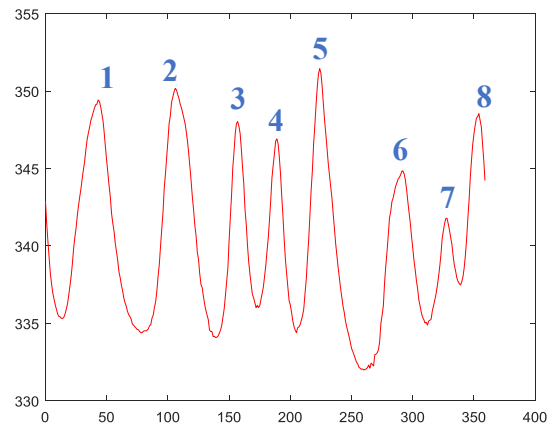
In case of stationary pattern, power spectrum and signals graph were not applicable since there was not any significant movement. On the other hand, mixed states were more complicated since two or more patterns existed at same time. In this case however, power spectrum and signals were still applicable as follows (Fig. 37):



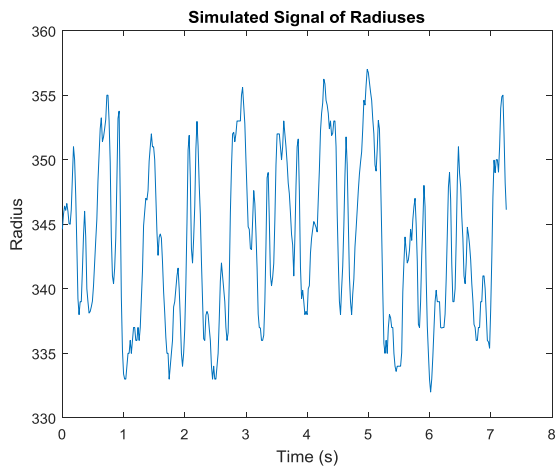
Sample Image



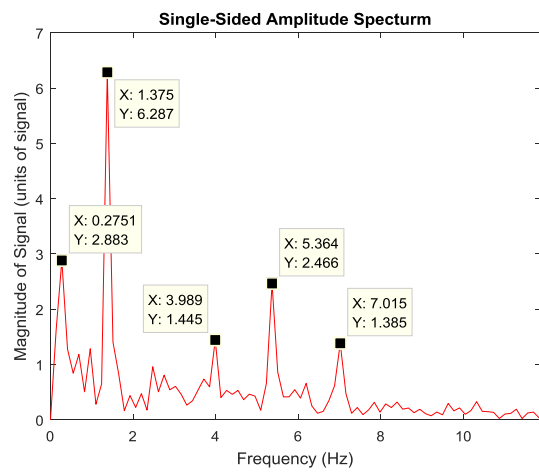
State Number -7



State Number -8



Corresponding Signal



Power Spectrum

Figure 38. Mixed States Representation

Hence, due to lack of a pure equilibrium state was not present no single pattern frequency

was present.

Another case was a state with solitary wave(s) encircling its contour. Note that the secondary peaks in the power spectrum do not necessarily lead to secondary waves modulating the base pattern (Fig. 38), because several of them are harmonics of the main frequency. The figures shown below could make clearer the above-mentioned arguments.

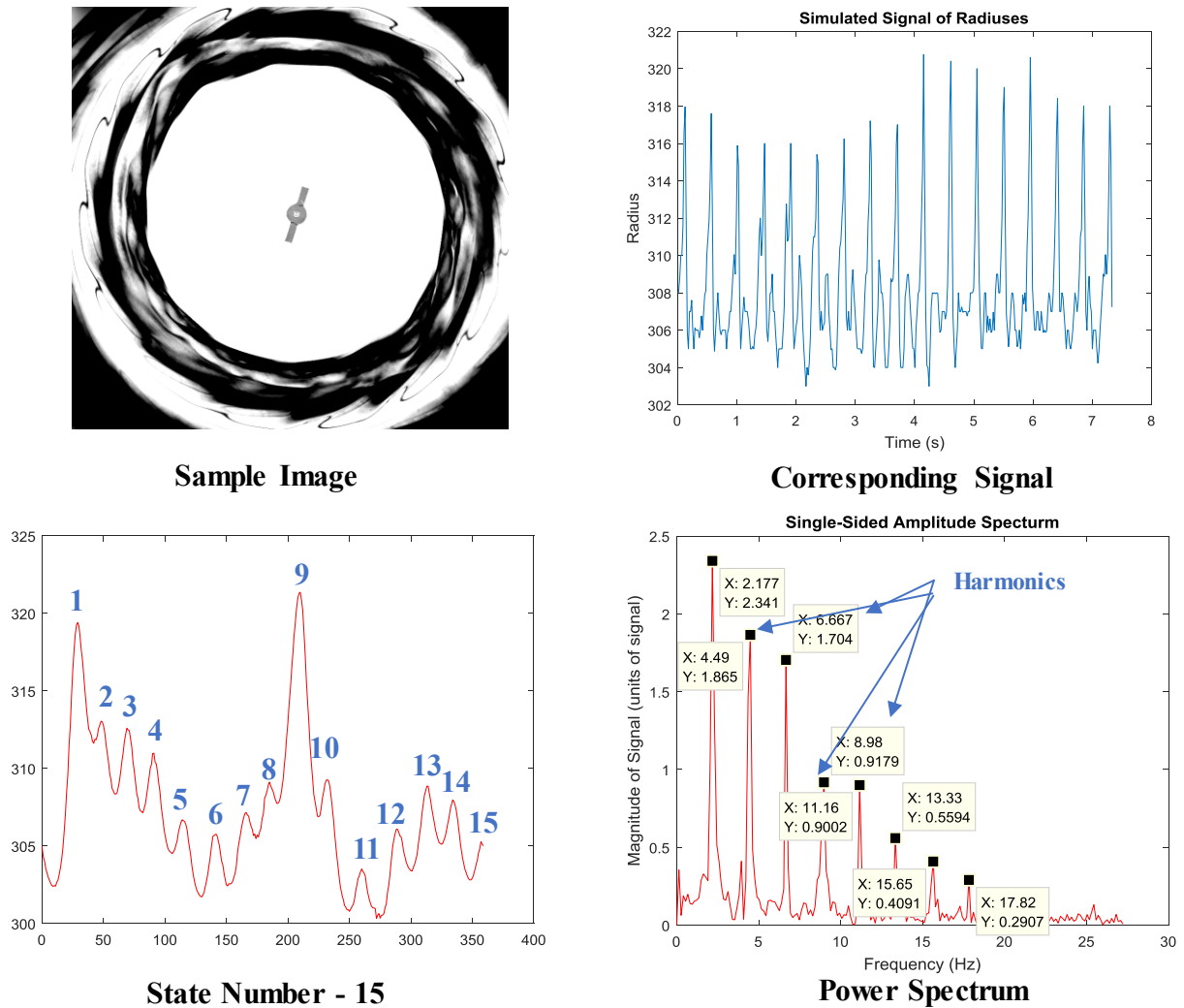


Figure 39. Pattern interrupted with solitary waves

Variety of patterns including their corresponding signal and power spectra are provided

in Appendix C.

4.4 Results

Based on the gathered data from image processing, the corresponding signals, and the FFT power spectra, the following dimensionless number could be considered:

- *Reynolds Number* ($Re = \frac{vR}{\nu}$, v = Disk Velocity in $\frac{m}{s}$, R = Disk radius, ν = Kinematic Viscosity in $\frac{m^2}{s}$),
- *Froude Number* ($Fr = \frac{v}{\sqrt{gh}}$, v = Disk Velocity in $\frac{m}{s}$, $g = 9.81 \frac{m}{s^2}$, h = initial height in m),
- *Taylor Number* ($Ta = \frac{4\omega_d^2 R^4}{\nu^2}$, ω_d = Disk Velocity in rpm , R = Disk radius in m , ν = Kinematic Viscosity in $\frac{m^2}{s}$),
- *C ratio (celerity)* defined as the ratio of pattern speed ω_p to disk speed ω_d ($\frac{\omega_p}{\omega_d}$)

The Reynolds number is the ratio of inertial to viscous forces, the Froude number defined as the ratio of the flow inertia to gravitational forces, and finally Taylor's number, which defines the ratio of centrifugal forces to viscous forces. Parameter C represents the ratio of the wave celerity to rotational speed of the disk. It should be noted that the C only applies to cases where the pattern is clear and predictable.

By calculating all of the abovementioned dimensionless quantities for each set of experiments, figures of discrete data were produced. These are provided in Appendix D.

The superposition of Taylor Number, Froude Number and Reynolds Number are given in the Appendix E.

The superimposed figure of all the experimental outcomes in terms of C versus Taylor's

number are provided in Fig. 39:

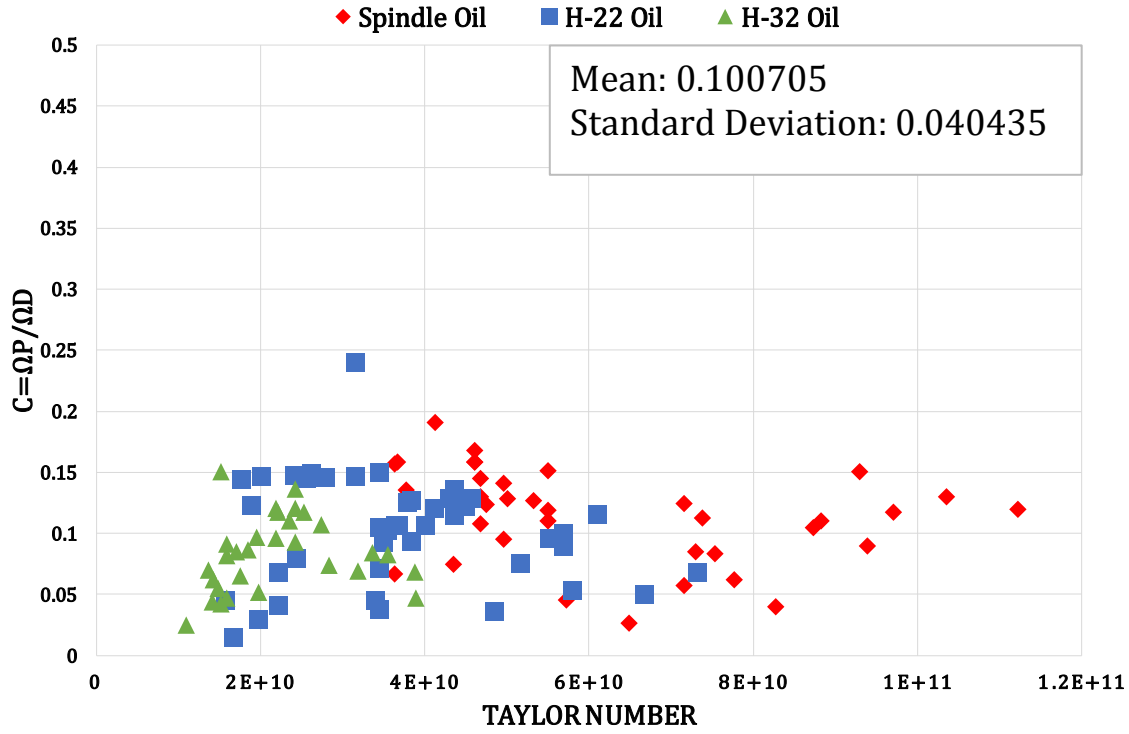


Figure 40. Superimposed Figure Representing C ratio versus *Taylor's Number*

It was uncovered here that the pattern frequency lock-in is about 1/10 of the disk's speed while for water was found earlier by Ait-Abderrahmane (2008) to be 1/3. The previous result using oil was obtained using 110 points in with three different viscosity fluids and 3 initial heights. The standard deviation of the dataset was calculated to be 0.04 (see Fig. 40) having an ensemble average of 0.1. The coefficient of variation ($CV = \text{standard deviation} / \text{mean value of the population}$, see Banik et al. (2012)) is often used in various scientific disciplines to determine the dispersion of the data in relation to its mean and standard deviation values. The calculated coefficient of variation in our case was found to be 0.40, which is less than one (note that CV could be more than 1). Therefore, the value for frequency lock-in of 1/10 is an acceptable result.

Analogous results with water by Vatistas and Ait-Abderrahman (2017) yielded a standard deviation of 0.015 with an ensemble average for C equal to 0.33 giving a coefficient of variation of 0.03. However, by comparison the amplitudes of the oil equilibria were very small, and the patterns were twisted and thus less defined.

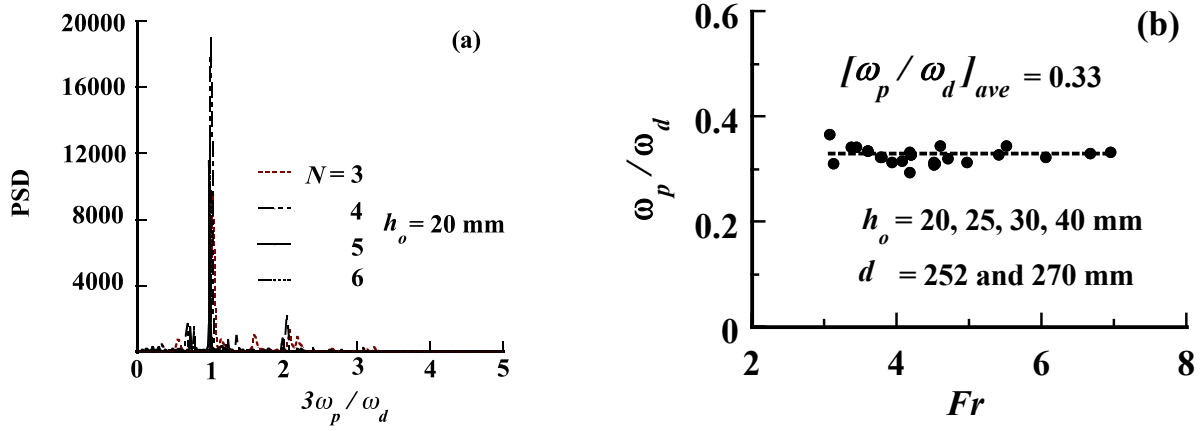


Figure 41. (a) Power Spectrum Density (PSD) of patterns from 3 to 6 modes, showing a pattern frequency lock-in at about 1/3 of the disk. (b) Frequency ratio vs. the Froude number. The average value of the set is 0.33 having a standard deviation of 0.01

5 Conclusions

This thesis communicated the findings of exploratory tests on oil vortices produced inside a cylindrical tank with a rotating base. The results of three different oils with different viscosities, performed under relatively shallow conditions with three liquid heights were presented. It was shown that the topology of equilibrium states that emerged show a considerably richer morphology than that of water. During a quasi-static spin-up and spin-down of the flow states ranging from $N = 2$ to 19 were found. Also pulsating ($N = 0$) and wobbling ($N = 1$) modes were spotted. In the case of H-22 a retrograde pentagonal ($N = 5$) equilibrium state within a specific interval of disk speed was also found. Both the spin-up and spin-down processes were associated with strong hysteresis whereby in some intervals flow bifurcations existed. These were more prominent in Spindle Oil than in H-22 and H-32. In the case of Spindle oil, the equilibria appeared at lower speeds than in H-22 and H-32.

A procession of one or groups up to 6 solidary waves arranged symmetrically on the apexes of regular polygons, moving at higher speeds than the host equilibrium state were apparent. Finally, patterns lock-in was found to occur at a frequency of about one-tenth the frequency of the rotating disk.

6 Future work

The present experiments have identified several issues that could be addressed by others that wish to make contribution with the aim to advance knowledge on the same topic.

The most important of them rests on the fact that the viscosities used here produced waves with very small wave amplitudes giving rise to low resolution. In future tests on liquids with lower kinematic viscosity (in the lower range of $10^{-5} m^2/s$) should be considered.

The state manifold constructed herein was sparsely populated and as such did not reveal the expected folds that will give rise to the now identified bifurcated states. Future tests should include more initial liquid heights, and refined disk speed increments. Also, considering discs of different sizes can enlarge the range of the dominant dimensionless numbers.

Theoretical treatment to this phenomena and interpretation of the results in that respect would make a significant future work and value to this research.

7 References

- Ait-Abderrahmane, H. (2008) “Two Cases of Symmetry Breaking of Free Surface Flows,” *Ph.D. Thesis*, Mechanical Engineering Department, Concordia University, Montreal, Canada.
- Ait-Abderrahmane, H. A., Kamran Siddiqui, M. H. & Vatistas, G. H. (2009) “Transition between Kelvin’s equilibria,” *Phys. Rev. E* **80**, 066305.
- Ait-Abderrahmane, H., Fayed, M., Ng, H. D., and Vatistas G. H. (2013) “A note on relative equilibria in a rotating shallow water layer,” *J. Fluid. Mech.* **724**, pp. 695-703.
- Amaouche, M., Ait-Abderrahmane, H., and Vatistas, G. H. (2013) “Rotating solitary wave at the wall of a cylindrical container.” *Physical Review*, **87** 043015 (2013).
- Banik, S., Kibria G. B. M., and Sharma, D. (2012) “Testing the Population Coefficient of Variation,” *Journal of Modern Applied Statistical Methods*, **11** (2), pp. 325-335.
- Barbosa Aguiar, A. C., Read, P. L., Wordsworth, R. D., Salter, T., and Yamazaki, Y. H. (2010) “A laboratory model of Saturn’s north polar hexagon,” *Icarus*, **206**, pp. 755– 763.
- Bedard, A. J. (2005) “Low-Frequency Atmospheric Acoustic Energy Associated with Vortices Produced by Thunderstorms,” *Mon. Weather Rev.* **133**, pp. 241-263.
- Beckwith T. G., Marangoni R. D., Lienhard V J. H., (2007) “Mechanical Measurements,” sixth edition. *Prentice Hall*.
- Braun, S. A., Montgomery, M. T. and Pu, Z. (2006) “High- resolution simulation of Hurricane Bonnie (1998). Part I: The organization of eyewall vertical motion,” *J. Atmos. Sci.*, **63**, pp. 19-42.

- Cabral, H. E. and Schmidt, D. S. (1999) "Stability of relative equilibria in the problem of $N+1$ vortices," *SIAM J. Math. Anal.* **31**, pp. 231-250.
- Carnevale, G. F. and Kloosterziel, R. C. (1995) "Emergence and evolution of triangular vortices," *J. Fluid Mech.* **259**, pp. 305-331.
- Chakraborty, P., Gioia, G. and Kieffer, S. W. (1999) "Volcanic mesocyclones," *Nature*, **458**, 07866.
- Durkin, D. and Fajans, J. (2000) "Experiments on two-dimensional vortex patterns," *Phys. Fluids* **12**, pp. 289-293.
- Einstein, A. (1905) "On the Electrodynamics of Moving Bodies," *Annalen der Physik*, **17**, pp. 891-921
- Fridman A. M., Morozov A. G., Nezlin M. V., and Snezhkin E. N. (1985) "Centrifugal instability in rotating shallow water and the problem of the spiral structure in galaxies," *Physics Letters*, **109A** (5), 228-231.
- Fujita, T. T., Watanabe K., Tsuchiya K. and Shimada, M. (1972) "Typhoon-associated tornadoes in Japan and new evidence of suction vortices in a tornado near Tokyo," *J. Meteor. Soc. Japan*, **50**, pp. 431- 453.
- Godfrey, A. D. (1988) "A hexagonal feature around Saturn's North Pole," *Icarus*, **76** (2), pp. 335-356.

Gonzales, R.C and Wood, R.E. (2004) “Digital image processing using MATLAB,” seventh edition. *Prentice Hall*.

Görtler, H. (1955). “Dreidimensionales zur Stabilitätstheorie laminarer Grenzschichten,” *Journal of Applied Mathematics and Mechanics*. **35** (9–10), pp. 362–363.

Gregory, N., Stuart J. T. and Walker, W. S. (1955) “On the stability of three-dimensional boundary layers with application to the flow due to a rotating disk,” *Phil. Trans. Roy. Soc. London Ser. A* **248**, pp. 155 – 199.

Havelock, T. H. (1931) “The stability of motion of rectilinear vortices in ring formation,” *Philos. Mag.*, **11**(7), pp. 617-633.

Jansson, T. R. N., Haspang, M. P., Jensen, K. H., Hersen, P. and Bohr, T. (2006) “Polygons on a Rotating Fluid Surface,” *Phys. Rev. Lett.* **96**, 174502.

Kurakin, L. G. and Yudovich, V. I. (2002) “The stability of stationary rotation of a regular vortex polygon,” *Chaos* **12**, pp. 574-595.

Lewis, B. M. and Hawkins H. F. (1982) “Polygonal eye walls and rain bands in hurricanes,” *Bull. Amer. Meteor. Soc.*, **63**, pp. 1294-1300.

Michelson, A.A. and Morley, E.W. (1887) “On the Relative Motion of the Earth and the Luminiferous Ether,” *Am. J. Sci.*, **34**, pp. 333 – 345.

Morales-Juberías R., Sayanagi, K. M., Dowling, T. E. and Ingersoll, A. P. (2011) “Emergence of polar-jet polygons from jet instabilities in a Saturn model,” *Icarus* **211**, pp. 1284–1293.

Polvani, L. M and Dritschel, D. G. (1993) “Wave and vortex dynamics on the surface of a sphere,” *J. Fluid Mech.* **255**, pp. 35-64.

Russell, J.S. (1844) “Report on waves,” Rep. 14th Meet. British. Assoc. Adv. Sci. in Proc. **3** pp. 11-390.

Schubert, W. H., Montgomery, M. T., Taft, R. K. , Guinn, T. A. , Fulton,, S. R. , Kossin, J. P., and Edwards, J. P. (1999) “Polygonal Eyewalls, Asymmetric Eye Contraction, and Potential Vorticity Mixing in Hurricanes,” *J. Atmos. Sci.*, **56**, pp. 1197-1223.

Stewart, H. (1943) “Periodic properties of the semi-permanent atmospheric pressure systems,” *Quart. Appl. Math.* **1**, pp. 262-267.

Sawatzki, O. and Zierep, J. (1970) “Das Stromfeld im Spalt zwischen zwei konzentrischen Kugelfl/ichen, von denen die inhere rotiert.” *Acta Mech.* **9**, pp. 13-15.

Taylor, F. W. (2006) “Venus before Venus Express,” *Planetary and Space Science*, **54**(13-14), pp. 1249-1262.

Thomson, W. (1875-6) “Vortex statics,” *Mathematical and Physical Papers*. Cambridge, **IV**, p. 10.

Thomson, W. (1869) “On vortex atoms,” *Proceedings of the Royal Society of Edinburgh*, **6**, pp. 94–105.

Thomson, W (1878) “Floating Magnets,” *Nature* **18**, pp. 13-14.

Thomson, W. (1880) “Vibrations of a Vortex Column,” *Phil. Mag.* **10**, 155–168.

Thomson, J. J. (1883) “Treatise on Vortex Rings,” *Macmillan*, London p. 94.

Vatistas, G. H. (1990) “A note on liquid vortex sloshing and Kelvin’s equilibria,” *J. Fluid Mech.* **217**, pp. 241-248.

Vatistas, G. H. and Ait-Abderrahman, H. (2017) “Beyond Kelvin’s atomic theory,” unpublished work.

Vatistas, G. H., Wang J. and Lin S. (1992) “Experiments on waves induced in the hollow core of vortices,” *Experiments in Fluids* **13**, pp. 377-385.

Vatistas, G.H., Esmail, N. and Ravanis, C. (2001) “Wave development in disk-like Nearly inviscid liquid vortices” *39th AIAA Aerospace Sciences Meeting and Exhibit*. Paper no. AIAA 2001-0168, 8-11 January 2001, Reno, NV.

Vatistas G. H. and Ait-Abderrahmane, H. (2012). Beyond Kelvin’s atomic theory. *Unpublished Work*.

Von Helmholtz, H. (1858) “Über Integrale der hydrodynamischen Gleichungen welche den Wirbelbewegungen entsprechen,” *Journal für die reine und angewandte Mathematik* **55 pp.** 25-55.

Wang, J. (1995) “On the wave activity within vortex cores,” *Ph.D. Thesis*, Mechanical Engineering Department, Concordia University, Montreal, Canada.

Williams, G. A. and Packard, R. E. (1974) “Photographs of Quantized Vortex Lines in Rotating He II,” *Phys. Rev. Lett.* **33**, pp. 280–283.

Yarmchuk, E. J., Gordon, M. J. V. and Packard R. E. (1979) “Observation of stationary vortex arrays in rotating superfluid helium,” *Phys. Rev. Lett.* **43**, 214.

Appendix A

Table 7. H-22 Oil – 8mm Ascending Sequence Equilibria

| Disk Velocity (rpm) | Equilibria State (<i>N</i>) | Bifurcation | Figure (41) |
|---------------------|-------------------------------|-------------|-------------|
| 46.07 | Circle | NO | a |
| 75.05 | Circle | NO | b |
| 114.73 | Circle | NO | c |
| 172.44 | 7+ | YES | d |
| 172.44 | 8+ | YES | e |
| 222.54 | 8+ | NO | f |
| 242.18 | 8+ | YES | g |
| 242.18 | 15+ | YES | h |
| 276.78 | 6+ | YES | i |
| 276.78 | 8+ | YES | j |
| 332.69 | Mixed 5+ and 6+ | NO | k |

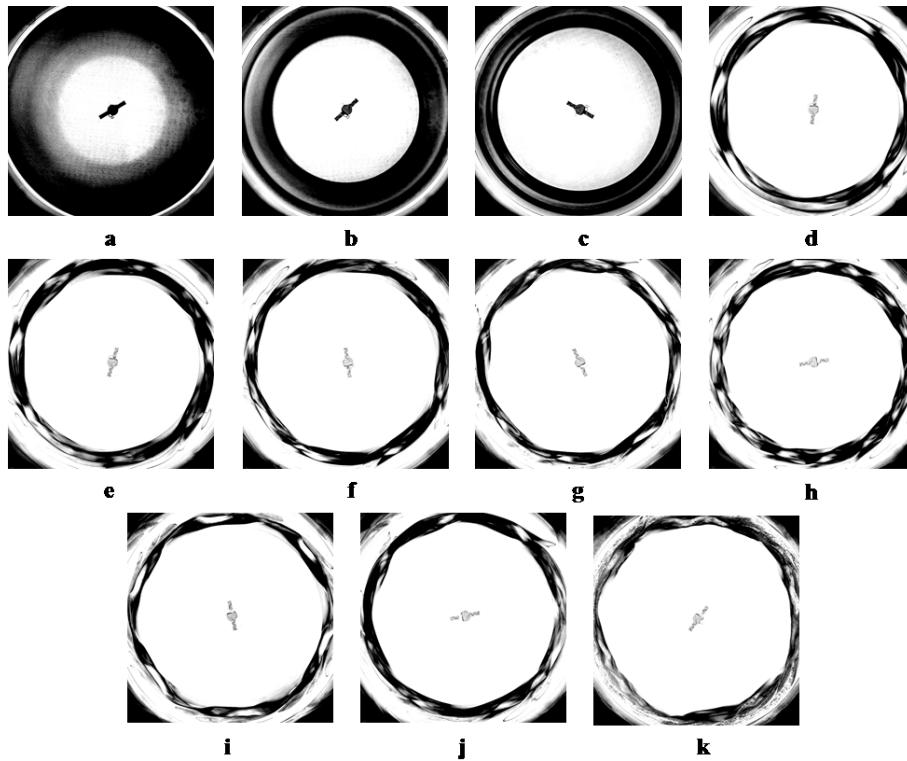


Figure 42. H-22 Oil (8mm) Ascending Sequence Actual Equilibria

Table 8. H-22 Oil – 8mm Descending Sequence Equilibria

| Disk Velocity (rpm) | Equilibria State (<i>N</i>) | Bifurcation | Figure (42) |
|------------------------|----------------------------------|-------------|----------------|
| 299.42 | 5+ | NO | a |
| 279.12 | 5+ | NO | b |
| 272. 2 | 6+ | NO | c |
| 255.32 | 8+ | NO | d |
| 231.95 | 8+ | NO | e |
| 215.27 | 7+ | YES | f |
| 215.27 | 8+ | YES | g |
| 180.97 | 8+ | NO | h |
| 162.25 | 7+ | NO | i |
| 152.48 | Circle | NO | j |
| 103.25 | Circle | NO | k |

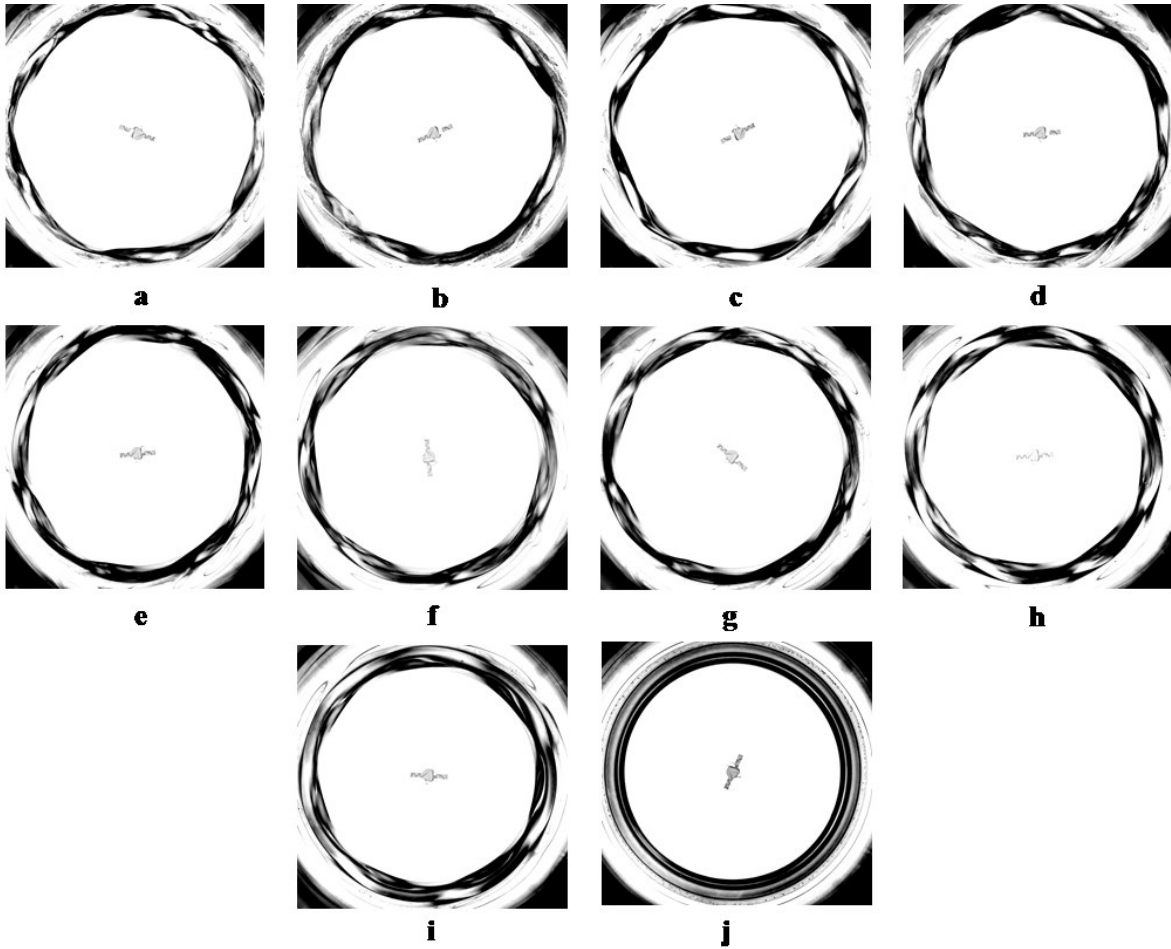


Figure 43. H-22 Oil (8mm) Descending Sequence Actual Equilibria

Table 9. H-22 Oil – 10mm Ascending Sequence Equilibria

| Disk Velocity (rpm) | Equilibria State (<i>N</i>) | Bifurcation | Figure (43) |
|------------------------|----------------------------------|-------------|----------------|
| 59.88 | Circle | NO | a |
| 109.42 | Circle | NO | b |
| 157.59 | 6(S) | NO | c |
| 163.86 | 13+ | NO | d |
| 179.98 | 13+ | NO | e |
| 218.12 | 7+ | NO | f |
| 221.05 | 7+ | NO | g |
| 245.79 | 8+ | NO | h |
| 263.49 | 5+ | NO | j |
| 313.68 | 5+ | NO | k |

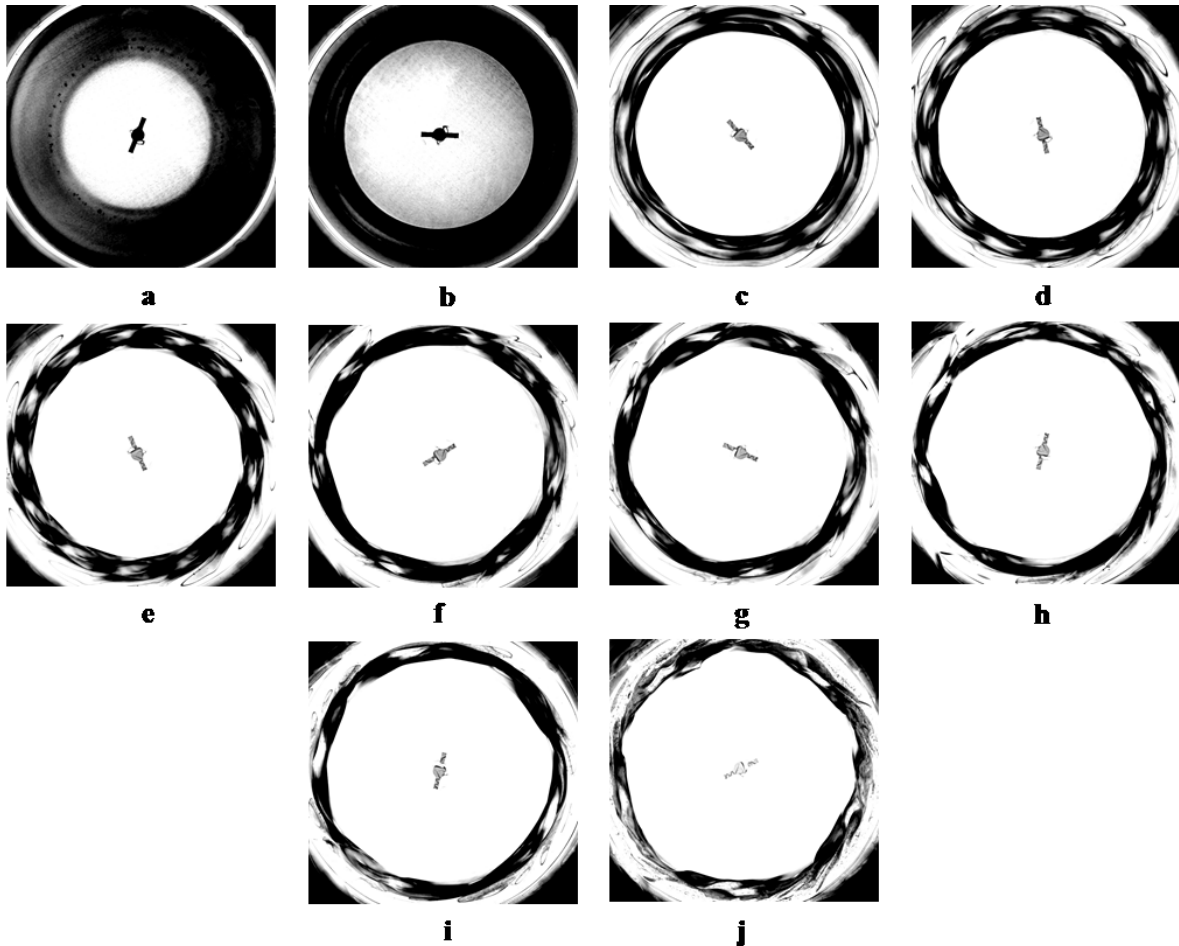


Figure 44. H-22 Oil (10mm) Ascending Sequence Actual Equilibria

Table 10. H-22 Oil – 10mm Descending Sequence Equilibria

| Disk Velocity (rpm) | Equilibria State (N) | Bifurcation | Figure (44) |
|---------------------|--------------------------|-------------|-------------|
| 247.64 | 8+ | NO | a |
| 240.41 | 8+ | NO | b |
| 227.15 | 7+ | YES | c |
| 227.15 | 8+ | YES | d |
| 216.7 | 7+ | NO | e |
| 205.85 | 12+ | YES | f |
| 205.85 | 7+ | YES | g |
| 187.14 | 13+ | NO | h |
| 153.91 | 13+ | NO | i |
| 143.2 | Circle | NO | j |
| 95.46 | Circle | NO | k |
| 61.56 | Circle | NO | l |

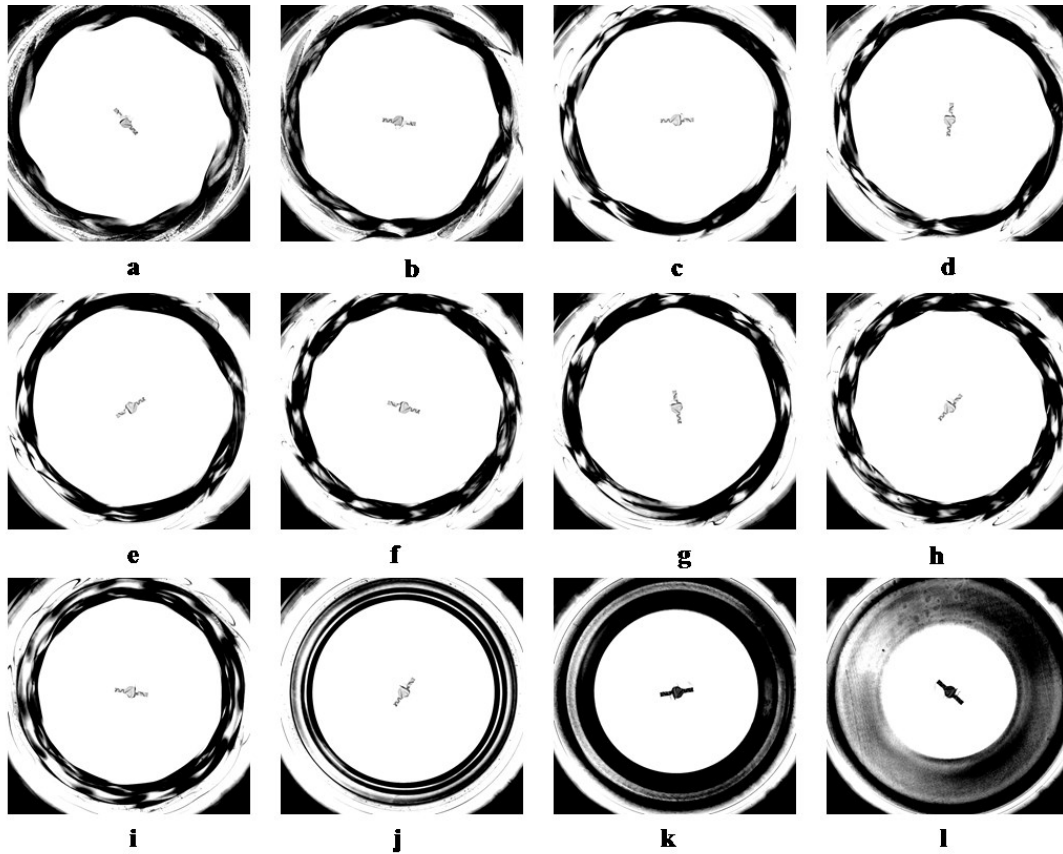


Figure 45. H-22 Oil (10mm) Descending Sequence Actual Equilibria

Table 11. H-22 Oil – 12mm Ascending Sequence Equilibria

| Disk Velocity (rpm) | Equilibria State (<i>N</i>) | Bifurcation | Figure (45) |
|------------------------|----------------------------------|-------------|----------------|
| 64.33 | Circle | NO | a |
| 97.73 | Circle | NO | b |
| 149.03 | 11+ | NO | c |
| 159.11 | 11+ | NO | d |
| 193.74 | 12+ | NO | e |
| 215.27 | 12+ | YES | f |
| 215.27 | 7+ | YES | g |
| 235.26 | 7+ | NO | h |
| 286.4 | 7+ | NO | i |

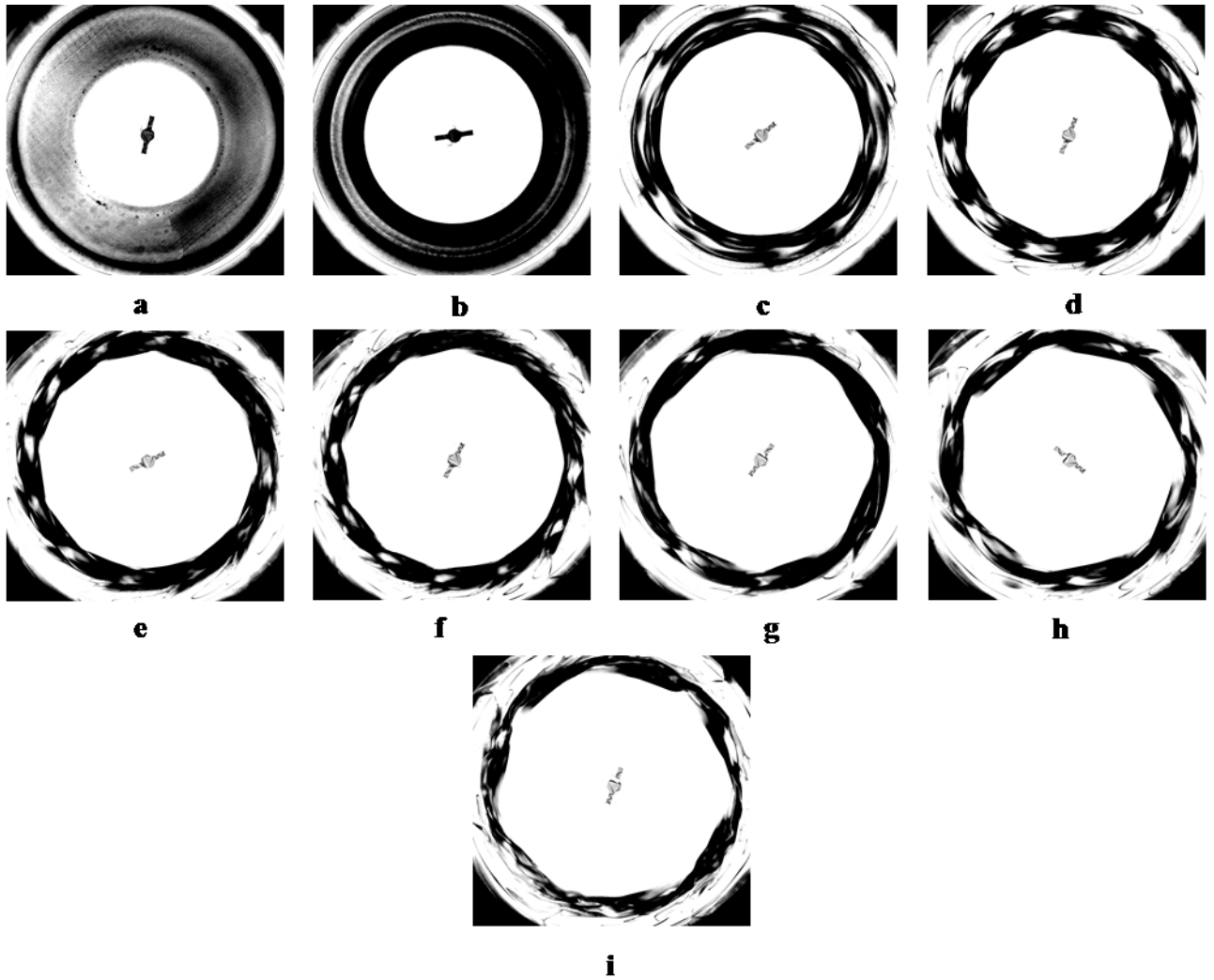


Figure 46. H-22 Oil (12mm) Ascending Sequence Actual Equilibria

Table 12. H-22 Oil – 12mm Descending Sequence Equilibria

| Disk Velocity (rpm) | Equilibria State (N) | Bifurcation | Figure (46) |
|------------------------|-----------------------------|-------------|----------------|
| 235.26 | 7+ | NO | a |
| 225.59 | 7+ | NO | b |
| 213.87 | 6+ | NO | c |
| 185.03 | 12+ | NO | d |
| 145.09 | 5- | NO | e |
| 132.81 | Circle | NO | f |
| 102.6 | Circle | NO | g |

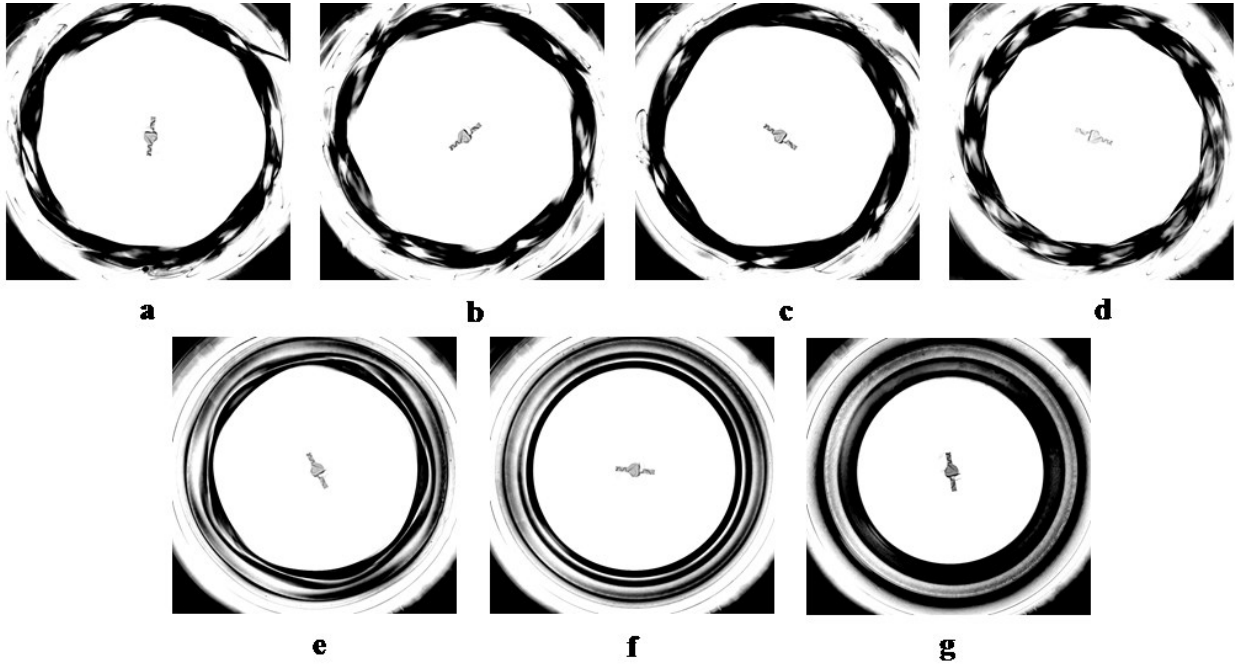


Figure 47. H-22 Oil (12mm) Descending Sequence Actual Equilibria

Appendix B

Table 13. H-32 Oil – 8mm Ascending Sequence Equilibria

| Disk Velocity (rpm) | Equilibria State (<i>N</i>) | Bifurcation | Figure (47) |
|------------------------|----------------------------------|-------------|----------------|
| 61.79 | Circle | NO | a |
| 83.6 | Circle | NO | b |
| 169.77 | Circle | NO | c |
| 202.09 | 9+ | YES | d |
| 202.09 | 7+ | YES | e |
| 202.09 | 8+ | YES | f |
| 236.95 | 8+ | YES | g |
| 236.95 | 9+ | YES | h |
| 263.49 | 9+ | NO | i |
| 316.7 | 5+ | NO | j |

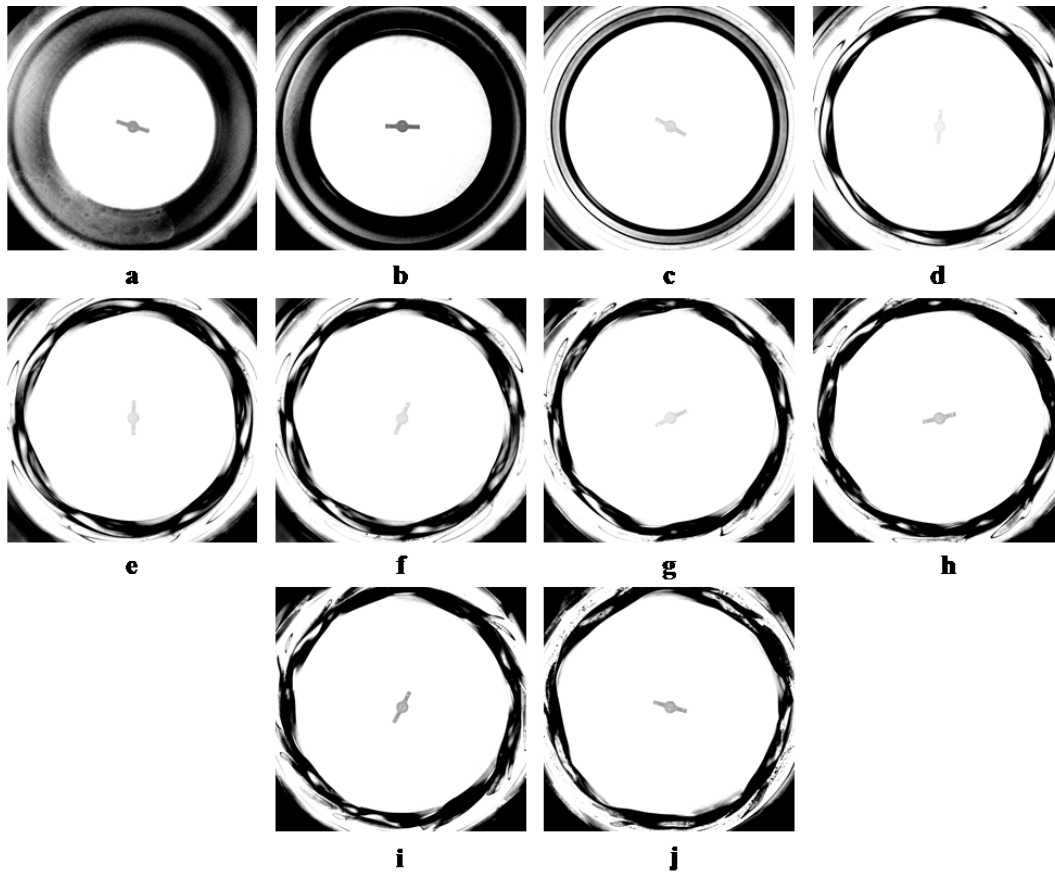


Figure 48. H-32 Oil (8mm) Ascending Sequence Actual Equilibria

Table 14. H-32 Oil – 8mm Descending Sequence Equilibria

| Disk Velocity (rpm) | Equilibria State (<i>N</i>) | Bifurcation | Figure (48) |
|------------------------|----------------------------------|-------------|----------------|
| 261.4 | 9+ | NO | a |
| 224.06 | 8+ | NO | b |
| 194.89 | 7+ | NO | c |
| 168.3 | Circle | NO | d |
| 133.89 | Circle | NO | e |
| 83.17 | Circle | NO | f |

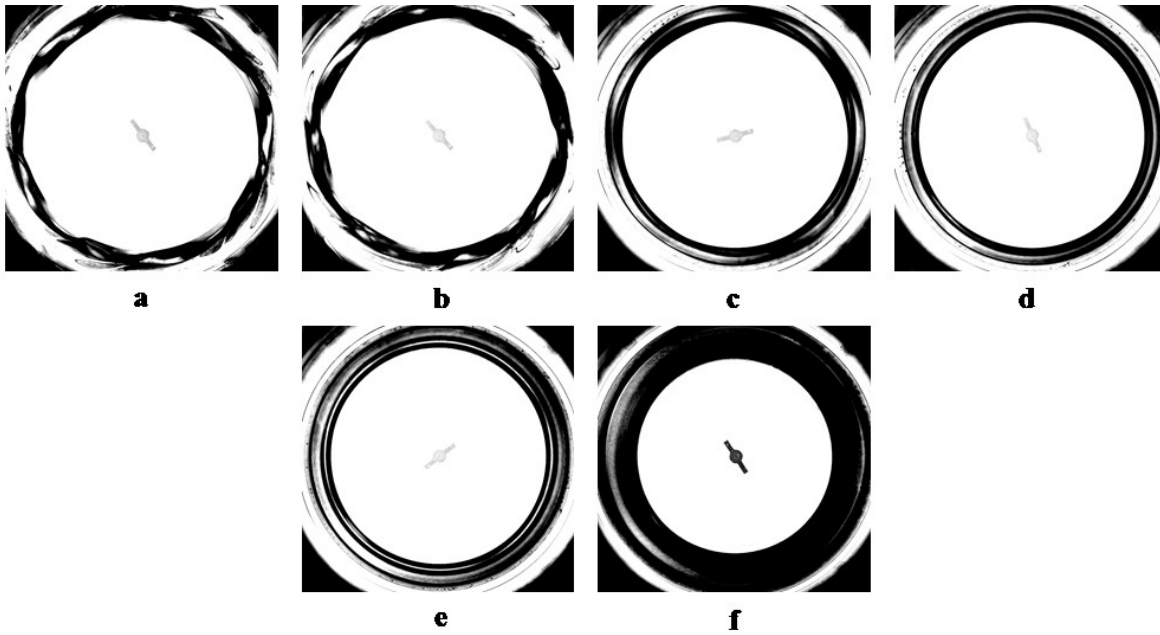


Figure 49. H-32 Oil (8mm) Descending Sequence Actual Equilibria

Table 15. H-32 Oil – 10mm Ascending Sequence Equilibria

| Disk Velocity (rpm) | Equilibria State (N) | Bifurcation | Figure (49) |
|---------------------|--------------------------|-------------|-------------|
| 60 | Circle | NO | a |
| 112.03 | Circle | NO | b |
| 140.75 | Circle | NO | c |
| 191.49 | 7+ | NO | d |
| 218.12 | 7+ | NO | e |
| 238.67 | 8+ | NO | f |
| 255.32 | 8+ | NO | g |
| 269.97 | Mixed of 7+ and 9+ | YES | h |
| 269.97 | 5+ | YES | i |
| 316.07 | 5+ | NO | j |

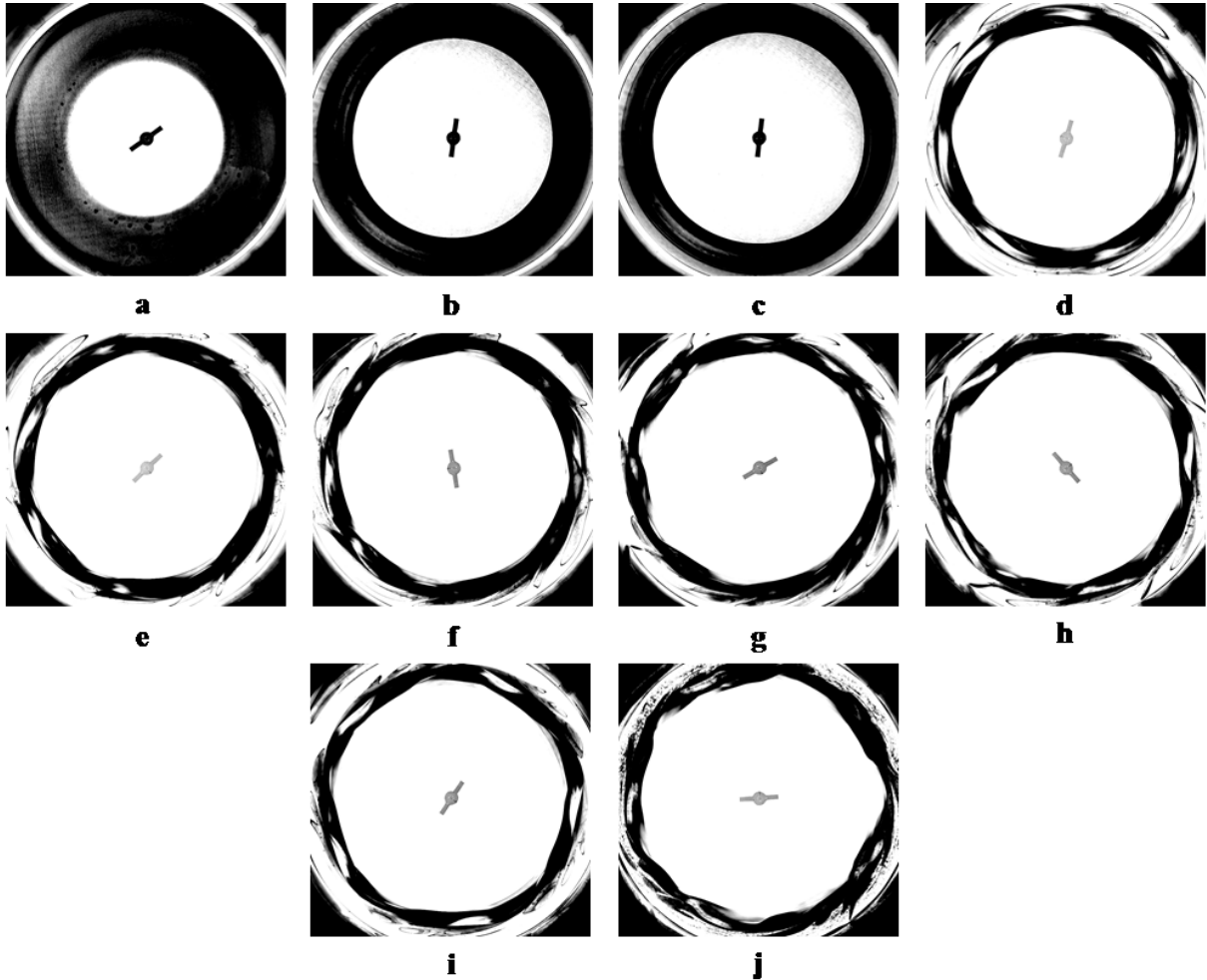


Figure 50. H-32 Oil (10mm) Ascending Sequence Actual Equilibria

Table 16. H-32 Oil – 10mm Descending Sequence Equilibria

| Disk Velocity (rpm) | Equilibria State (<i>N</i>) | Bifurcation | Figure (50) |
|------------------------|----------------------------------|-------------|----------------|
| 286.4 | 5+ | NO | a |
| 249.52 | 8+ | NO | b |
| 209.78 | 7+ | NO | c |
| 187.14 | 6+ | YES | d |
| 187.14 | 7+ | YES | e |
| 168.9 | Circle | NO | f |
| 139.56 | Circle | NO | g |
| 80.72 | Circle | NO | h |

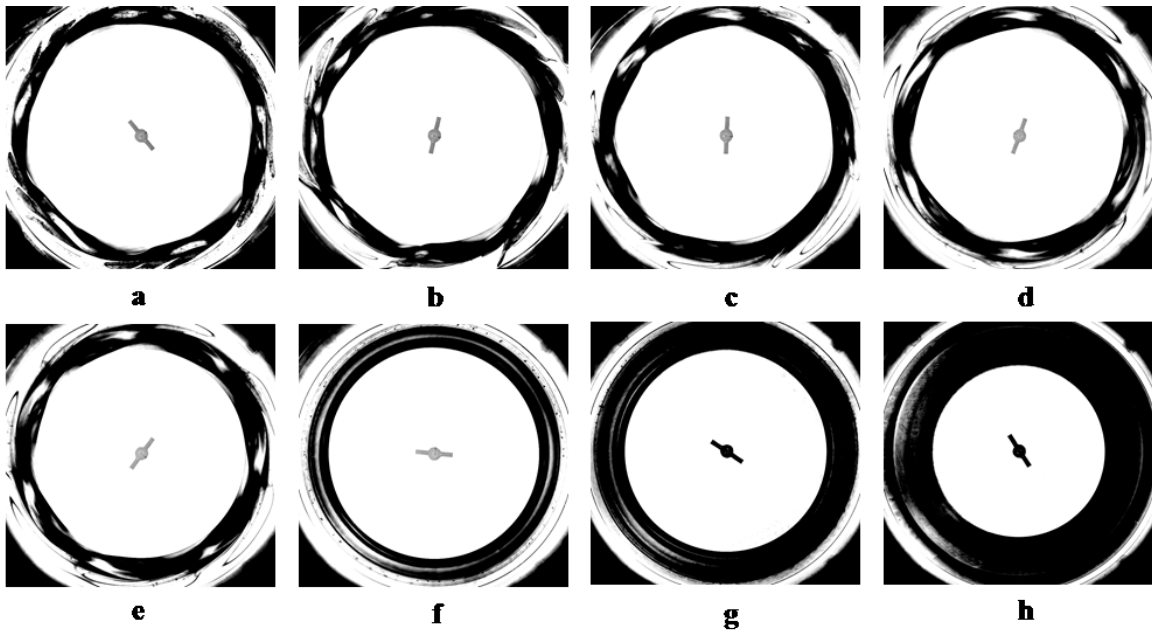


Figure 51. H-32 Oil (10mm) Descending Sequence Actual Equilibria

Table 17. H-32 Oil – 12mm Ascending Sequence Equilibria

| Disk Velocity (rpm) | Equilibria State (<i>N</i>) | Bifurcation | Figure (51) |
|---------------------|-------------------------------|-------------|-------------|
| 64.33 | Circle | NO | a |
| 115.16 | Circle | NO | b |
| 172.44 | Circle | NO | c |
| 190.38 | 6+ | NO | d |
| 212.49 | 6+ | NO | e |
| 245.79 | 7+ | NO | f |
| 261.4 | Mixed of 7+ and 8+ | NO | g |
| 265.6 | 7+ | NO | h |
| 294.08 | 5+ | NO | i |
| 302.17 | 5+ | NO | j |

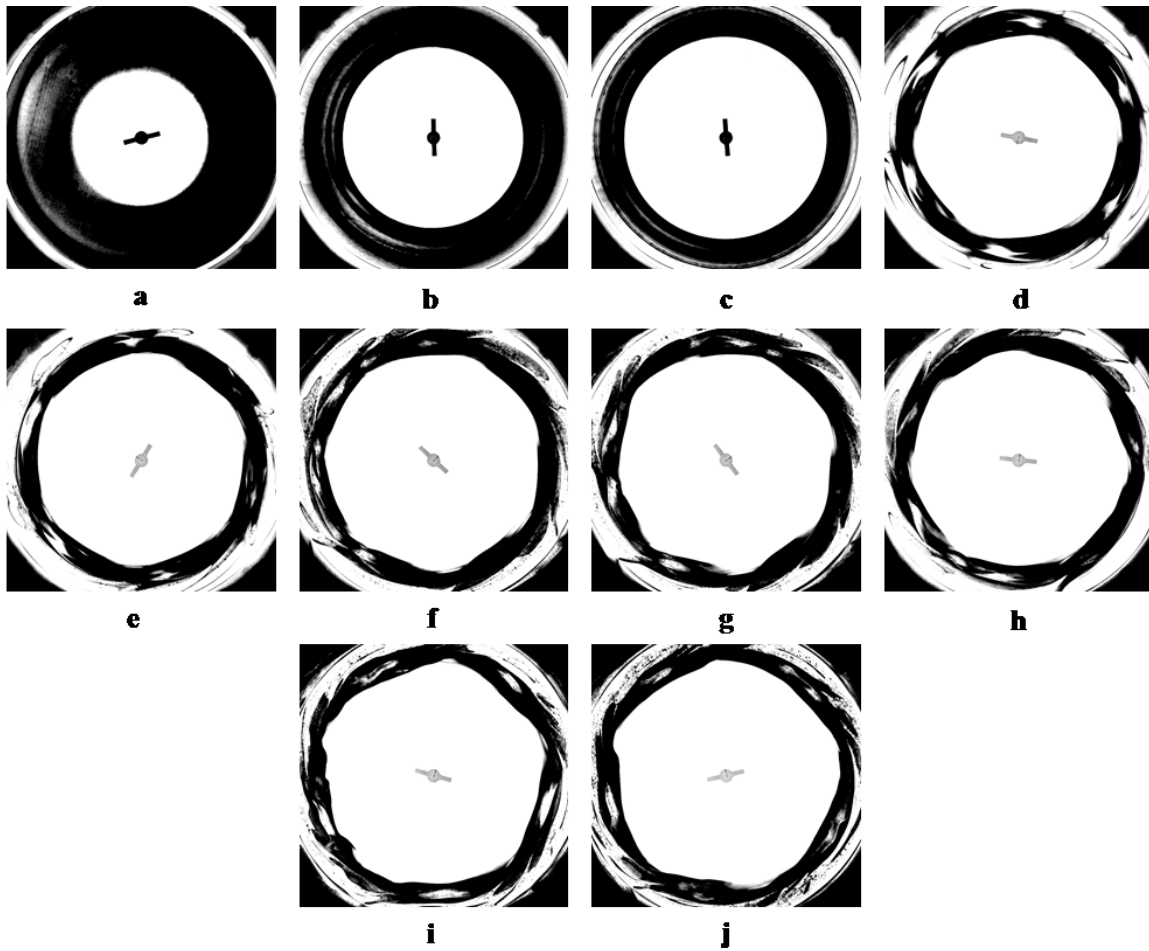


Figure 52. H-32 Oil (12mm) Ascending Sequence Actual Equilibria

Table 18. H-32 Oil – 12mm Descending Sequence Equilibria

| Disk Velocity (rpm) | Equilibria State (N) | Bifurcation | Figure (52) |
|---------------------|--------------------------|-------------|-------------|
| 249.52 | 5+ | YES | a |
| 249.52 | Possible 8+ | YES | b |
| 225.59 | 5+ | NO | c |
| 205.85 | Mixed of 7+ and 8+ | NO | d |
| 197.22 | 12+ | YES | e |
| 197.22 | 6+ | YES | f |
| 168.04 | 6+ | NO | g |
| 163.05 | Circle | NO | h |
| 116.38 | Circle | NO | i |
| 74.18 | Circle | NO | j |

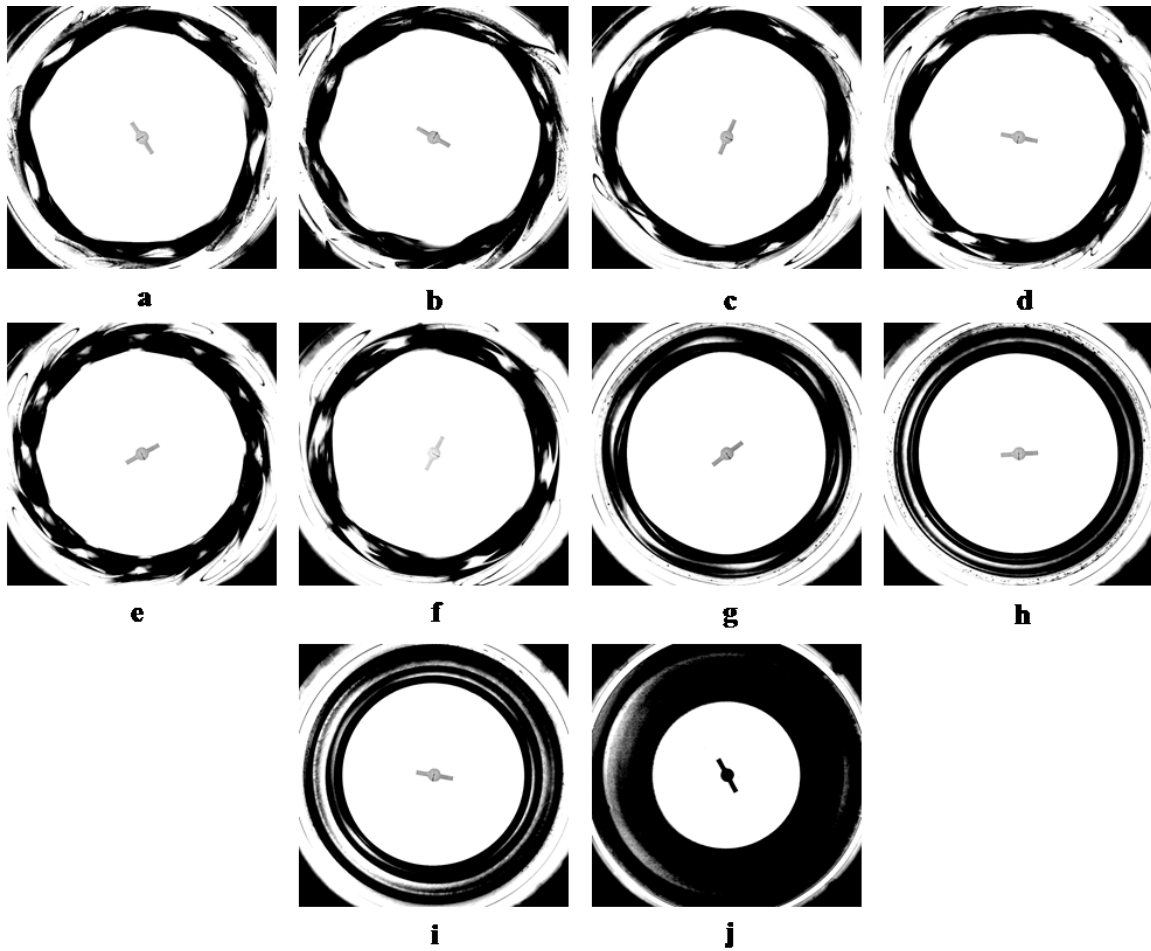
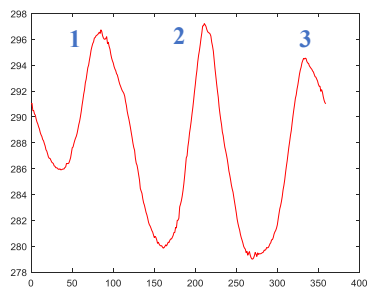
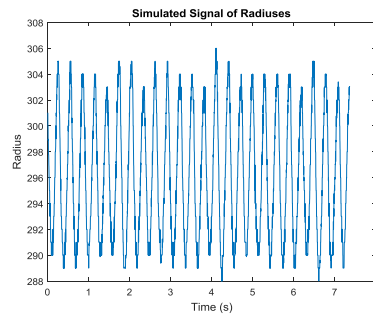


Figure 53. H-32 Oil (12mm) Descending Sequence Actual Equilibria

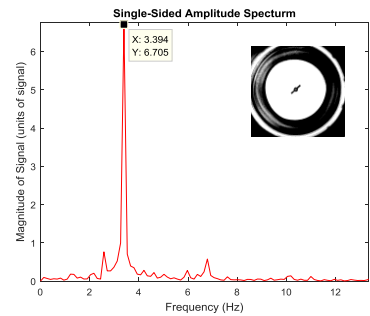
Appendix C



State Number - 3

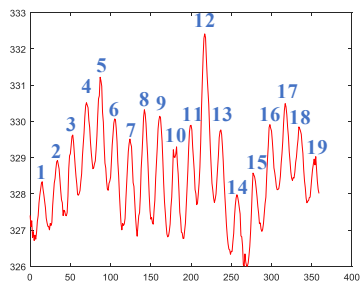


Corresponding Signal

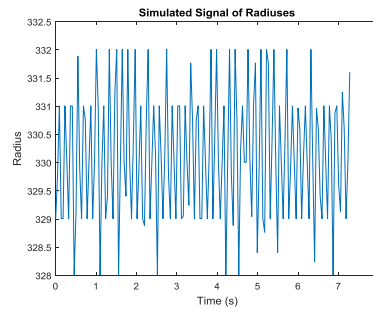


Power Spectrum

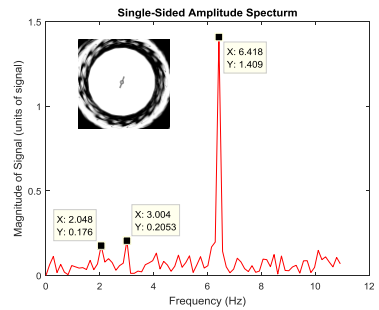
Figure 54. $N=3$ Analysis – Spindle Oil



State Number - 19

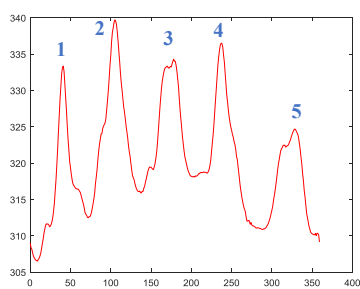


Corresponding Signal

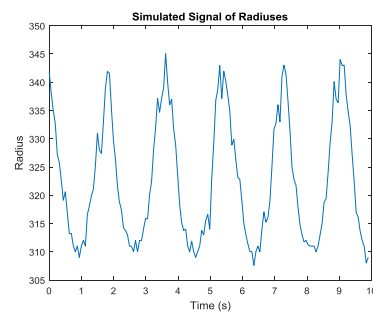


Power Spectrum

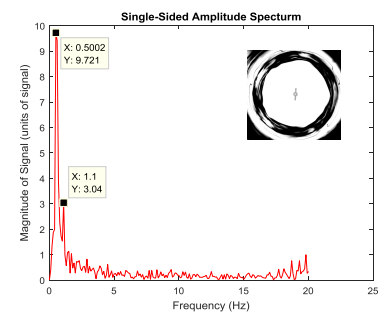
Figure 55. $N=19$ Analysis – Spindle Oil



State Number – 5 Retro-grade

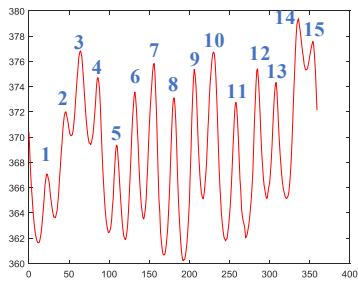


Corresponding Signal

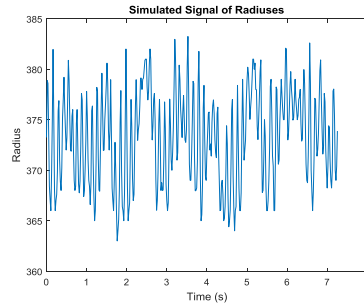


Power Spectrum

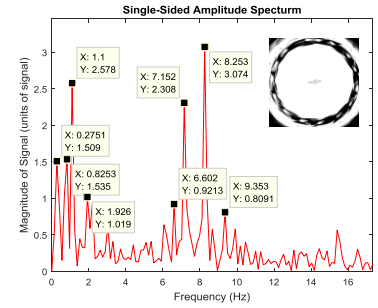
Figure 56. $N=5$ Analysis – Spindle Oil



State Number – 15

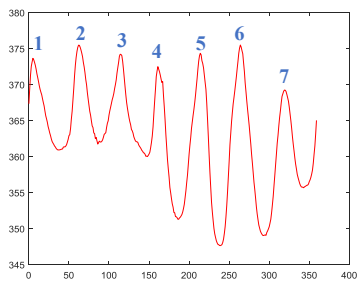


Corresponding Signal

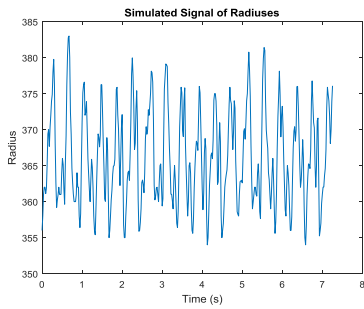


Power Spectrum

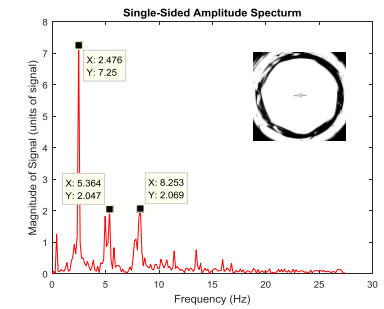
Figure 57. $N=15$ Analysis – H-22 Oil



State Number – 7

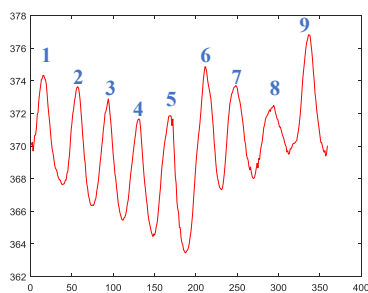


Corresponding Signal

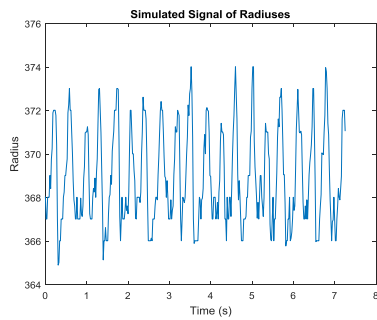


Power Spectrum

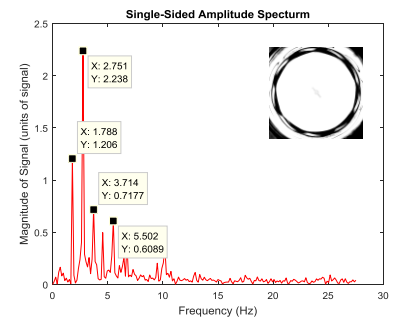
Figure 58. $N=7$ Analysis – H-22 Oil



State Number – 9

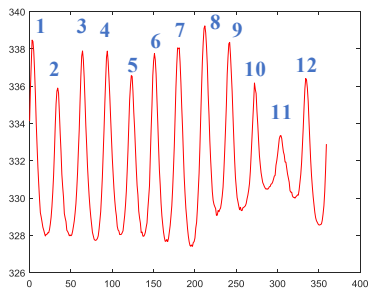


Corresponding Signal

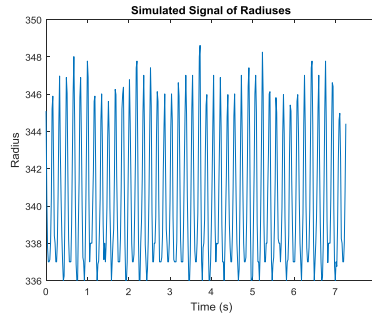


Power Spectrum

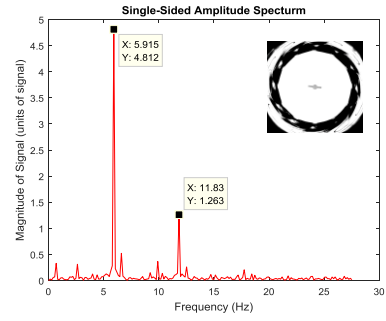
Figure 59. $N=9$ Analysis – H-32 Oil



State Number – 12



Corresponding Signal



Power Spectrum

Figure 60. $N=12$ Analysis – H-32 Oil

Appendix D

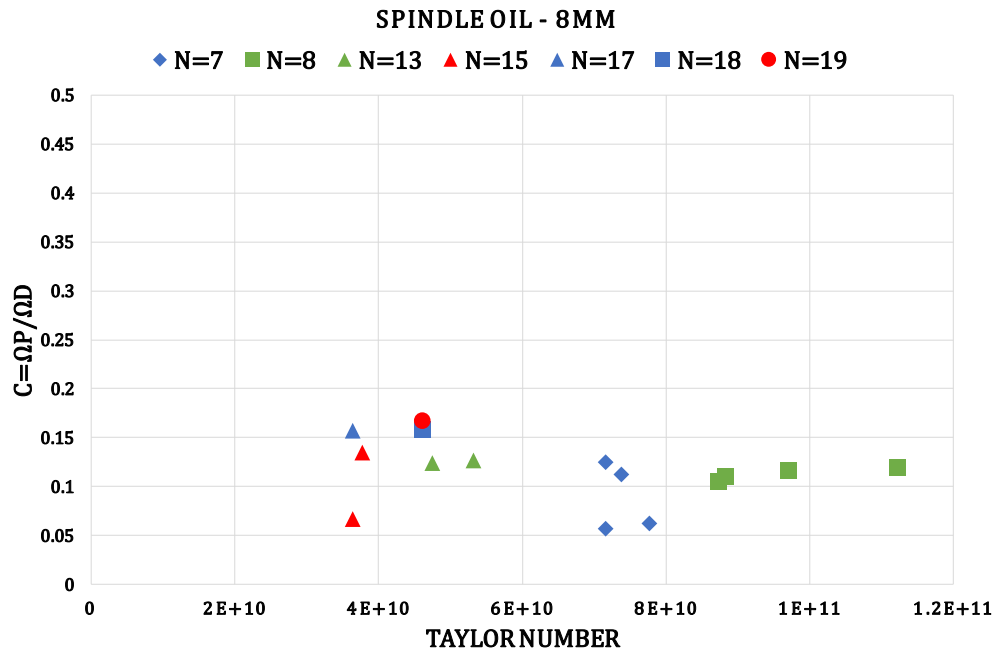


Figure 61. *C* Ratio versus *Taylor Number* - Spindle Oil (8mm)

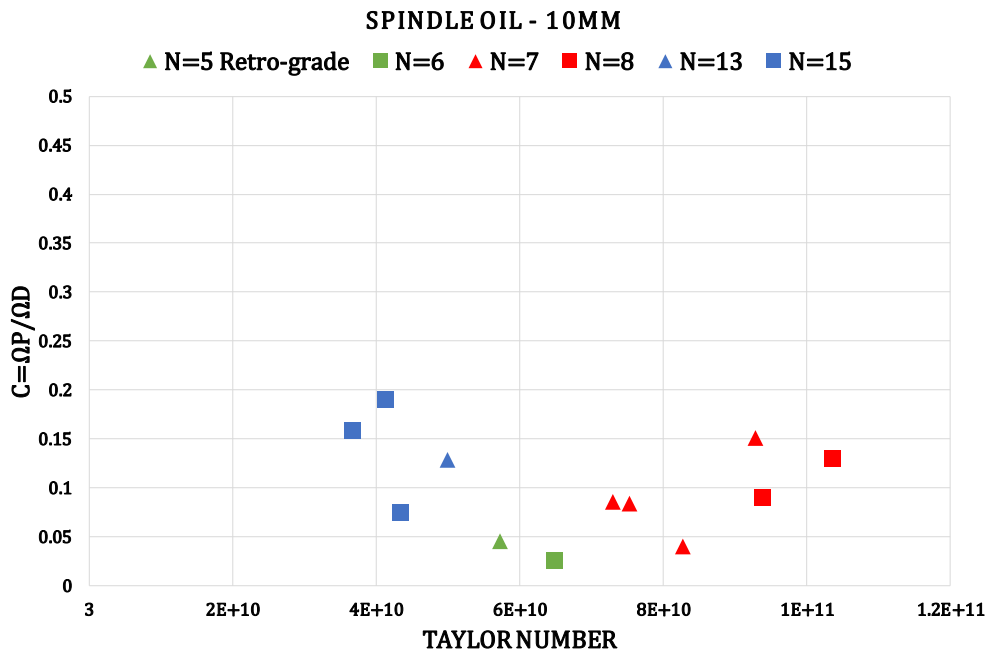


Figure 62. *C* Ratio versus *Taylor Number* - Spindle Oil (10mm)

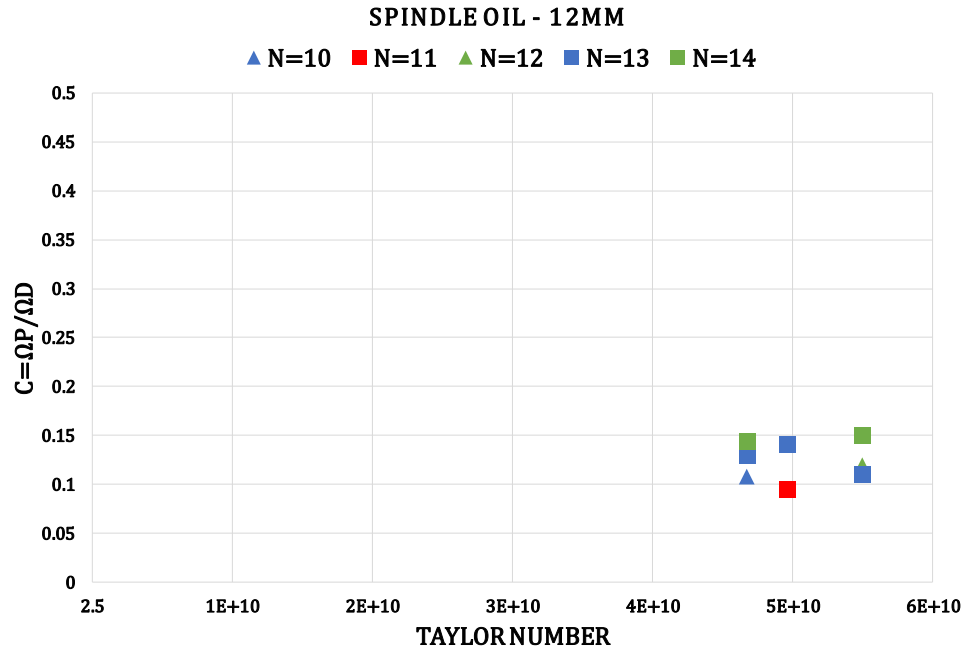


Figure 63. *C* Ratio versus *Taylor Number* - Spindle Oil (12mm)

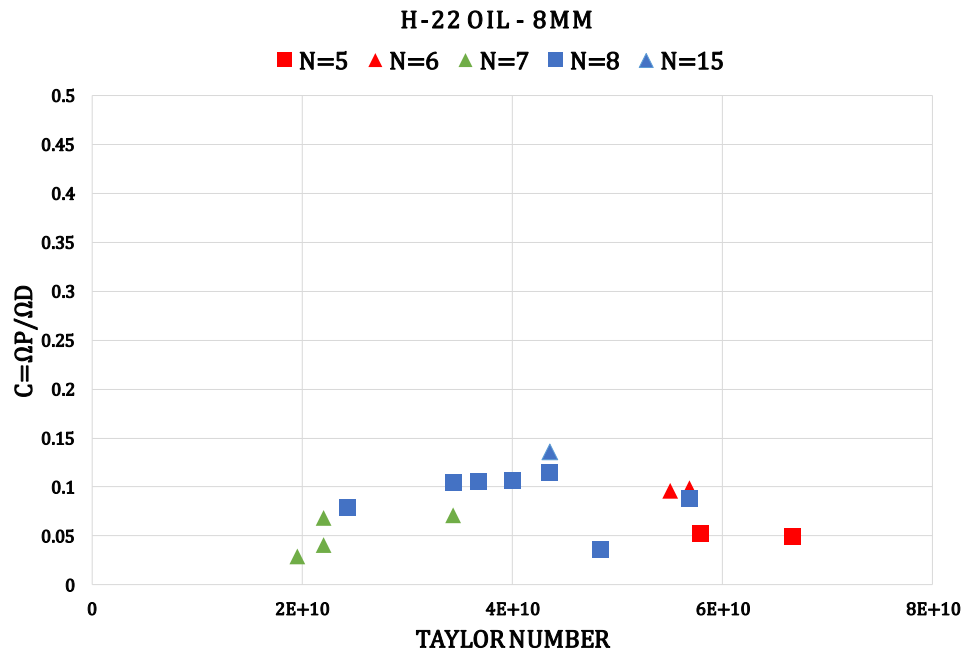


Figure 64. *C* Ratio versus *Taylor Number* – H-22 Oil (8mm)

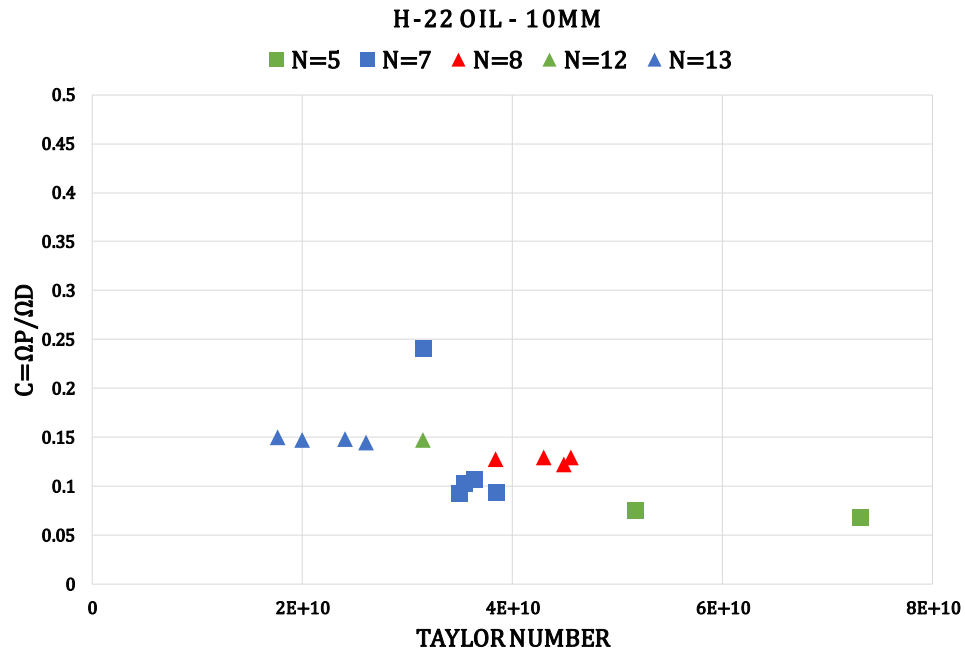


Figure 65. *C* Ratio versus *Taylor Number* – H-22 Oil (10mm)

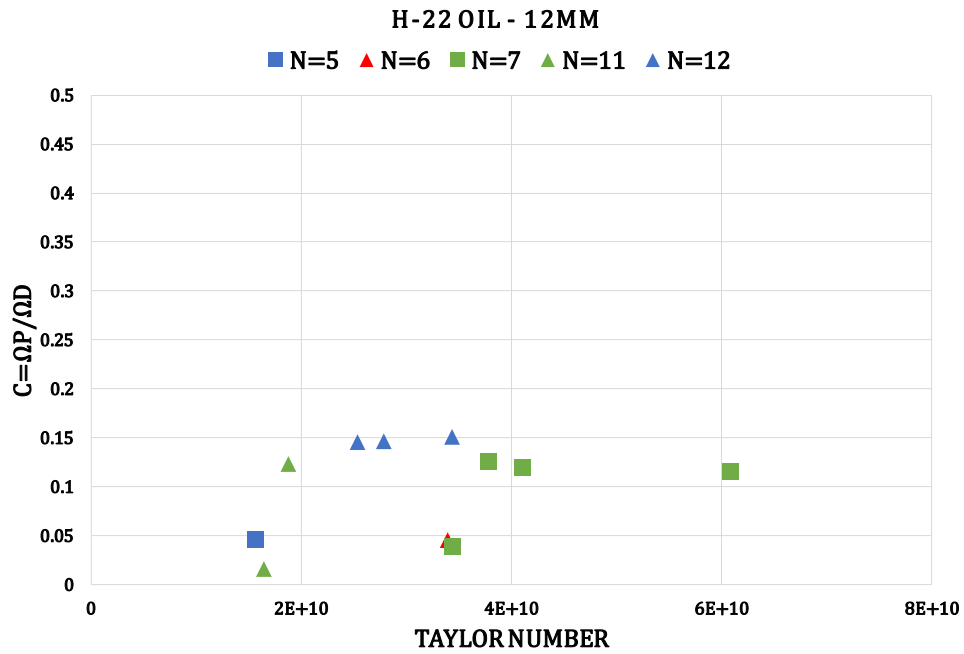


Figure 66. *C* Ratio versus *Taylor Number* – H-22 Oil (12mm)

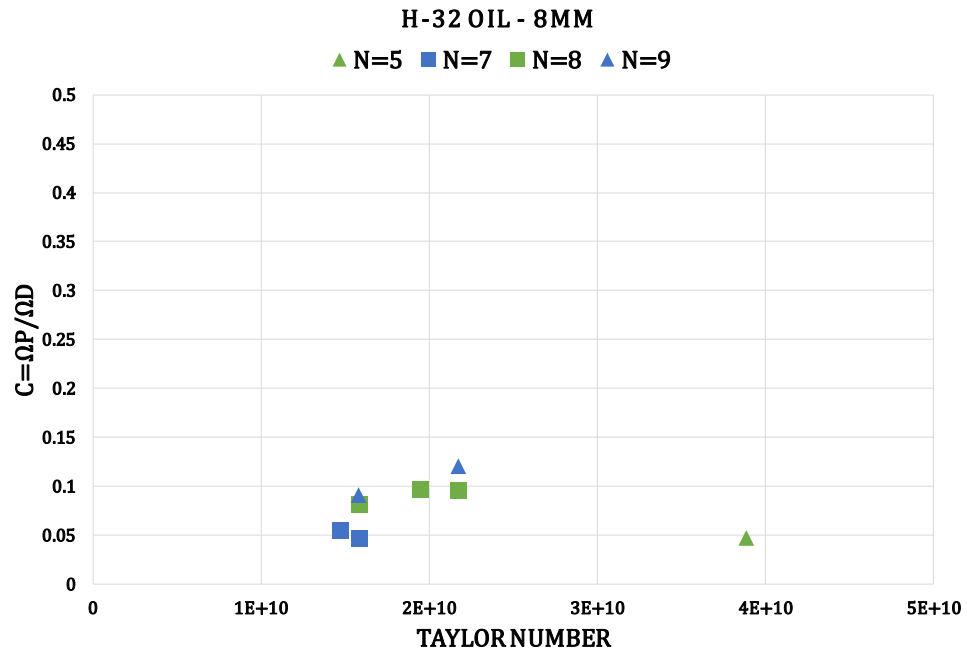


Figure 67. *C* Ratio versus *Taylor Number* – H-32 Oil (8mm)

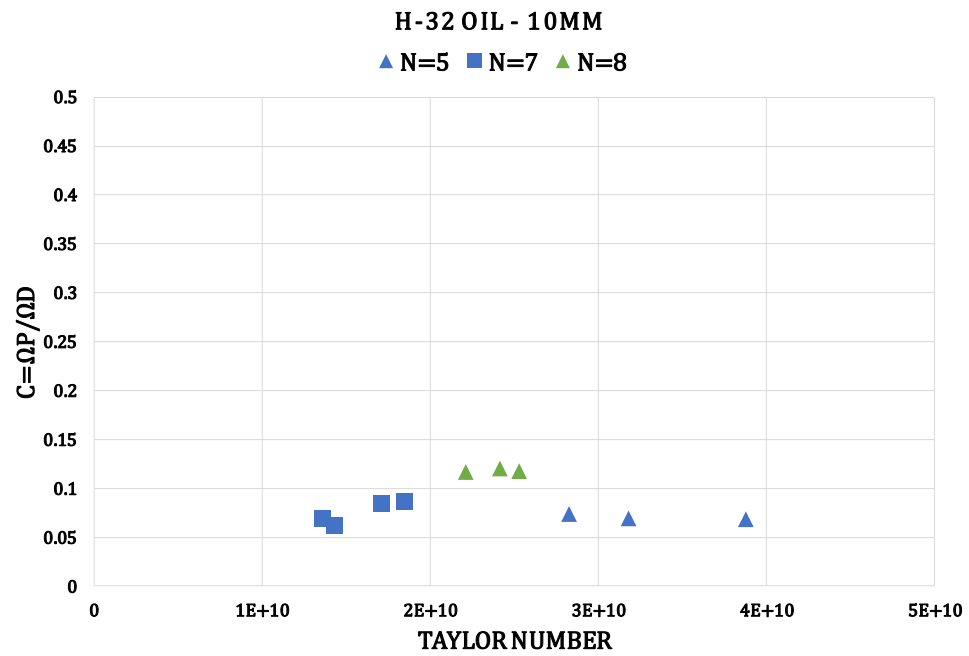


Figure 68. *C* Ratio versus *Taylor Number* – H-32 Oil (10mm)

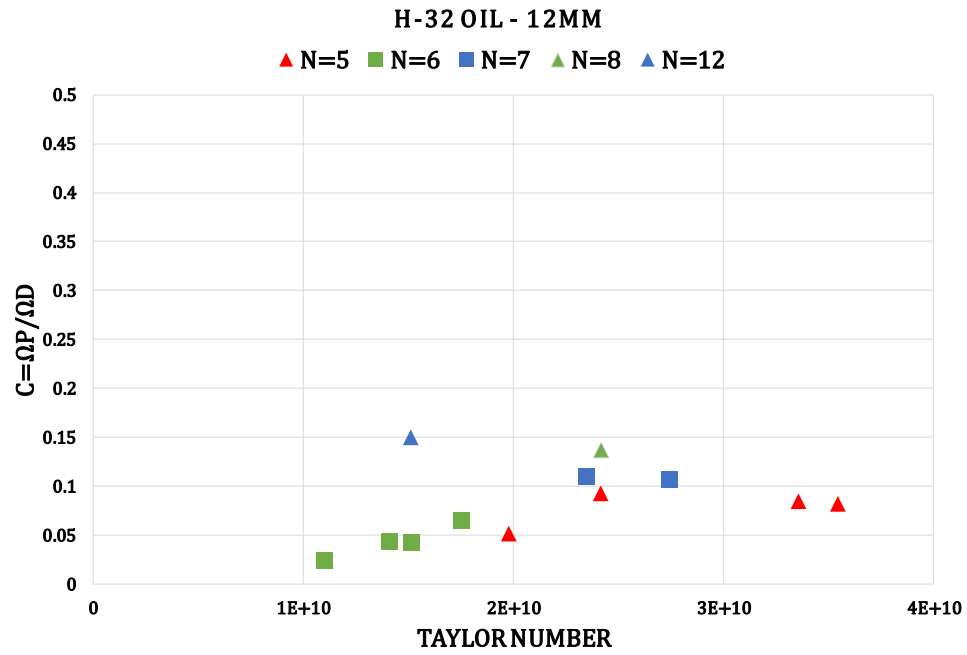


Figure 69. *C* Ratio versus *Taylor Number* – H-32 Oil (12mm)

Appendix E

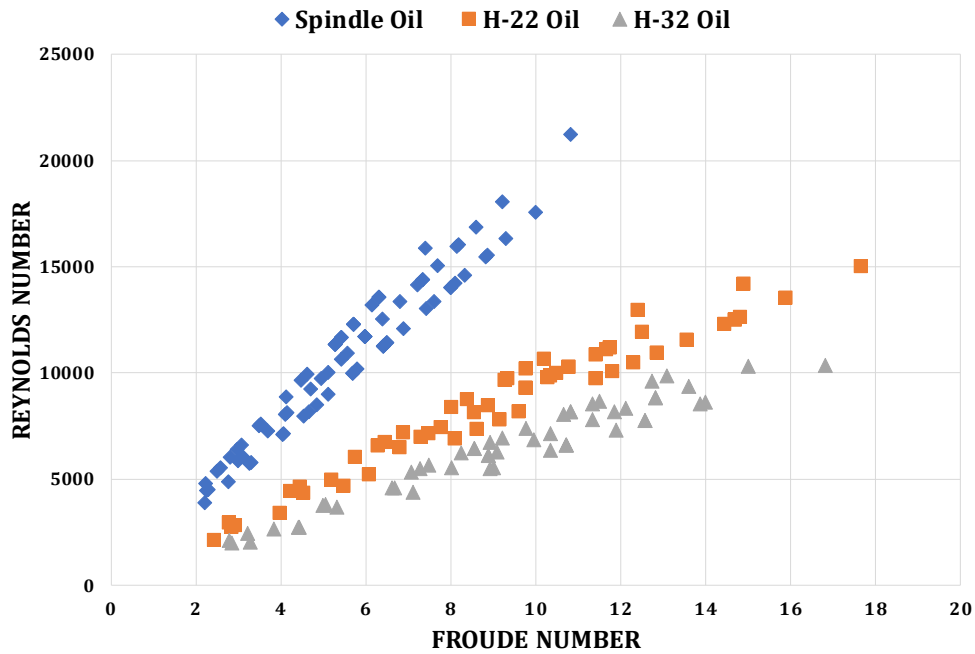


Figure 70. Superposition of Reynolds Number vs Froude Number

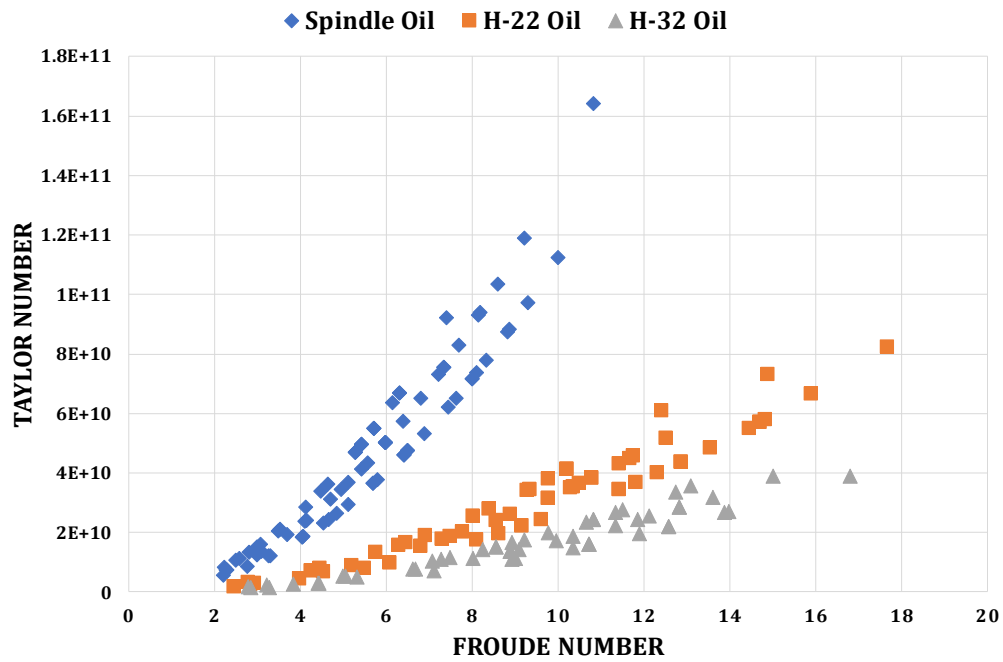


Figure 71. Superposition of Taylor Number vs Froude Number

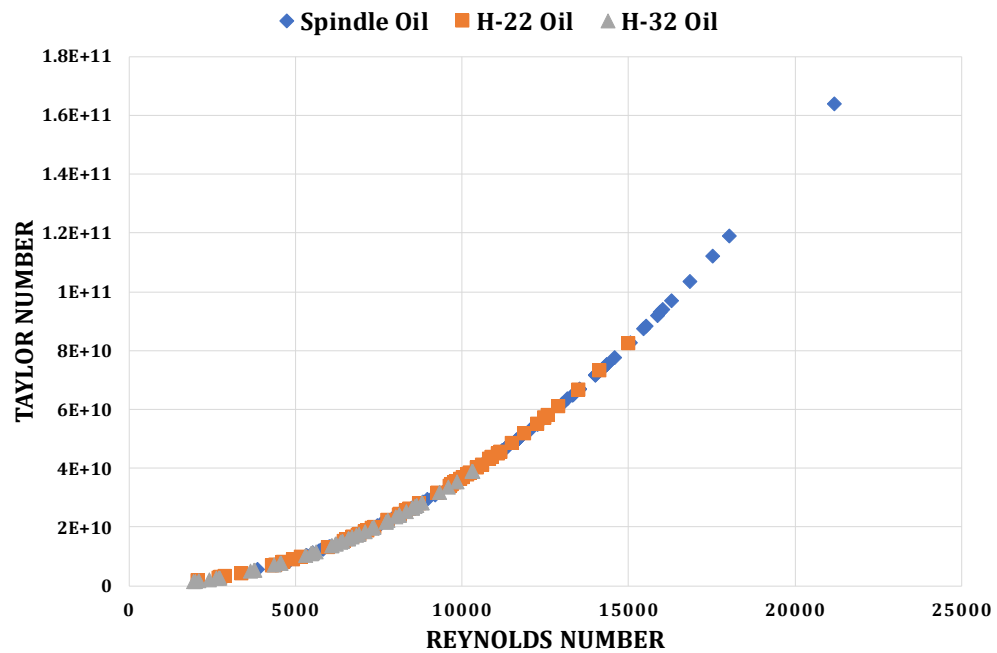


Figure 72. Superposition of Taylor Number vs Reynolds Number

Appendix F

```

close all
clear all
clc;
for j=1:4000 % j can be starting 1:3500 since we have 3500 images each time
    %K=K+1;
    i=0000+(j);
    fname=int2str(i);
    if i<10
        fname1='8_000'; %file path:
    end
    if i>=10
        fname1='8_00'; %file path:
    end
    if i>=100
        fname1='8_0'; %file path:
    end
    if i>=1000
        fname1='8_'; %file path:
    end
    fname=strcat(fname1,fname);
    fname=strcat(fname, '.bmp');
    im=imread(fname);
    im=im(15:870,20:900); %Defining the appropriate size fram
    h=fspecial('gaussian',100,15); %filtering the image
    bim=imfilter(im,h,'replicate'); %filtering the image
    bim=im2bw(bim,225/250);
    B0=boundaries(bim); d=cellfun('length',B0); [max_d,k]=max(d); b0=B0{k}; [M,N]=size(bim); ???
    a1=ones(1,5)/5; % 10 point averaging filter, Noncausal
    b0=filtfilt(a1,1,b0);

    [st0(:,j),angle0(:,j),x0(j),y0(j)]=signature(b0);

    for i=1:max(size(b0))
        b0(i,1)=b0(i,1)-x0(j);
        b0(i,2)=b0(i,2)-y0(j);
    end
    [st1(:,j),angle1(:,j),x1(j),y1(j)]=signature(b0); %st=radius
    %%%%%%IMPORTANT=
end
x=st1(1,:);
%samp=fft(x);
Fs=548.95; %Camera frequency
T_inc=1/Fs; % Time increment
m=numel(x);
m=T_inc*m;
T_measure=m-T_inc; %time of measurment
L=T_measure/T_inc;%Lenght of signal vector
time=0:T_inc:T_measure; % Time vector

[frequency,amplitude]=funct_fft(time,x);
figure;

```

```

plot(time(:),x(:));
xlabel('Time (s)');
ylabel('Radius');
title('Simulated Signal of Radiuses');

```

```

function [st, angle, x0, y0] = signature(b, varargin)
%SIGNATURE Computes the signature of a boundary.
% [ST, ANGLE, X0, Y0] = SIGNATURE(B) computes the signature of a
% given boundary, B, where B is an np-by-2 array (np > 2)
% containing the (x, y) coordinates of the boundary ordered in a
% clockwise or counterclockwise direction. The amplitude of the
% signature as a function of increasing ANGLE is output in
% ST. (X0,Y0) are the coordinates of the centroid of the
% boundary. The maximum size of arrays ST and ANGLE is 360-by-1,
% indicating a maximum resolution of one degree. The input must be
% a one-pixel-thick boundary obtained, for example, by using the
% function boundaries. By definition, a boundary is a closed
% curve.
%
% [ST, ANGLE, X0, Y0] = SIGNATURE(B) computes the signature, using
% the centroid as the origin of the signature vector.
%
% [ST, ANGLE, X0, Y0] = SIGNATURE(B, X0, Y0) computes the boundary
% using the specified (X0, Y0) as the origin of the signature
% vector.

% Copyright 2002-2004 R. C. Gonzalez, R. E. Woods, & S. L. Eddins
% Digital Image Processing Using MATLAB, Prentice-Hall, 2004
% $Revision: 1.6 $ $Date: 2003/11/21 14:46:47 $

% Check dimensions of b.
[np, nc] = size(b);
if (np < nc | nc ~= 2)
    error('B must be of size np-by-2.');
```

```

end

% Some boundary tracing programs, such as boundaries.m, end where
% they started, resulting in a sequence in which the coordinates
% of the first and last points are the same. If this is the case,
% in b, eliminate the last point.
if isequal(b(1, :), b(np, :))
    b = b(1:np - 1, :);
    np = np - 1;
end

% Compute parameters.
if nargin == 1
    x0 = round(sum(b(:, 1))/np); % Coordinates of the centroid.
    y0 = round(sum(b(:, 2))/np);
elseif nargin == 3
    x0 = varargin{1};
    y0 = varargin{2};
else
    error('Incorrect number of inputs.');
```

```

end

% Shift origin of coord system to (x0, y0)).
b(:, 1) = b(:, 1) - x0;
b(:, 2) = b(:, 2) - y0;

% Convert the coordinates to polar. But first have to convert the
% given image coordinates, (x, y), to the coordinate system used by
% MATLAB for conversion between Cartesian and polar coordinates.
% Designate these coordinates by (xc, yc). The two coordinate systems
% are related as follows: xc = y and yc = -x.
xc = b(:, 2);
yc = -b(:, 1);
[theta, rho] = cart2pol(xc, yc);

% Convert angles to degrees.
theta = theta.*(180/pi);

% Convert to all nonnegative angles.
j = theta == 0; % Store the indices of theta = 0 for use below.
theta = theta.*(0.5*abs(1 + sign(theta)))...
    - 0.5*(-1 + sign(theta)).*(360 + theta);
theta(j) = 0; % To preserve the 0 values.

temp = theta;
% Order temp so that sequence starts with the smallest angle.
% This will be used below in a check for monotonicity.
I = find(temp == min(temp));

% Scroll up so that sequence starts with the smallest angle.
% Use I(1) in case the min is not unique (in this case the
% sequence will not be monotonic anyway).
temp = circshift(temp, [-(I(1) - 1), 0]);

% Check for monotonicity, and issue a warning if sequence
% is not monotonic. First determine if sequence is
% cw or ccw.
k1 = abs(temp(1) - temp(2));
k2 = abs(temp(1) - temp(3));
if k2 > k1
    sense = 1; % ccw
elseif k2 < k1
    sense = -1; % cw
else
    warning(['The first 3 points in B do not form a monotonic ' ...
        'sequence.']);
end

% Check the rest of the sequence for monotonicity. Because
% the angles are rounded to the nearest integer later in the
% program, only differences greater than 0.5 degrees are
% considered in the test for monotonicity in the rest of
% the sequence.
flag = 0;
for k = 3:length(temp) - 1
    diff = sense*(temp(k + 1) - temp(k));

```

```

        if diff < -.5
            flag = 1;
        end
    end
end
if flag
    warning('Angles do not form a monotonic sequence.');
```

```

end

% Round theta to 1 degree increments.
theta = round(theta);

% Keep theta and rho together.
tr = [theta, rho];

% Delete duplicate angles. The unique operation
% also sorts the input in ascending order.
[w, u, v] = unique(tr(:, 1));
tr = tr(u,:); % u identifies the rows kept by unique.

% If the last angle equals 360 degrees plus the first
% angle, delete the last angle.
if tr(end, 1) == tr(1) + 360
    tr = tr(1:end - 1, :);
end

% Output the angle values.
angle = tr(:, 1);

% The signature is the set of values of rho corresponding
% to the angle values.
st = tr(:, 2);
```